Integration of Planar Antennas with MMIC Active Frontends for THz Imaging Applications

Yogesh Karandikar

Integration of Planar Antennas with MMIC Active Frontends for THz Imaging Applications

YOGESH KARANDIKAR

Microwave Electronics Laboratory
Department of Microtechnology and Nanoscience (MC2)
Chalmers University of Technology
SE–412 96 Göteborg, Sweden
Phone: +46 (0)31–772 1000

Abstract

In recent years, there has been constant growth in using THz frequencies or mm, sub-mm wavelengths for various applications such as: Astronomy, Atmospheric studies, security, bio-medical imaging. All these applications are now seen more feasible due to rapid enhancements of semi-conductor processing technologies. The state of the art MMIC processing techniques offering increased cut-off frequencies ($>$ 500 GHz) of HEMT/HBT transistors, open up new opportunities for integrating systems on chip along with an antenna for either Transmit/Receive architecture.

The work carried out in this thesis mainly deals with the development of antenna structures which are compatible to available MMIC processes and have well defined interface with the active circuit components for microwave as well as mm/sub-mm wave applications. The thesis briefly reviews the THz applications and modern MMIC process techniques. Thereafter the emphasis is on various possible antenna structures which are feasible to fabricate with MMIC layer topologies. Such antenna structures are further compared in terms of their Gain, Bandwidth, Directivity, Gaussian Coupling Efficiency and Compactness.

The main focus of the thesis is towards the development of multi-pixel front ends for THz imaging of concealed weapons for security applications. The requirement in this type of application is the heterodyne detection of reflected THz signals from the distant objects ($>$ 20 m) with tightly integrated pixels constituting of antenna integrated receiver (Antenna + Mixer + LO-Multiplier chain) giving real-time video imaging. Thus the work is focused towards Co-design of Antenna + Mixer aiming towards compactness and minimizing physical area of pixel for tighter integration.

One of the important results obtained in this work, is the integration of a Double Slot Antenna with a sub-harmonically pumped resistive mixer. The novelty in this work is the new geometrical placements of slots and microstrip feed network. This new topology has differential excitation of two parallel slots for broadside beam. With this new arrangement, the need of conventional power combining network from two slots is eliminated and the transistors can directly be placed between the two slots, thus minimizing the physical area. Such arrangement is fabricated and tested at frequency of 200 GHz using 50 nm HEMT process. Encouraging results are obtained with mixer conversion loss of $\simeq$ 15 dB with +3 dBm LO power at sub-harmonic of 100 GHz.

The next key result of this thesis is the integration of a differential 2 x 2 array of microstrip patch antennas with Gilbert Cell type sub-harmonically pumped mixer. This integration is achieved using 250 nm DHBT process. Considering the antenna ohmic efficiency, mixer conversion loss and gain of IF amplifier; the overall receiver front end features a conversion gain of $\simeq$ 14 $\pm$ 1 dB at frequency of 320 GHz when pumped with sub-harmonic LO of 160 GHz with $\simeq$ 4 dBm on chip power. This receiver was also tested close to 340 GHz, which is a target frequency for security imaging applications.

Another important aspect of this work is to quantify the ability of a planar antenna to couple radiated power in to the THz quasi-optical system. This is often evaluated as Gaussian Coupling Efficiency or Gaussicity. Therefore MMIC integrated antennas are needed to be characterized in terms of their Gaussicity as well. For this, a new algorithm has been developed which accepts the far-field of the antenna as input and computes the optimum beam parameters (waist and its position) which maximize the Gaussicity. Furthermore this algorithm is applied to different antenna array configurations to quantify their radiation pattern for Gaussian Coupling Efficiency.

Furthermore, a modified method to measure noise figure of resistive mixer has been developed. This new method can measure noise figure exceeding 10 dBs where conventional Y-factor method is limited due to measurement uncertainty for very small Y-factors ($<$ 0.1 dB).

Keywords: THz, MMIC, Gaussian Coupling, Planar Antennas, Lens Antenna, Sub-Harmonic Resistive Mixer, Gilbert Cell Mixer.

Appended Publications

[A]   Y. Yan, Y. B. Karandikar, S. E. Gunnarsson, M. Urteaga, R. Pierson, and H. Zirath, "340 ghz integrated receiver in 250nm dhbt technology," *THz Science and Technology, accepted to IEEE Transactions on*, vol. xx, no. xx, p. xx, 2012.

[B]   Y. B. Karandikar, H. Zirath, Y. Yan, V. Vassilev, J. Bergman, and D.-H. Kim, "Compact integration of sub-harmonic resistive mixer with differential double slot antenna in g-band using 50nm inp-hemt mmic process," *Microwave Theory and Techniques, submitted to IEEE Transactions on*, vol. xx, no. xx, p. xx, 2012.

[C]   Y. Karandikar, "Factorization of gaussian coupling efficiency and algorithm to compute it," in *Antennas and Propagation, 2012. EuCAP 2012. The Sixth European Conference on*, March 2012, pp. 1 –5.

[D]   Y. Yan, Y. B. Karandikar, S. E. Gunnarsson, B. M. Motlagh, S. Cherednichenko, I. Kallfass, A. Leuther, and H. Zirath, "Monolithically integrated 200-ghz double-slot antenna and resistive mixers in a gaas-mhemt mmic process," *Microwave Theory and Techniques, IEEE Transactions on*, vol. 59, no. 10, pp. 2494–2503, 2011.

[E]   Y. Yan, Y. B. Karandikar, S. E. Gunnarsson, and H. Zirath, "24 ghz balanced self-oscillating mixer with integrated patch antenna array," in *European Microwave Week (EuMW), 2011 Proceedings of the Fourth*, October 2011, pp. 404–407.

[F]   J. Yang, M. Pantaleev, P.-S. Kildal, B. Klein, Y. Karandikar, L. Helldner, N. Wadefalk, and C. Beaudoin, "Cryogenic 2-13 ghz eleven feed for reflector antennas in future wideband radio telescopes," *Antennas and Propagation, IEEE Transactions on*, vol. 59, no. 6, pp. 1918 –1934, june 2011.

[G]   Y. Karandikar, "Pattern studies of two parallel dipoles above ground plane in eleven configuration as feed for reflector antenna," *Antennas and Wireless Propagation Letters, IEEE*, vol. 9, pp. 558 –561, 2010.

[H]   Y. Karandikar, D. Nyberg, N. Jamaly, and P.-S. Kildal, "Mode counting in rectangular, cylindrical, and spherical cavities with application to wireless measurements in reverberation chambers," *Electromagnetic Compatibility, IEEE Transactions on*, vol. 51, no. 4, pp. 1044 –1046, nov. 2009.

Other Publications

[a]   Y. B. Karandikar, J. Yang, and P.-S. Kildal, "Reduction of radiation from central exciting region of eleven feed and pattern improvements for vlbi2010 applications," in *Antennas and Propagation (EuCAP), 2010 Proceedings of the Fourth European Conference on*, april 2010, pp. 1 –5.

[b]   Y. B. Karandikar and P.-S. Kildal, "Comparisons of different descrambler/power combining boards layout for multi-port, decade bandwidth eleven feed," in *Antennas and Propagation (EuCAP), 2010 Proceedings of the Fourth European Conference on*, april 2010, pp. 1 –6.

[c]   Y. Karandikar and P.-S. Kildal, "X-ka dual band prime focus feed for satellite earth terminals," in *Antennas and Propagation, 2009. EuCAP 2009. 3rd European Conference on*, march 2009, pp. 3085 –3089.

[d]   Y. Karandikar and P. Kildal, "Optimization of 200-800mhz eleven feed for gmrt," in *Antennas and Propagation, 2007. EuCAP 2007. The Second European Conference on*, nov. 2007, pp. 1 –6.

Patent

[a]   H. Zirath and Y. Karandikar, "Integration of resistive mixer with differential antenna," Patent 61 553 275, October 31, 2011.

Dedicated to Passionate Engineers
who make things work...

Acknowledgments

Contents

List of Tables

List of Figures

Abbreviations

AUT	Antenna Under Test
CPW	Coplanar Waveguide
DSB	Double Side Band
DUT	Device Under Test
FDTD	Finite Difference Time Domain
FEM	Finite Element Method
FET	Field Effect Transistor
FMCW	Frequency Modulated Continuous Wave
GCPW	Grounded Coplanar Waveguide
GO	Geometrical Optics
HB	Harmonic Balance
HBT	Heterojunction Bipolar Transistor
HEMT	High Electron Mobility Transistor
HM	Harmonic Mixer
HPBW	Half Power Beam Width
IF	Intermediate Frequency
LNA	Low Noise Amplifier
LO	Local Oscillator
MIC	Monolithic Integrated Circuit
MMIC	Microwave Monolithic Integrated Circuit
MoM	Method of Moments
NF	Noise Figure
PLL	Phase Locked Loop
PO	Physical Optics
RC	Reverberation Chamber
RF	Radio Frequency
Rx	Receiver
SHM	Sub-Harmonically Pumped Mixer
SSB	Single Side Band
SMMIC	Sub Millimeter Wave Monolithic Integrated Circuit
TE	Transverse Electric
TEM	Transverse Electromagnetic
TM	Transverse Magnetic
TMIC	Tera-Hertz Monolithic Integrated Circuit
Tx	Transmitter
VCO	Voltage Controlled Oscillator
VNA	Vector Network Analyzer
VSWR	Voltage Standing Wave Ratio
x N	Times N Multiplier Chain (N=2,3,4..)

Notations

$G(\theta, \phi)$	Far-field Function of Antenna in Spherical Coordinate System
$G_\theta(\theta, \phi)$	Theta Component of Far-field Function
$G_\phi(\theta, \phi)$	Phi Component of Far-field Function
$\hat{co}$	Co-polar Unit Vector
$\hat{xp}$	Cross-polar Unit Vector
$G_{co45}(\theta)$	Co-polar far-field function in $\phi = 45°$ plane
$G_{xp45}(\theta)$	Cross-polar far-field function in $\phi = 45°$ plane
η_{ap}	Aperture Efficiency
η_G	Gaussian Coupling Efficiency
η_{pol}	Polarization Efficiency
η_{ill}	Illumination Efficiency
η_{spill}	Spill Over Efficiency
η_{BOR_1}	Body of Revolution-Type 1 Efficiency
η_ϕ	Phase Efficiency
$\eta_{BOR_1}^{Gauss}$	Coupling efficiency between Gaussian Beam and BOR_1 components
η_{ohmic}	Ohmic Efficiency
η_{refl}	Reflection Efficiency
Γ_A	Input Reflection Coefficient of Antenna
A_e	Effective Antenna Area (m^2)
$f/_D$	Focal length to diameter ratio
θ_o	Half subtended angle of the prime focus reflector (degrees)
$D(\theta, \phi)$	Directivity of Antenna (dBi)
$D_E(\theta)$	Directivity of Antenna in E-plane (dBi)
$D_H(\theta)$	Directivity of Antenna in H-plane (dBi)
$D_{co}^{45}(\theta)$	Co-polar Directivity of Antenna in $\phi = 45°$ plane (dBi)
$D_{xp}^{45}(\theta)$	Cross-polar Directivity of Antenna in $\phi = 45°$ plane (dBi)
$PeakXP$	Peak Cross-polar side lobe level normalized to co-polar maximum
k	Wave number in medium
k_o	Wave number in free space
f	Frequency
ω	Angular Frequency
λ	Wavelength
C_o	Speed of light in Vacuum
ϵ_r	Relative Permittivity
ω_o	Beam Waist Radius of Gaussian Beam
Z_o	Location of Beam Waist along z-axis w.r.t. Origin
V	Voltage
I	Current
R	Resistance
C	Capacitance
L	Inductance
T_o	Physical Temperature in Kelvin
k_B	Boltzmann Constant
T_N	Noise Temperature in Kelvin
L_c	Conversion Loss
f_t	Current gain cut-off frequency
f_{max}	Unilateral power gain cut-off frequency

Preface

Writing a PhD thesis is like collecting pearls from the ocean of knowledge and experience, and putting them together in a nice collage. During the five years of PhD studies, I have tried to gather know-how's and expertise from two different disciplines; mainly antenna and microwave engineering. I have always attempted to combine these different strengths to obtain better and efficient systems for various applications.

Recent advances in THz applications and on-going quest for making higher operating frequencies of transistors have opened up numerous opportunities for making integrated antenna-microwave systems. The use of THz frequencies for detection of concealed weapon by radar based imaging is one such application where blend of knowledge from various disciplines is of paramount importance. This has been the main focus of thesis where my background as an antenna engineer with basic knowledge of microwave suits very well.

The thesis first covers a brief introduction on THz applications and gives more details on THz imaging for security applications. For this work, the MMIC technology is predominantly used. Hence, in the chapter 2 a brief review is given on the available devices (HEMT/HBT) along with MMIC processes used in the work.

With this introduced in the chapter 3, the thesis draws attention towards the characterization of antennas both in GHz and THz region. In which the definitions of antenna efficiencies for different applications are described in depth. Later on, the chapter 4 discusses various different topologies of antennas which are compatible to the given MMIC process.

Chapter 4 is the major part of the thesis. The goal for writing chapter 4 is to make a collection of different antennas which are completely feasible to manufacture in MMIC technology and are fully compatible to process layer definitions. The antenna structures included are based on literature survey as well as my own work. My aim while writing this chapter is to compare these antennas in terms of ohmic, reflection and Gaussian coupling efficiencies so that reader of the thesis would get an idea which antenna to choose for a particular MMIC process. The overall goal is to integrate antennas and active circuits on a single MMIC for multi-functional frontends. Hence, for every antenna structure described in this chapter, the comments on possible interface between the antenna and the active circuits are given as well.

Even though with ft and fmax of transistors are exceeding 1 THz, the low noise amplifiers are still under experimental stage. Hence, a more appropriate choice is to combine antenna with either resistive or Gilbert Cell. This has been addressed in depth in chapter 5 of the thesis where different topologies of mixers are compared in terms of their conversion loss and required LO power. Such that, it becomes clear for a reader, both qualitatively and quantitatively, which mixer topology can offer better conversion loss for a particular MMIC process.

Finally, I have tried to gather discussion and conclusion based on my understanding and experience while working with antenna-mixer integration for THz imaging applications. At the time of writing this thesis, I am very much optimistic about integrated front-end based on MMIC technology for single pixel imaging. But for multi-pixel imaging, more work is required in terms of both antenna-optics engineering and mixer integration with reduced LO drive requirements. I have tried to put together these aspects for future work towards multi-pixel front ends. Even though challenging, I feel optimistic about linear arrays of pixels in near future.

During this thesis work, two more additional contributions are made. One for the characterization of antenna far-field in terms of Gaussian Coupling efficiency and one for the measurement of mixer noise figures exceeding 10 dB. Hence, two appendices

are included. The first one is about the comparisons of different definitions of the far-field of Gaussian beam. And the second one is the detail derivation of new 'N-times Signal Power Method' for the measurement of mixer noise.

I hope that this thesis have touched upon various aspects antenna-microwave-optics engineering required for multi-pixel THz imaging applications. And the reader would find it useful either as an introduction to this field or as a handbook to pick particular antenna + mixer topology for the design based on certain MMIC process.

With English as a foreign language, I often find myself making grammatical and typographical mistakes. Even then, I have tried my best to correct the text for such errors, with kind help from Vessen and Sumedh for proof reading, I apologies to the reader if such errors cause inconvenience in reading.

Yogesh Karandikar

Gothenburg, Sweden.

Introduction

The field of terahertz is relatively new compared to the traditional microwave engineering. It is now being defined as the field encompassing techniques, fabrication methods and devices operating in the frequency band of 300 GHz to 3 THz. This band covers sub-millimeter wavelengths ranging between $1\ mm - 100\ \mu m$. Even though the capabilities of generating and transmitting millimeter wave electromagnetic radiation had been demonstrated by Sir J. C. Bose as early as 1895 a few years before famous wireless transmission by Marconi; the use of these wavelengths for practical applications remain dormant for more than half a century [1, 2]. Many of the required THz components such as horns, polarization filters, cavity resonators, point contact diodes etc. were invented in their elementary form by Sir J. C. Bose in late 19th century, but it took considerable time for the advancement of semi-conductor technology that the use of THz frequencies became feasible for a variety of modern applications.

As time progressed, the THz frequencies found more and more attention due to numerous molecular spectral lines in this band carrying vital information for astronomy as well as atmospheric studies. Unarguably, radio astronomy played an important role as a driver for THz technology and components development [3]. But soon, the studies of atmospheric windows in these bands [4] as well as rapid advancements in the semiconductor processing capabilities opened up variety of new applications of THz or T-rays for communication, security and biomedical imaging.

Thus the rapid growth seen in the use of THz frequencies in the last 20 years, made THz engineering as a field in itself. Hence, in this chapter, first a brief review on various THz applications is given followed by different enabler technologies. The field of THz is vast and rapidly expanding in terms of applications, components, and technologies. Therefore the scope of this thesis is limited to the THz technologies which offer heterodyne mixing. For detailed descriptions of various other THz devices, reader can turn to review articles [5, 6].

This thesis work is mainly focused on integration of antennas and active receiver frontends at THz frequencies using MMIC technology with security imaging as a primary application. Thus it is important for such THz imaging systems to foresee the requirements, goals and corresponding active frontend hardware. Hence, this chapter concludes with the details of design goals for antenna integrated circuits for imaging.

1.1 Review of THz Applications

Undoubtedly, astronomy and atmospheric sciences were first to tap the potential of THz technology for the exploration of universe as well as our own mother earth. The strong absorption lines of water vapor at 183 GHz and 557 GHz were used for exploration of water in Universe and possibly life [3]. The absorption of THz radiation by water, Oxygen and other gases led to many space missions, since measuring the spectral lines of these molecules gave information about the surrounding temperature, pressure, gas velocities as well as magnetic fields within the observational region. For these applications, low noise radiometers were developed and deployed in space [7]. There are currently various operational THz instruments in space such as Odin,

Herschel and Planck [8]. Also ongoing work for radio telescope such as ALMA has been a major driver for low noise THz receivers in recent years [9].

Apart from scientific objectives, in recent times THz frequencies are gaining momentum in various other applications. Communication is one such area where large bandwidth requirements for high data rate can be achieved using THz frequencies. Even though the free space loss is high at THz frequencies, the high data rate exceeding 10 Gbps over short distances is of use for consumer products such as wireless HDTV video transfer, large file downloads from home server as well as for indoor WLAN or WPAN. This is gaining large attention recently and attempts are made to demonstrate practical THz radio with carrier frequency around 300 GHz [10, 11, 12].

Recently Biomedical engineering has started using THz frequencies for various medical applications such as disease diagnostic, recognition of protein states, tissue identification etc. The dielectric properties of many biological materials vary strongly in THz band. Thus absorption or reflection measurements of biological samples using broadband time domain systems, offers vital information for diagnosis [13].

THz pulsed systems offering imaging capabilities have also found use in inspection of Pharmaceutical products such as medicinal tablets. Many chemicals used for tablets have unique spectral characteristics which can be used to obtain structural information of tablet, its coating thickness, uniformity and chemical composition. The main advantage of using THz radiation here is the fact that it is non-ionizing. Also using reflection type systems a non-destructive testing of tablets can be performed. This is very helpful, both for quality control of the tablets during manufacturing as well as preventing counterfeit medicine in the market [14].

The non-ionizing properties of sub-millimeter waves along with high spatial resolution obtained from moderate aperture size have emerged in use of these wavelengths for surveillance and security applications. It is found that THz frequencies can penetrate clothing but get attenuated significantly by human skin. This makes them very attractive to use in airport security scanners for concealed weapon detection. The single pixel imaging radars based on frequency domain systems in reflection mode have been demonstrated around 0.6 THz [15, 16, 17, 18]. But still getting video rate imaging at large distances (> 20 m) with high dynamic range and contrast is an ongoing quest. Hence for these applications multi-pixel compact heterodyne frontends are needed. Passive radiometric systems using cryogenically cooled bolometers are also emerging for these applications [19].

With unique properties of THz spectra, the numbers of applications which can be thought of are countless. The use these frequencies have even come up in the inspection and preservation of historical artifacts such as paintings, pottery [20]. Thus exploration, research towards innovative THz technology is vital for the success of these applications. Attempts are also made by microwave engineers to cover THz frequencies by down scaling the devices such as transistors, Schottky diodes. On the other hand, photonics community is coming with new methods of generating and receiving broadband THz radiation. Thus soon the THz gap will be filled with modern devices and technologies to explore or rather exploit this part of electromagnetic spectrum. But to achieve this substantial multi-disciplinary research is needed.

1.2 Review of THz Technologies

As seen in the last decade, the explosion of THz applications came up with higher and higher demands on THz systems and technologies. The enablers of these technologies are various different devices capable of generating or detecting THz radiation. Many

applications described in section 1.1, are based on either frequency domain or pulsed time domain THz systems.

In time domain systems typically femto second laser pulses are used to shine antenna on III-V semiconductor substrates (GaAs, InGaAs) which in turn give rise to THz pulses covering broad spectra. These are often referred as photo conductive switches and are used in spectroscopic studies [6].

In frequency domain, either heterodyne or direct detection of THz radiation is possible. Various different types of devices such as bolometers, transition edge sensors (TES), kinetic inductance detectors (KID) etc can be used to measure power of THz radiation. But here considering the scope of thesis, more attention is given to the heterodyne systems. The details of direct detection techniques can be looked in articles [5, 6].

The Heterodyne receivers capable of retaining both amplitude and phase of the received signal offer advantage for THz systems in imaging and communication applications. At THz frequencies typically a heterodyne system consists of a local oscillator (LO) as a reference frequency, a mixer which multiplies incoming radiation with LO and an amplifier with band pass filer to extract Intermediate Frequency (IF) [21]. The performance of these heterodyne systems at THz is mainly governed by the mixer and hence choice of mixer plays key role for particular application. Very often for THz heterodyne systems the emphasis is given on a mixer design to minimize conversion loss and LO power requirement.

Thus to get better insight on the various different mixing devices and to understand their limitations in terms of noise, conversion loss etc, a brief review of key THz mixer technologies is given below.

1.2.1 Super conductor-Insulator-Super conductor (SIS)

These types of mixers can offer lowest noise and can operate up to ~ 1.3 THz. The SIS operation is based on photo assisted tunneling of quasi-particles (electrons) through insulating layer. With the application of photon on these junctions, the cooper pairs in the super conductor break giving free electrons to tunnel through insulators [21, 22]. Due to their low noise, these are widely used for radio astronomy applications. The state of the art SIS mixers have noise just few times the quantum limit ($h\nu/k_B$). The single side band (SSB) receiver using SIS has noise temperature of 100 K in $211 - 275$ GHz band [23] while the double side band (DSB) receiver has shown ~ 50 K noise temperature in $280 - 420$ GHz band [24]. Even though SIS based receivers show lowest noise performance, the need of cryogenically cooled systems makes them less suitable for consumer applications.

1.2.2 Hot Electron Bolometer (HEB)

The low noise properties of SIS junctions are limited by their upper frequency cutoff. This cutoff occurs when the photon energy becomes more than twice the bandgap of the junction ($h\nu > 4\Delta$). Thus there is a need of sensitive devices to cover upper end of THz spectrum ($1.3 - 3$ THz). Hence, in this band Hot Electron Bolometers (HEBs) are more commonly used. The HEB mixers are thermal detectors in which the temperature changes caused by the absorption of incident radiation significantly alters the resistance of biased sensor near its superconducting transition [6].

The state of the art HEB mixers offer noise temperatures of the order of 20 times the quantum limit (~ 2200 K @ 2.5 THz [25]) and they also operate at much lower LO power levels. This is an advantage since generating high power, stable LO sources

above 1 THz is in itself an active subject of research. The RF impedance of HEBs is primarily real and octave bandwidths can be achieved. As an practical example, the measured DSB noise temperature for HEBs used in Herschel Space observatory are 1100 K and 1450 K in 1.63 and 1.89 THz bands respectively [26].

1.2.3 Schottky Diode

These are versatile devices used for both generation and detection of THz frequencies. In principal it is a junction formed at the interface of a metal and a semiconductor and traditionally made as a Whisker contact in which the thin metal tip touches the epitaxially grown semiconductor surface. But nowadays, the Schottky diodes are planarized and anode contact is formed by using an air-bridge. The multipliers made out of Schottky diodes can offer few mW of power in the lower end of THz spectrum while $10 - 100$ μW in the range of $1 - 2$ THz [27]. And these are widely used as LO sources for mixers.

While using these diodes for mixer applications, both fundamentally and sub-harmonically pumped mixers are feasible. A fundamentally pumped DSB mixer using these diodes having 2700 K noise temperature and ~ 9 dB conversions loss has been demonstrated at $835 - 900$ GHz band and it requires ~ 1 mW of LO power [28]. For a sub-harmonic case, the DSB noise temperature of ~ 900 K with conversion loss $6 - 7$ dB in $300 - 360$ GHz band has been achieved using $2 - 4$ mW of LO power [29].

In case of image rejection type of mixers, the state of the art Schottky diodes based receiver has been demonstrated for SSB noise temperature of ~ 3000 K with 4 mW sub-harmonic LO pumping in $320 - 360$ GHz band recently [30]. Thus Schottky diodes based source/receiver is a competitive technology in THz band and its room temperature operation make it a suitable candidate for security imaging applications.

1.2.4 Transistors

As compared to other technologies, researchers are rapidly improving transistors to cover THz band by shrinking their size and integrating them with other passive components such as resistors, capacitors and inductors using MMIC technology and it is now being referred as TMIC (T-Tera) or SMMIC (S-sub millimeter wave).

In principle various topologies of mixers utilizing transistors operating at microwave region can be made at THz frequencies if the f_t and f_{max} of the transistor are above 1 THz. Both High Electron Mobility Transistors (HEMT) ($f_{max} = 1.2$ THz [31]) and Heterojunction Bipolar Transistors (HBT) ($f_{max} = 0.8$ THz [32]) are in rapid development stage for THz frequencies. Even though with these transistors amplifiers are feasible, their noise figures are varying from $2 - 10$ dB over THz band [33]. And still integrating LNA+ mixer for low noise frontend is a challenging task. But these technologies offer the biggest advantage of monolithically integrated circuit in contrast to SIS, HEB or Schottky. More details on these transistors will be covered in Chapter 2.

1.3 Frontend Goals for Multi-pixel Imaging System

The major work carried out in this thesis is towards the development of MMIC based frontends for THz security applications. In this application the goal is to reconstruct 3-D image of a human for detection of concealed weapons, explosive etc using reflection based active systems. Here, the non-ionizing THz radiation around 340 GHz is used
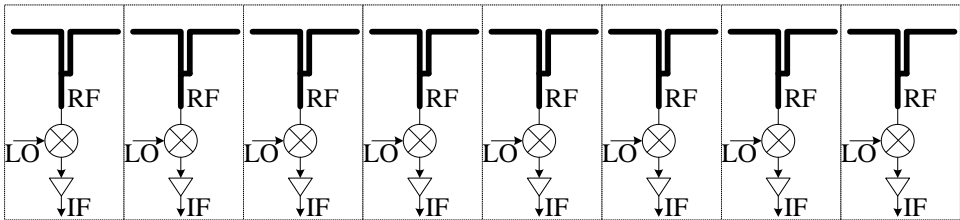
Figure 1.1: Concept of linear array of Antenna Integrated Heterodyne Receivers

to illuminate the subject and the reflected or backscatter field is measured over large distances (> 20 m).

The amplitude of the reflected signal is used to generate false color image while the phase is used to estimate distance. Hence, in principle these systems are analogous to bi-static radars and require heterodyne frontends. This type of systems even though demonstrated earlier [15, 16, 17, 18], they require multiple pixels to achieve practical video rates. Here, each pixel corresponds to one heterodyne receiver integrated with planar antenna using MMIC technology. This has resulted in the vision of monolith-ically integrated N x 1 linear array of pixels capable of generating N parallel beams which in turn would result N times improvement in the image acquisition rate. This concept is shown in Fig. 1.1. The overall system goals are summarized below.

- Linear Array of 8x1 monolithically integrated pixels.

- Target Frequency of 340 GHz with $\sim 10\%$ (30 GHz) bandwidth.

- Gaussian Coupling Efficiency of Integrated Planar Antenna $> 70\%$.

- Sub-harmonically pumped mixer with $L_c < 15$ dB.

- Integrated x3 or x4 multiplier with output power $\sim 3 - 4$ dBm @ 170 GHz.

- Integrated IF amplifier with Gain > 20 dB and $1 - 15$ GHz bandwidth.

The criterion for pixel separation is largely governed by the focusing quasi-optics used after the MMIC. Therefore, pixel size of $1 - 2\lambda$ is estimated considering the physical dimensions of the complete MMIC. The intended use of such multi-frontend MMIC receiver for security systems is shown in Fig. 1.2.

In this thesis, emphasis is more given on the design of single pixel based on various feasible antenna + mixer topologies and the appended papers show the implementation of practical pixel using MMIC technology.

With modern THz transistors, the individual component seems feasible but higher level of integration is ongoing research. Different challenges such as LO distribution, DC connections, packaging, antenna mutual couplings and efficient coupling to optics needs to be addressed in depth for a useful frontend in practical system.
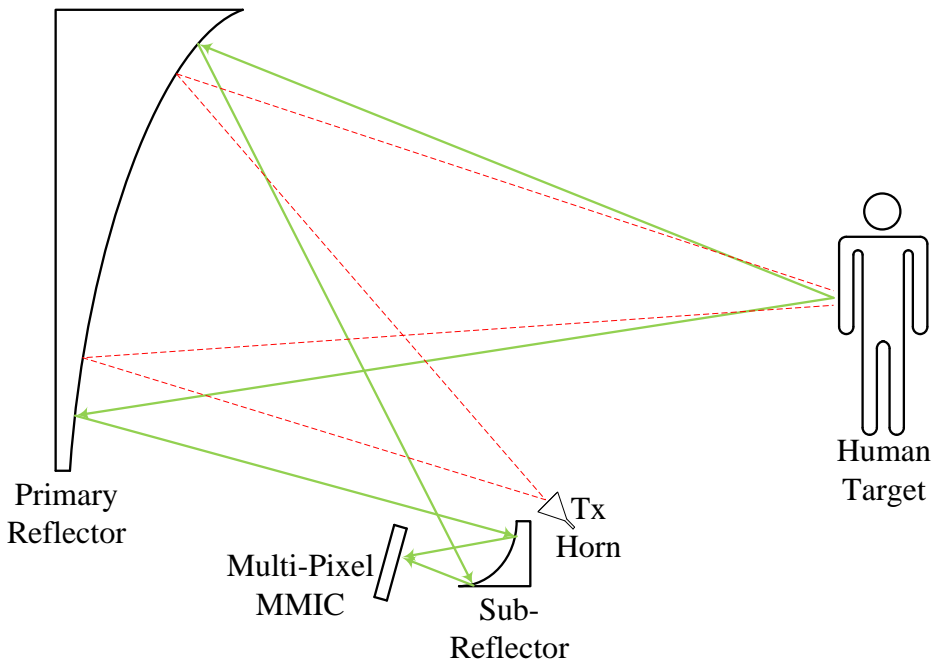
Figure 1.2: Impression of Multi-Pixel THz Imaging System for Security Applications

CHAPTER 2

MMIC Processes for HEMT/HBT Devices

Monolithically Integrated circuits (MIC) can be referred as one of the key technological achievements of the 20th century. The ability of MIC technology to integrate multi-function analog as well as digital circuits on a single chip has resulted in improved performance and smaller sizes of the electronic devices.

The term MMIC is usually associated to MIC which could operate at microwave frequencies and it contains monolithic integration of microwave transistors with other passive components such as capacitors, resistors, inductors and transmission lines. Even though earlier attempts were made to obtain MMIC using Silicon technology, the practical MMIC picked up the pace only after the first demonstration of the X-band amplifier using GaAs as substrate in 1976 [34, 35, 36].

Since then both bipolar and field effect transistors are grown using MMIC technology with predominant use of III-V semiconductors having higher electron mobilities. Currently, considerable progress has been made in the transistors using GaAs or InP as a semi-conductor substrate and the operating frequencies of these transistors have been pushed into the THz region using device scaling as well as careful material bandgap engineering of heterostructures [37].

The main advantage of using MMIC approach for THz application is that the entire transmitter/receiver can be fabricated on a single chip. This simplifies the interface at RF and LO frequencies. Also MMIC is easier to integrate in the system since lower input or output frequencies such as IF can be transferred relatively easily in microstrip or co-axial technology. Since both active as well as passive components are fabricated on the same semiconductor substrate, the parasitics associated with individual components can be minimized. This results in the designing of the more complex circuits with wider bandwidths and higher operating frequencies.

The cost associated with the initial setup, research and development for MMICs is very high. Also it takes considerable time for a MMIC process to mature so that it can offer reliable circuits with high yield. Even with these aspects, for mass production, the cost/MMIC can come down, but still space is premium and often a circuit designer has to work towards the minimization of the physical area of the circuit. Even with these limitations, MMICs are under rapid development stage to offer advanced transistors operating in THz region.

The work carried out in this thesis, predominantly uses MMIC processes available from Teledyne Scientific Company[1] using InP substrate material. For higher cutoff frequencies, heterojunction bipolar transistor (HBT) as well as high electron mobility transistors (HEMT) are used. Hence, the goal of this chapter is to introduce briefly HBT and HEMT devices and their relevant performance parameters using state of the art MMIC process. Further in the chapter, the MMIC layer topology is introduced along with typical process parameters which are relevant for the antenna as well as circuit design. In subsequent chapters, these layer definitions will be used to elaborate different feasible antenna and mixer topologies using these MMIC processes.

---

[1] http://www.teledyne-si.com

2.1   HBT Device

A heterojunction device is the device in which the junction of at least two semi-conductor materials is formed having different band gaps in terms of conduction or valance band. For Heterojunction bipolar transistor usually base-emitter junction is made out of different band gap materials, but in Double Heterojunction bipolar transistor (DHBT) both base-emitter as well as collector-base junctions are hetero-junctions.

The basic advantage of using heterojunctions in BJT was pointed out in patent application way back in 1948 [37], but the first HBT devices using SiGe only appeared during 1987 [38] and since then they are getting improved radically in terms of size and performance.

Usually in the HBT device the emitter has larger band gap than the base, this suppresses the injection of holes from base to emitter which helps in having highly doped base, reduced base resistance and higher gain cut-off frequencies. A typical structure of HBT is shown in Fig 2.1. It has buried n-type collector layer under p-type base. The top layer is the n-type highly doped emitter layer having different band gap than base forming the heterojuction. The behavior of DHBT device is analogous to BJT but with improved frequency response and lower noise. The typical I-V characteristics of the 250 nm emitter width DHBT [39] (from Teledyne Scientific Company) used in this work are plotted in Fig. 2.2a. This device has DC current gain $\beta \sim 25$.
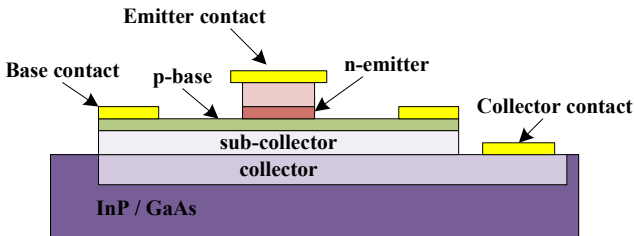
Figure 2.1: Typical Layer Structure of HBT

Apart from the I-V characteristics, min. noise figure (NF_{min}), stability factor (k), AC current gain (h_{21}) and unilateral power gain (U) are the parameters to be looked at for high frequency characterization of the device. Also the current gain cut-off frequency (f_t) and unilateral power gain cut-off frequency (f_{max}) are important since they define upper frequency limit on the operation of the device. The f_t and f_{max} are obtained by extrapolating h_{21} and U respectively with $-20\ dB/decade$ roll off. The definition of h_{21} and U is given in (2.1,2.2) [37, 40] and for 0.25 x 4 μm device the extrapolated values of f_t, f_{max} are shown in Fig. 2.2b.

$$h_{21} = \frac{-2S_{21}}{(1 - S_{11})(1 + S_{22}) + S_{12}S_{21}} \qquad (2.1)$$

$$U = \frac{|Y_{21} - Y_{12}|^2}{4\left[Re(Y_{11})Re(Y_{22}) - Re(Y_{21})Re(Y_{12})\right]} \qquad (2.2)$$

The recent results for 130 nm DHBT devices show f_t, f_{max} of 0.52, 1.1 THz respectively [41]. This shows the potential in these devices to cover THz region.

(a) IV Characteristics   (b) Extrapolated f_t and f_{max}
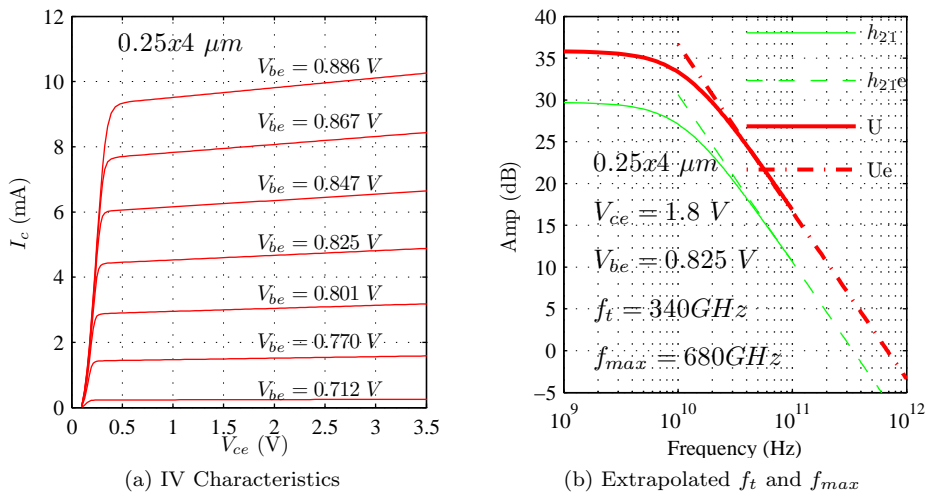
Figure 2.2: Characteristics of 0.25 x 4 μm device of TSC 250nm InP DHBT Process

2.1.1 Teledyne 250nm DHBT MMIC Process

This process is based on 250nm DHBT device [39] and has multiple metal interconnect layers. The layer topology of this process is shown in Fig. 2.3. The four metal interconnect layers (MET1-MET4) are separated by $2\mu m$ thick Benzocyclobuten (BCB) dielectric layer having permittivity $\epsilon_r \sim 2.7$. The subsequent metal layers can be shorted using plated via holes. Thus this process offers possibilities to have complicated layouts in relatively smaller physical area.

The active devices are DHBTs with typical sizes of 0.25 x 2 μm, 0.25 x 4 μm and 0.25 x 10 μm. For passives similar to HEMT MMIC process, NiCr thin film resistors with sheet resistance of $50\Omega/sq$ are available along with Metal-Insulator-Metal (MIM) capacitors with capacitance of 0.3 $fF/\mu m^2$. The spiral inductors using multiple layers are also feasible. Typically circuits can be designed with MET1 or MET 2 as ground with MET3 or MET4 for signal. The lack of back metallization makes it difficult to ground the chip in the package. Thus special attention is required for grounding of chip to the external circuits.

2.2 HEMT Device

The High Electron Mobility Transistors are similar in operation as that of Field Effect Transistors. In these transistors, the channel layer having lower band gap is placed below the barrier layer having higher band gap. This type of placement of layers, forms the heterojunction causing high concentration of electrons near the interface. Since electrons are very much confined near the interface in the channel layer, they are referred as 2-dimensional electron gas (2DEG). The 2DEG electrons are spatially separated from the donors. This results in reduced ionized impurity scattering and higher electron mobilities [37, 33]. The Schottky gate contact formed above the barrier layer then control the flow of electrons in the channel. The basic layer structure of HEMTs is shown in Fig. 2.4.
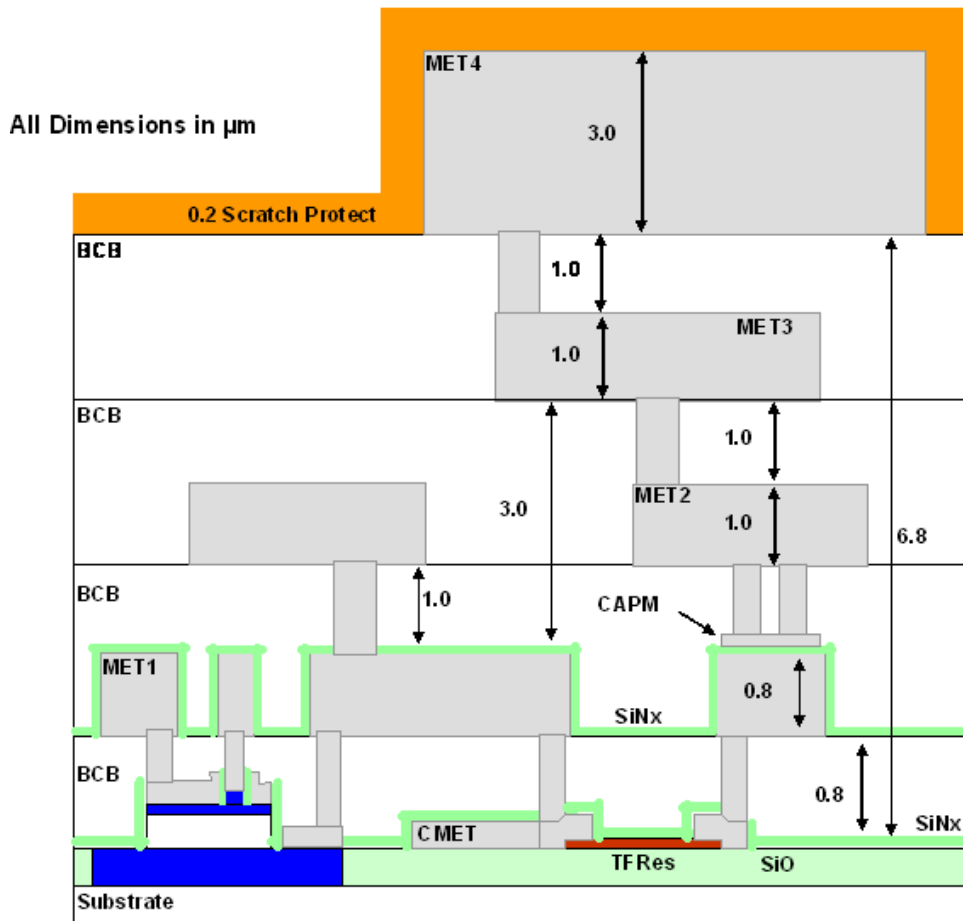
Figure 2.3: Layer Topology for DHBT MMIC (Reprinted with permission from Teledyne Scientific Company)
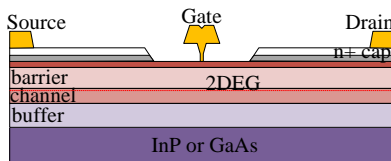
Figure 2.4: Typical Layer Structure of HEMT

The very first HEMT device originated after the studies of heterojunctions formed by thin layers of n-type AlGaAs and undoped GaAs, and subsequently by introducing a Schottky gate on AlGaAs surface during 1980s [42].

In a common source configuration of the device, at the negative potential applied to the gate, the E-field originated from the gate penetrates deeply in the semi-conductor layers causing depletion of electrons in 2DEG. This results in high channel resistivity and very low current flows from Drain to Source terminal. For positive Gate-Source (V_{GS}) voltages with certain positive Drain-Source voltage (V_{DS}), the electron concen-

(a) IV Characteristics: I_D Vs. V_{DS}

(b) IV Characteristics: I_D Vs. V_{GS}
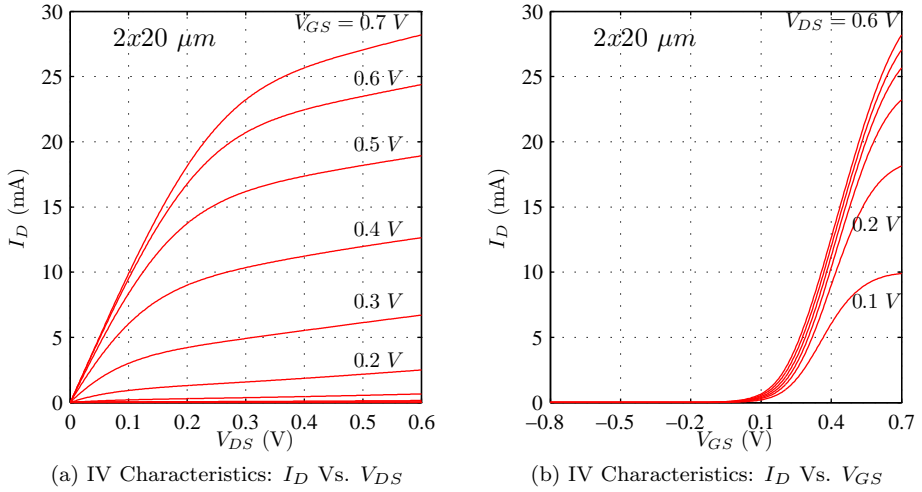
Figure 2.5: DC Characteristics of 2 x 20 μm device of TSC 50nm InP HEMT Process

(a) Transconductance

(b) Extrapolated f_t and f_{max}
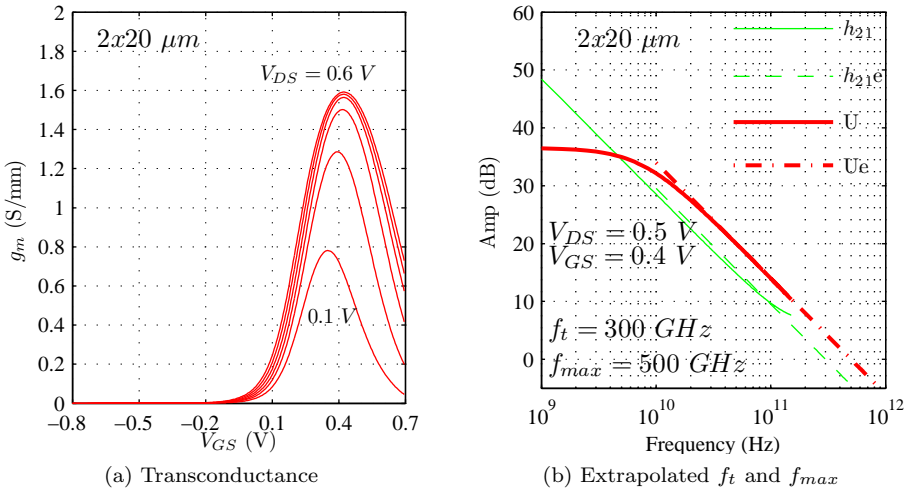
Figure 2.6: g_m, f_t & f_{max} of 2 x 20 μm device of TSC 50nm InP HEMT Process

tration in the 2DEG increases and drain current (I_D) is established. Thus I_D depends on both V_{DS} & V_{GS} as shown in Fig. 2.5 for 2 x 20 μm 50nm gate length device [43]. Apart from device I-V, its transconductance (g_m) and f_t & f_{max} are useful parameters which are shown in Fig. 2.6.

In recent years, rigorous attempts were made to push f_t & f_{max} of these devices towards 1 THz. The brief summary of recently reported cut-off frequency values are shown in Table 2.1. Thus the trend indicates the potential of HEMTs to become a widely used THz transistor as well as attractive device for Low Noise Amplifiers in this band [33].

Table 2.1: Reported f_t & f_{max} values of HEMT Devices

HEMT type	Gate Length (nm)	f_t (GHz)	f_{max} (GHz)	Year	Ref.
Metamorphic	50	340	–	2005	[44]
Pseudomorphic	30	631	331	2008	[45]
Pseudomorphic	40	591	394	2008	[45]
Pseudomorphic	50	557	718	2008	[45]
Pseudomorphic	30	644	681	2010	[46]
Enhancement	50	465	1060	2010	[43]
Metamorphic	40	688	800	2011	[47]
Metamorphic	30	600	1200	2011	[31]

2.2.1 Teledyne 50nm HEMT MMIC Process

This process is based on 50 nm HEMT device as described in [43]. The substrate is Indium Phosphide (InP) with dielectric constant $\epsilon_r \sim 12.5$ with thickness of 50 μm (optional 75, 100 μm). For device as well as passive connections two interconnect Gold (Au) layers are available namely MET1 ($\sim 0.8~\mu m$) and MET2 ($\sim 2.0~\mu m$). The backside metallization (STREET) is done with Au with thickness of ($\sim 3~\mu m$). The Au plated substrate vias with typical diameter of 60 μm are available as well. This layer structure is shown in Fig. 2.7 (HEMT features are suppressed).
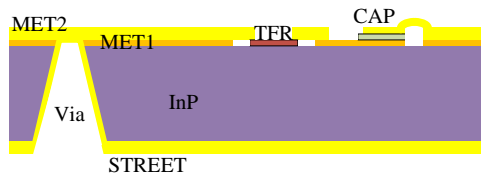
Figure 2.7: Layer Topology for HEMT MMIC

The active devices are HEMTs with typical sizes of 2 x 20μm, 4 x 20μm, 2 x 50μm and 4 x 50μm. For passive devices, NiCr thin film resistors with sheet resistance of 50Ω/sq are available along with Metal-Insulator-Metal (MIM) capacitors with capacitance of 0.3 $fF/\mu m^2$. The spiral inductors are feasible due to availability of air bridge up to 30 μm in length.

Antenna Characterization

As seen in earlier chapters the THz band is getting widely used for various applications and the transistor technology is already getting mature for the lower end of THz spectrum. This opens up opportunities to integrate both passive antenna structures as well as active circuits on a single MMIC for transmit/receive architecture. Also considering the complex processing techniques of MMIC, the degrees of freedom for antenna designs are less and often antenna designs using MMIC technology are constrained to the MMIC layer topologies and thicknesses. Hence, while developing antenna structures which are compatible to MMICs, it is important to characterize those structures in terms of their loss, matching and radiation patterns. And depending upon the application, importance should be given to the appropriate parameter.

Therefore the goal of this chapter is to introduce first the antenna properties, characterization definitions along with few application examples. And further develop an quantitative as well as qualitative understanding of the challenges in MMIC antenna designs for THz applications.

The foremost characteristic of an antenna is its ability to convert applied excitation (voltage/current) to radiated waves. Thus it can be referred as the transducer between guided waves to free space electromagnetic waves. This directly translates to its size being proportional to the wavelength of the radiation. Also the way radiation occurs from an antenna is characterized by its radiation pattern and further more by terms such as directivity, side-lobe level, cross-polarization level and front to back ratio [48, 49, 50]. The overall goal with antenna design is to optimize the geometries such that antenna structure radiates most of the radiated power in the desired direction while maintaining low losses and good input matching.

3.1 Directivity

The directivity quantifies the ability of an antenna to focus radiation in the given direction in space. Hence, it is considered as the ratio of the power radiated by antenna in the observation direction (i.e. at certain θ, ϕ in spherical coordinate system) to the power radiated by an isotropic radiator in the same direction. The directivity has upper maximum limit based on the antenna size. If D is the diameter of antenna aperture then max. directivity (D_{max}) is given by (3.1) [48]. This occurs when the E-field over the antenna aperture is uniform in amplitude and phase. Thus a 3λ diameter circular aperture gives $D_{max} \sim 20 \ dBi$ and corresponding side lobe level of -17.6 dB is obtained, as shown in Fig. 3.1 [50].

$$D_{max} = 10 \log_{10} \left[4\pi \frac{\pi D^2/4}{\lambda^2} \right] \quad (dBi) \tag{3.1}$$

The purpose of putting this example is to highlight the fact that maximized Directivity occurs when E-field over an antenna aperture is uniform and this also results in increased side-lobe levels. In many practical applications such as radio astronomy, satellite communication and THz quasi-optical systems, low side-lobe levels are required which are achieved by tapering the E-field distribution over the aperture.

(a) 3-D Copolar Radiation Pattern (b) $\phi = 45°$ plane copolar pattern
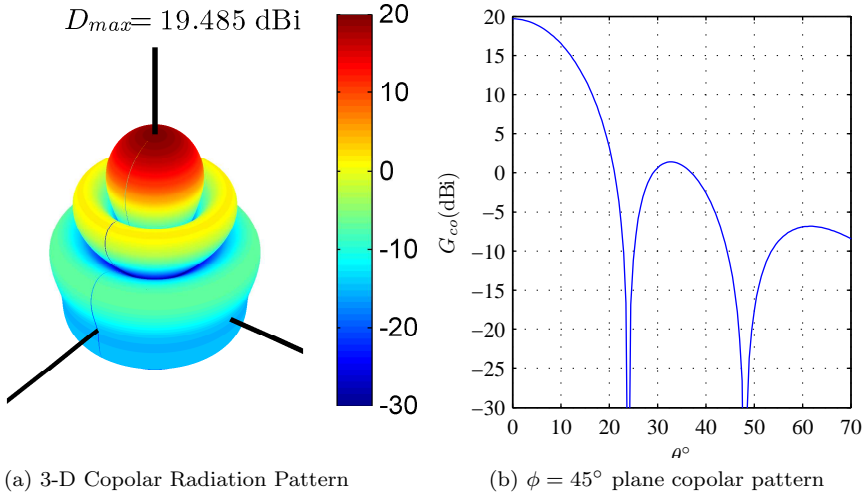
Figure 3.1: Radiation Patterns of Uniform Circular Aperture with $D = 3\lambda$

This indicates that Directivity can not be maximized at the same time with the minimization of the side-lobes for given physical area of the antenna. This translates to efficiency trade-offs and are more relevant for MMIC based antenna design where physical size of an antenna is an issue due to increased cost.

Therefor in this chapter, after defining basic antenna efficiency terms namely ohmic and reflection, more application specific aperture and gaussian coupling efficiencies are defined. And finally the trade-off between aperture efficiency and Gaussian Coupling Efficiency is explained.

3.2   Ohmic Efficiency

The ohmic efficiency is directly associated with the losses in the antenna structure and therefore it is defined as the ratio of total radiated power to the accepted power by antenna at its input terminal [48]. This efficiency is also regarded as the ratio of antenna gain to directivity. The ohmic losses inherent to antenna building materials dictate ohmic efficiency value since it is simply the addition of dielectric and conductor losses in the antenna structure.

$$\eta_{ohmic} = \frac{P_{rad}}{P_{accepted}} = \frac{Gain}{Directivity} \tag{3.2}$$

The ohmic efficiency can be estimated by doing careful antenna pattern measurements in the anechoic chambers or by using excited modes inside a shielded metallic cavity referred as the reverberation chambers (RC). In the traditional anechoic chambers, antenna radiation patterns, input impedance and ohmic efficiency can be measured but antenna characterization is limited to the line-of-sight (LOS) type of environment. While with RCs, except radiation pattern all other antenna parameters can be measured. The main advantage of using RCs for antenna efficiency estimation is its speed and comparatively low cost. Also RCs can support rich multi-path environments which are more realistic for consumer mobile communication applications and

more application specific parameters such as Diversity Gain, MIMO channel capacity can be measured using RC [51].

3.2.1 Reverberation Chamber

In its simplest form a reverberation chamber is an over sized, well shielded metallic cavity which can support many resonant modes close to the frequency of measurement. Such a cavity can be used to produce statistical field distribution when excited by the antennas inside the cavity and by mechanically stirring or perturbing the cavity by different means. The statistical field distributions can be made very similar to the real-life multipath scenarios experienced by mobile terminals.

The typical measurement setup using RC involves the Antenna Under Test (AUT) inside the chamber as a receive antenna with one or more transmit antennas along with a network analyzer. The complex transmission between these antennas is measured. The accuracy of measurement depends upon the number of independent complex measurements and the number of independent samples depend upon the number of excited modes in the chamber. For a rectangular cavity with no losses, each mode can be described as the sum of eight independent plane waves. Thus, the number of independent samples are a factor of eight larger than the number of excited modes in the cavity [52]. Therefore, with more number of excited modes more uniform environment is experienced by the AUT.

Here, it could be misleading that a spherical cavity having many number of degenerate modes would result in high accuracy of measurement. But this is in fact contrary to the study conducted during this thesis as mentioned in **Paper H**. The conclusion of this study suggests that a cavity with more irregular shape can give more uniform distribution of modes as a function of frequency and high accuracy in estimating radiation efficiency. Thus a cavity having less number of degenerate modes is required for RC. Such cavity has more independent plane waves giving more uniform environment inside it. Hence, a rectangular cavity outperforms cylindrical or spherical cavity when its used as a RC. And the RC build around rectangular cavity (for e.g.[1]) can measure radiation efficiency with accuracy better than 0.5 dB.

3.3 Reflection Efficiency

The antenna has certain impedance at its input terminals. Thus for maximum power transfer from the generator to the antenna, the antenna impedance should be matched to the system characteristics impedance (Z_o). If Γ_A is the reflection coefficient for antenna impedance Z_A then antenna's reflection efficiency is defined as in (3.4). Thus it is a ratio of power accepted by antenna terminals to power available from generator.

$$\Gamma_A \quad = \quad \frac{Z_A - Z_o}{Z_A + Z_o} \tag{3.3}$$

$$\eta_{refl} \quad = \quad 10 \log_{10} \left[1 - |\Gamma_A|^2 \right] \tag{3.4}$$

3.4 Aperture Efficiency

Every antenna has an effective area (A_e) over which it receives the power from the incoming plain wave having certain power flux density (W/m^2). The output power is

---

[1]`www.bluetest.se`

simply the multiplication of antenna effective area with incoming power flux density. The effective area of an antenna is same as that of the physical area when the aperture field has uniform distribution of E-field resulting in maximized directivity. The relationship between D and A_e is given in (3.5) [48].

$$D = 4\pi \frac{A_e}{\lambda^2} \tag{3.5}$$

In its simplest form the aperture efficiency is defined as the ratio of maximum effective antenna area to its physical area and is given by (3.6) [48]. This definition translates to the efficiency with which antenna can couple power from incoming plane wave to its output terminals.

$$\eta_{ap} = \frac{\max A_e}{A_{physical}} \tag{3.6}$$

In many practical antenna applications, aperture efficiency is an important characterization parameter and maximizing its value is often considered as one of the goals in the design. The applications using prime focus reflector, offset fed reflector or Cassegrain reflector systems require the feed antenna along with the reflector to be characterized in terms of aperture efficiency. The use of such systems is very common for radio astronomy, satellite communication and base station microwave backhaul links for mobile communication.

Therefore, the term aperture efficiency in the reflector antenna system depends upon both the radiation patterns of the feed antenna as well as the $^f/_D$. The maximization of the η_{ap} for reflector antennas comes with trade-offs. The maximized η_{ap} occurs for uniform E-field distribution over an aperture. For this ideally an isotropic radiator is needed giving equal amplitude of E-field radiated in all directions. This type of isotropic antenna is not possible to realize in practice and threfore a practical feed pattern having finite directivity introduces the tapered E-field distribution over an aperture.

This translate to well-known spill-over and illumination efficiency trade-off as shown in Fig. 3.2a. Since having a low directivity feed achieves more uniform distribution over reflector aperture giving higher illumination efficiency at the expense of radiating more power outside the reflector resulting in spill-over loss. Hence the aperture efficiency becomes the product of spill-over and illumination efficiency.

To illustrate this trade-off further a rotationally symmetric feed pattern as given in (3.7) is chosen and the directivity values between 7-15 dBi are chosen along with a prime focus reflector having $^f/_D = 0.433$. The numerically computed values of illumination, spill-over and aperture efficiencies are plotted in Fig. 3.2b.

$$G(\theta, \phi) = \cos^n \left(\frac{\theta}{2}\right) \left[\sin\phi\hat{\theta} + \cos\phi\hat{\phi}\right] \tag{3.7}$$

It is seen from Fig. 3.2b that the maximized η_{ap} of $\sim 80\%$ can be achieved for feed directivity of 9.25 dBi. This translates to the E-field taper of 9.26 dB at the edge of the reflector. Similar computations are performed for other practical $^f/_D$ ratios for reflector and the optimum directivity, taper values are summarized in Table 3.1. Thus even with ideal feed pattern having equal E- and H-planes, zero cross polarization and perfect rotational symmetry in pattern, the theoretical maximum η_{ap} does not exceed $\sim 80\%$.

Therefore for a practical feed pattern having finite levels of cross-polar components and with less rotationally symmetric beam; the η_{ap} degrades further. Also the practical

(a) Prime Focus Reflector with Feed Pattern

(b) η_{spill} and η_{ill} trade-off
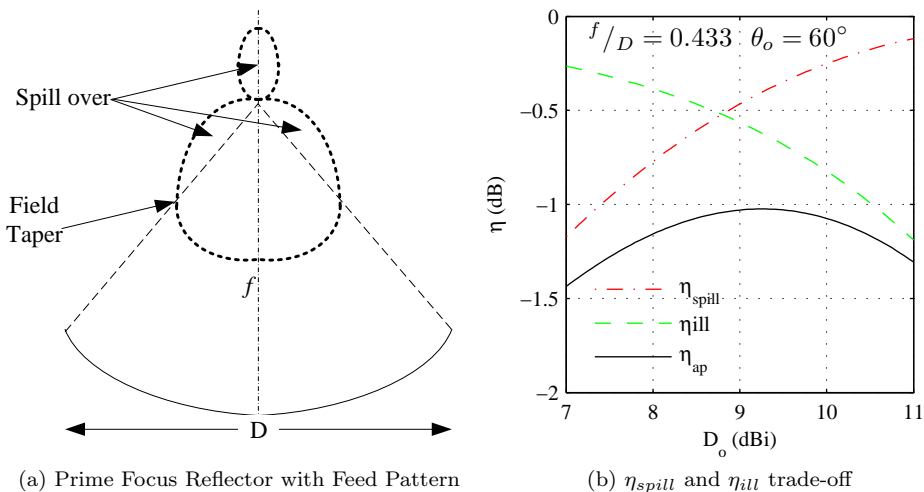
Figure 3.2: Influence of Feed Pattern and $^f/_D$ ratio of reflector on η_{ap}

feed pattern does not having uniform phase of radiated E-field. This causes non-uniform phase distribution on aperture and results in further degradation of η_{ap} value. Thus in practice, polarization efficiency, phase efficiency and Body of Revolution-Type 1 (BOR_1) efficiency become additional sub-efficiency terms in the aperture efficiency calculations [50, 53, 54, 55].

The BOR_1 sub-efficiency basically quantifies the amount of power radiated by an antenna in first order ϕ-variations in the pattern. The power radiated by antenna in higher order modes does not contribute to on-axis directivity after the reflector [56]. Therefore radiation in the higher order ϕ-variations of pattern is a loss ad results in reduction of directivity.

Finally accumulating these arguments together the aperture efficiency becomes a product of several different sub-efficiencies as given in (3.8). The exact definitions of these terms are given in *Appendix A*.

$$\eta_{ap} = \eta_{BOR1} \cdot \eta_{spill} \cdot \eta_{pol} \cdot \eta_{ill} \cdot \eta_{\o} \qquad (3.8)$$

Putting it all together for a practical feed+reflector antenna systems the total efficiency then becomes the product of η_{ap} along with ohmic and reflection efficiency as given in (3.9).

$$\eta_{total} = \eta_{ohmic} \cdot \eta_{refl} \cdot \eta_{ap} \qquad (3.9)$$

3.4.1 η_{ap} studies of Two Parallel Dipoles above Ground Plane

Corrugated horns are well known for being used as a feed for reflector for their low cross-polarization levels and rotationally symmetric beams. But these horns are often bulky and require precision machining for corrugations. Thus if similar patterns as that of corrugated horns are achieved with relatively simple antenna geometry such as two parallel dipoles above ground plane then solution becomes more attractive in terms of manufacturing as well as cost issues.

Table 3.1: Optimized D_o and Taper values for maximized η_{ap}

θ_o (°)	f/D	η_{ap} (dB)	D_o (dBi)	$Taper$ -(dB)
45	0.6036	-0.96	11.92	10.01
50	0.5361	-0.98	10.95	9.78
55	0.4802	-1.00	10.07	9.54
60	0.4330	-1.02	9.25	9.26
65	0.3924	-1.05	8.49	8.97
70	0.3570	-1.08	7.77	8.64
75	0.3258	-1.11	7.09	8.28
80	0.2979	-1.15	6.45	7.91

(a) Linear Dipoles   (b) Circular Dipoles
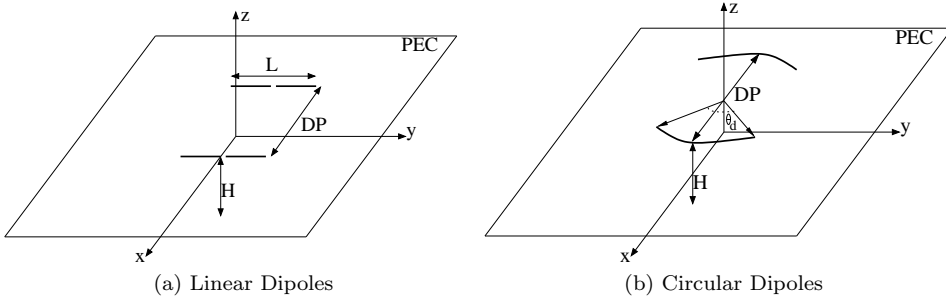
Figure 3.3: Geometry of two parallel dipoles above ground plane

The **Paper G** of this thesis tries to quantify a simple geometry of two parallel dipoles above ground plane as a feed for reflector by using η_{ap} as a measure. The basic geometry using linear as well as curved dipoles is shown in Fig. 3.3. The feed pattern, formed by in phase excitation of these two parallel dipoles, can be altered by changing the separation DP and height H above the ground plane.

The patterns for both these geometries are numerically computed and characterized in terms of various sub-efficiencies. It is found that both geometries can produce rotationally symmetric pattern having $\eta_{BOR1} > 97\%$, but the peak cross-polarization levels are better with curved dipoles.

Further more, it is found that maximum η_{ap} of $\sim 80\%$ can be achieved by carefully choosing the geometrical parameters DP and H for many practical values of f/D of prime focus reflector. And these optimum values are summarized in **Paper G**.

The effect of finite size ground plane is also studied. Since having bigger size ground plane increases aperture blockage, its size becomes a trade-off for aperture efficiency. The numerically computed patterns[2] of these two basic geometries for several different ground plane sizes indicate that the ground plane size of $\sim 1\lambda$ is optimum. With this size, the η_{ap} is reduced by a factor of $0.6 - 0.8$ dB from its maximum value of ~ -1 dB.

For more quantitative judgement, the aperture efficiency values using optimized patterns from these geometries are obtained for $f/D = 0.5361$ ($\theta_o = 50°$). The finite size circular ground plane with diameter of 1.2λ is used in computations. The 3-D patterns from these geometries are shown in Fig. 3.4. The aperture efficiencies from

---

[2]using WiPl-D: www.wipl-d.com
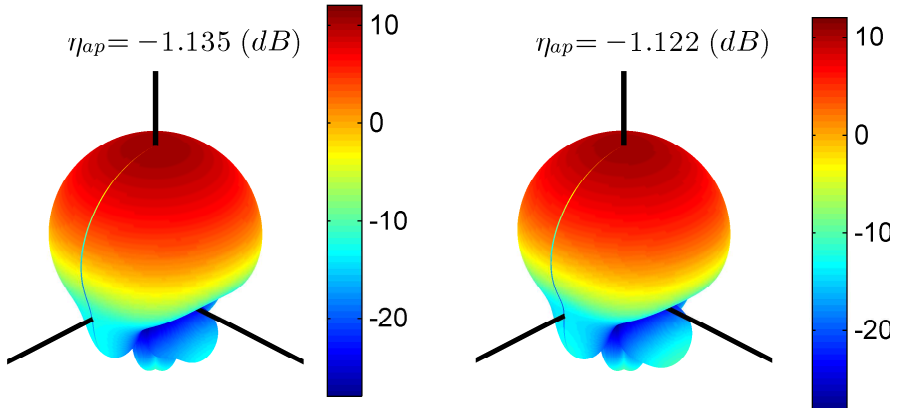
(a) Linear Dipoles ($DP = 0.48\lambda$ & $H = 0.18\lambda$) (b) Circular Dipoles $DP = 0.525\lambda$ & $H = 0.225\lambda$

Figure 3.4: 3-D radiation patterns for Linear and Circular Dipole Geometries

linear and circular dipoles are -1.135 dB and -1.122 dB respectively. For comparison, the corrugated Choke Horn [57] offers $\eta_{ap} = -1.055$ dB for the same $^f/_D$ of prime focus reflector. Thus it is very promising that these geometries can give a competitive performance as a feed for a reflector antenna.

The practical implementation of this geometry using folded dipoles is described in [58]. In this design a dual band feed in X- and Ka-band is fabricated. The lower X-band is covered using circular folded dipole geometry similar to Fig. 3.3b. The aperture efficiency better than -2.5 dB is achieved in practice due to limited ground plane size and higher dipole separation to incorporate Ka-band Choke Horn.

3.4.2 The Eleven Feed

As seen in earlier section, the simple dipole based geometry can perform well as a feed for reflector. But dipole being a resonant structure, the single dipole based designs are inherently narrow band. To overcome this limitation, the dipoles in Fig. 3.3a can be replaced with the two parallel log-periodic arrays of folded dipoles. By doing so, the pattern stays relatively constant over a large frequency bandwidth and at the same time log-periodic variation of impedance is achieved. Thus the newly modified geometry offers a broadband feed for reflector antennas.

This geometry offers ~ 11 dBi directivity along with $\sim 10 : 1$ bandwidth for ~ -11 dB input matching and hence it is referred as 'Eleven Feed' [59, 60, 61]. The main feature of this feed is that its phase center variation is very small over broad bandwidths which minimizes the de-focusing loss.

The low frequency (200-800 MHz) version of this feed offers 4:1 bandwidth with input matching better than -10 dB and gives $\eta_{ap} > -2.7$ dB for $\theta_o = 63°$ of the prime focus reflector [62]. The manufactured prototype is shown in Fig. 3.5a. The high frequency version of this feed for cryogenic operation (Temp~ 20 K) in 2-13 GHz band is designed and characterized as a part of this thesis work and the details of it are given in **Paper F** and the manufactured prototype is shown in Fig. 3.5b.
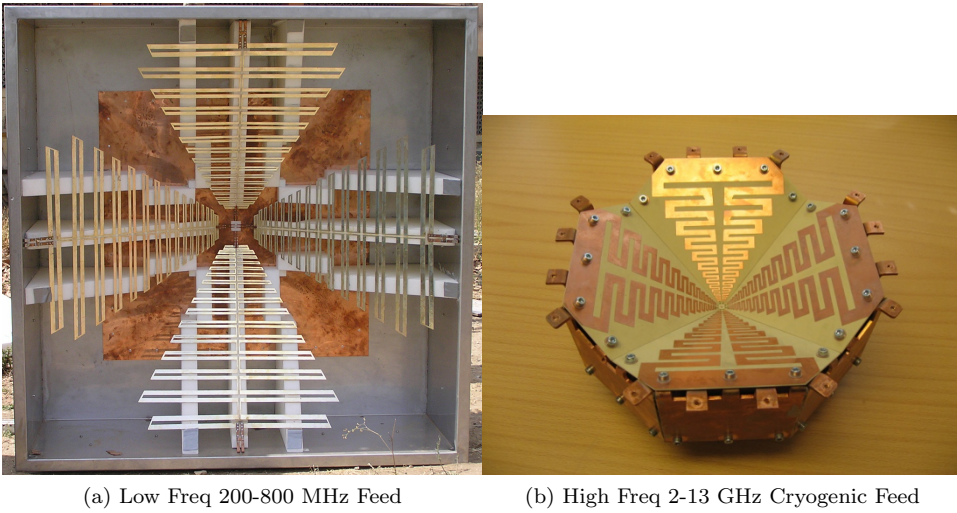
(a) Low Freq 200-800 MHz Feed   (b) High Freq 2-13 GHz Cryogenic Feed

Figure 3.5: Fabricated Prototypes of Eleven Feed
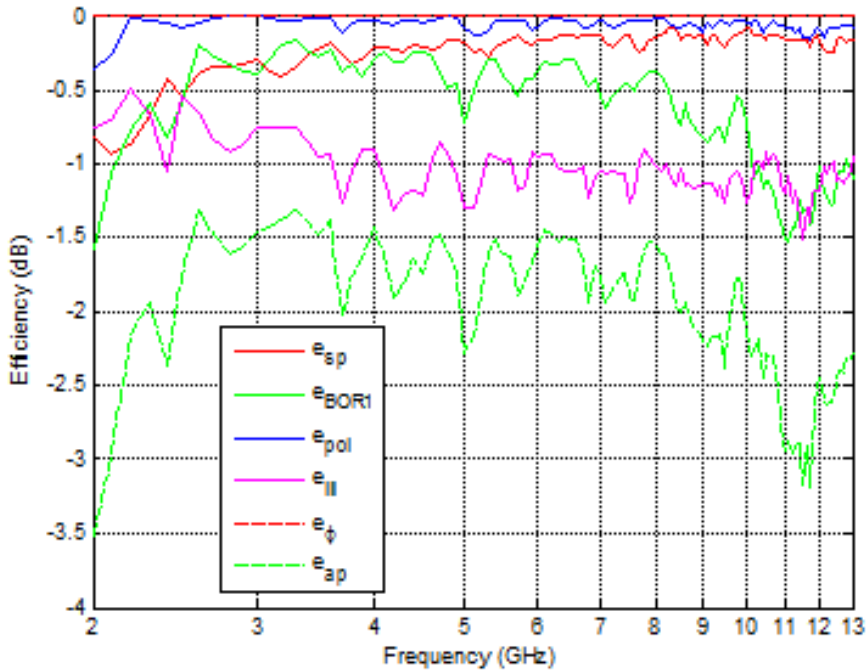
Figure 3.6: η_{ap} of 2-13 GHz Eleven Feed for Prime Focus Reflector ($^{f}/_{D} = 0.433$)

The aperture efficiencies obtained from 2-13 GHz model of Eleven feed are better than -2.5 dB for a prime focus reflector having $^{f}/_{D} = 0.433$ as shown in Fig. 3.6. Also the measured ohmic efficiency better than -0.4 dB is achieved [63].

This improved performance is a result of careful modeling of log-periodic arrays[3]

---

[3]using CST MWS: www.cst.com

20

along with the central excitation region which transfer signals from the log-periodic array to the back side of the ground plane for further integration with low noise amplifiers (LNA). Both single ended and differential LNAs [64] can be integrated with Eleven Feed to obtain dual polarization output [65, 66]. Thus Eleven Feed can offer broadband performance for reflector antennas having $\theta_o = 50 - 55°$.

3.5 Gaussian Coupling Efficiency

In contrast to the reflector antenna system, where goal is to maximize η_{ap}, the Quasi-optical systems require very high coupling of radiated power by antenna to the fundamental Gaussian Beam Mode. The Gaussian beam is a solution to the paraxial form of the Helmholtz equation and it is a convenient tool to model the optical system at THz frequencies. The fundamental mode of Gaussian beam has electric field Gaussian distributed and has no side lobes. Therefore for a radiating feed element, the efficient coupling of its power to the Gaussian distributed E-field is desired and it is quantified using the term Gaussian Coupling Efficiency (η_G) or Gaussicity [67].

In Quasi-optical systems, the use of Gaussian Beam approximation for modeling simplifies the overall analysis or synthesis of it. Such systems are often designed by assuming the input E-field having Gaussian distribution. And with the knowledge of input beam size (ω) where field is $-8.7dB$ down, the E-field in the entire system can be traced. At certain location the beam radius achieves its lowest value and it is referred as beam waist (ω_o). The exact definition of this Gaussian E-field in cylindrical coordinate system is defined in (3.10) [67]. Also the same E-field at the far-field distance from origin can be defined using (3.11) [68]. The more detail derivation of Gaussian beam far-field is given in *Appendix B*

$$E(\rho, z) = \sqrt{\frac{2}{\pi}} \frac{1}{\omega} e^{\left(\frac{-\rho^2}{\omega^2} - jkz - \frac{jk\rho^2}{2R} + j\Phi_o \right)} \tag{3.10}$$

$$E(R, \theta) = \frac{1}{R} e^{-jkR} \sqrt{\frac{2}{\pi}} \frac{\pi\omega_o}{\lambda} \cos\theta e^{-\left(\frac{\pi\omega_o}{\lambda} \right)^2 \sin^2\theta + j\frac{\pi}{2}} \tag{3.11}$$

The Quasi-optical systems can be viewed as low loss transmission lines in THz bands where all optical components have diameter/size $4\omega_o$ of fundamental Gaussian Mode which contains 99% of transmitted power. Hence the efficient coupling of radiated power to fundamental Gaussian beam mode is necessary.

This type of coupling can be computed either from the near-field or from the far-field of the antenna. The exact definition of η_G using near-field as well as far-field is defined in (3.12),(3.13) [69, 70, 67]. The Gaussian coupling efficiency by its definition suggests the coupling of radiated powers between an antenna and the Gaussian beam. Therefore, this coupling will be maximum (100%) when the near-field of an antenna is complex conjugate of Gaussian beam E-field.

$$\eta_G = \frac{\left| \int \int E_A \cdot E_{Gauss}^* \ dx \ dy \right|^2}{\left[\int \int |E_A|^2 \ dx \ dy \right] \left[\int \int |E_{Gauss}|^2 \ dx \ dy \right]} \tag{3.12}$$

$$\eta_G = \frac{\left| \int\int G^A \cdot G^G \sin\theta d\theta d\phi \right|^2}{\left[\int\int |G^A|^2 \sin\theta d\theta d\phi \right] \cdot \left[\int\int |G^G|^2 \sin\theta d\theta d\phi \right]} \tag{3.13}$$

$$\eta_G = \eta_{BOR_1} \cdot \eta_{spill} \cdot \eta_{pol} \cdot \eta_{BOR_1}^{Gauss} \tag{3.14}$$

Even though, the Gaussicity can be computed from the knowledge of the 2-D near-field data of an antenna; the problem with near-field 2-D cut is that the truncation of

the 2-D plane affects the accuracy of the computations. While with antenna far-field which is defined over complete sphere, the issue of truncation is eliminated. Hence, in this thesis the computations of η_G are derived only from far-field description of antenna radiation pattern.

The **Paper C** of this thesis describes a method to calculate the η_G using far-field data defined over complete sphere (i.e. $0 \leqslant \theta \leqslant \pi$ & $0 \leqslant \phi \leqslant 2\pi$). Even though the direct computations of η_G using (3.13) are possible, to develop better understanding the **Paper C** mathematically factorizes η_G into four sub-efficiencies as given in (3.14).

The conclusions from **Paper C** suggests that for an antenna to have high η_G, its pattern should be of the type BOR_1 with equal E- and H-planes and minimized side lobe levels [56]. Also the BOR_1 components of antenna far-field pattern mainly influence the coupling efficiency to Gaussian beam. This understanding developed in **Paper C** along with the algorithm of η_G computation is used further in the thesis to characterize planar antennas for their Gaussian coupling efficiencies. Finally, if the intended use of an antenna is in Quasi-optical systems then the total efficiency takes the form as given in 3.15.

$$\eta_{total} = \eta_{ohmic} \cdot \eta_{refl} \cdot \eta_G \qquad (3.15)$$

3.6 Examples of η_G for Horn Antennas

With the implementation[4] of generic algorithm for the computations of the η_G from the 3-D far-field data of antenna based on **Paper C**; it is possible to use this algorithm to quantify η_G for well-studied aperture based Horn Antennas. The purpose of doing this is to understand the practical limits on the η_G values and later on in the next chapter compare it with η_G values of planar antennas.

3.6.1 Corrugated Horn

These type of horn antennas offer far-field very close to the ideal Gaussian beam and are widely used for both reflector antenna systems and THz quasi-optical systems. These antennas are studied in-depth for their far-field and its coupling to the Gaussian Beam. The theoretical max. coupling from corrugated horn to fundamental gaussian beam mode is 97.92% [71, 72].

Also the corrugated horn antennas are well characterized in terms of the beam waist (ω_o) and its location (z_o) inside the throat of the horn for the Gaussian beam associated with it [73, 67]. To elaborate this further a corrugated horn operating in W-band (75-110 GHz), with length $L = 30$ mm and having semi-opening angle $\alpha = 7.5°$ is shown in Fig. 3.7a along with the gaussian beam originated from it. The 3-D far-field is shown in Fig. 3.7b.

Now to estimate the optimum beam associated with the far-field of this horn, the algorithm discussed in **Paper C** is used. The algorithm convergence occurs in less than 7 iterations and it is shown in Fig. 3.8a as solid black line. The analytical values of ω_o and z_o are shown with dotted lines. With the same data, the direct evaluation of η_G using (3.13) is shown in the same figure as well for various values of ω_o and z_o. Thus the contours are independently computed in Fig. 3.8a. The converged value of max η_G is 97.5% which is in well agreement with theoretical maximum. (*Note: The numerically tested accuracy of this algorithm is* 0.5%)

---

[4]using MATLAB: `www.mathworks.com`

(a) 2-D Profile with Gaussian Beam　　　(b) 3-D Patterns
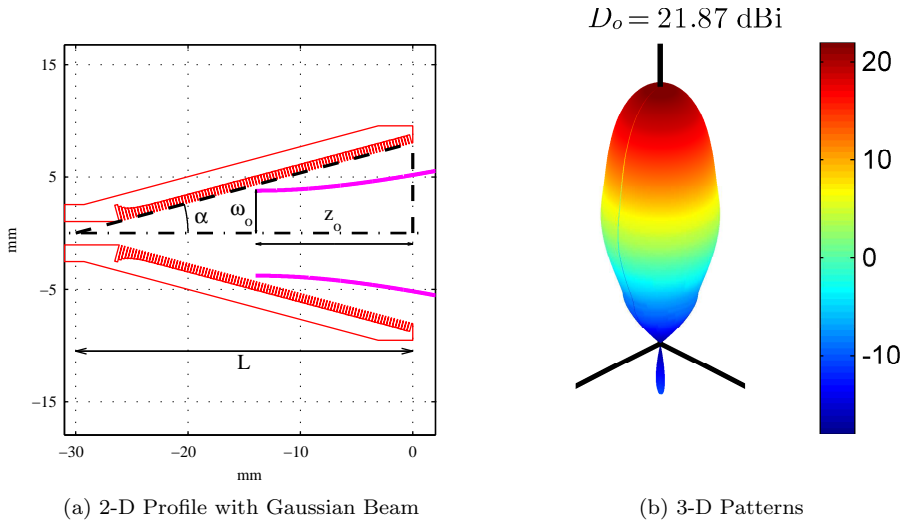
Figure 3.7: Corrugated Horn $L = 30\ mm$ & $\alpha = 15°$ @ $F = 100\ GHz$

(a) Algorithm Convergence (solid line) Vs Analytical Values (dashed line)
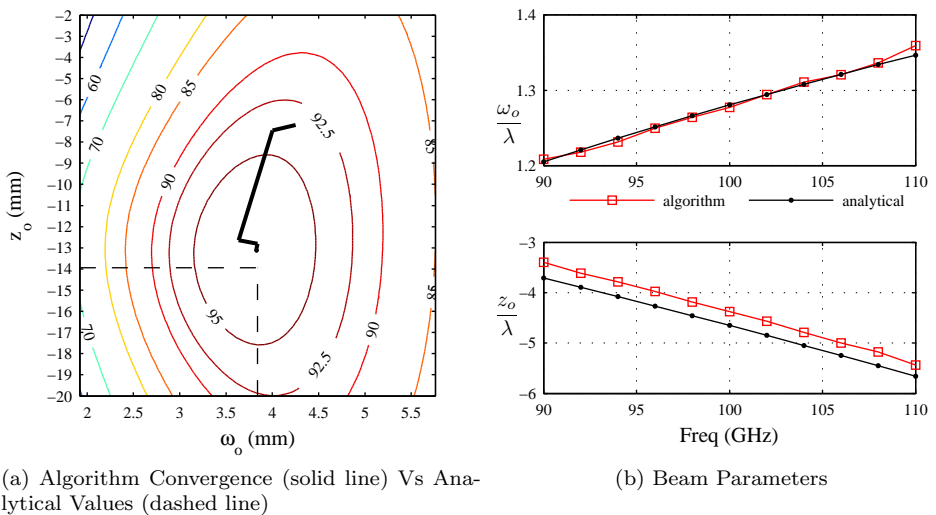
(b) Beam Parameters

Figure 3.8: Comparison of analytical beam parameters with numerically computed values using far-field

This numerical study shows the effectiveness of algorithm developed in **Paper C**. To further strengthen this claim, the numerically computed ω_o and z_o values for this horn are compared with analytical values in Fig. 3.8b over 20% bandwidth. These values agree well proving the robustness of the algorithm on estimation of Gaussian beam coupling and beam parameters.

Thus the corrugated horns offers the best coupling to Gaussian beam with efficiency $\sim 98\%$. But these type of horns require very precision machining with high accuracy for them to be used in THz band.

3.6.2 Dual-Mode Potter Horn

To overcome the need of precision machining of corrugated horns, dual mode horns can be used since they don't require corrugation on the walls but can offer similar performance by carefully exciting higher order modes of circular waveguide. Thus these horns usually have a step discontinuity in the throat region for creation of higher order modes.

(a) 2-D Profile of Potter Horn (b) Computed η_G values of Potter Horn
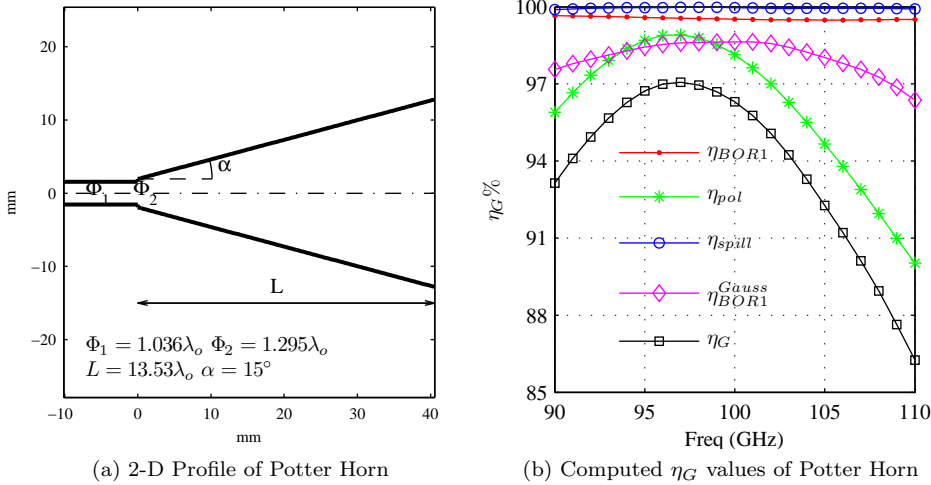
Figure 3.9: Gaussian Coupling of Dual-Mode Horn

The 2-D profile of this type of horn is shown in Fig. 3.9a [74] and corresponding η_G values are shown in Fig. 3.9b in the W-band. It is conclusive from these computations that the frequency at which exact phasing condition occurs at the aperture of horn, the η_G is maximum and its value is comparable to that of corrugated horns. But away from these frequency modes can not cancel each other perfectly causing increased cross-polarization which results in degraded polarization efficiency and in turn Gaussian coupling efficiency.

3.6.3 Choke Horn

This is a flare angle controlled horn whose radiation patterns are constant over 1.8:1 bandwidth [57]. This horn is scaled up in frequencies of W-band and again η_G computations are performed from the simulated far-field pattern. The geometry of horn with 3-D radiation pattern is shown in Fig. 3.10a and corresponding η_G values in Fig. 3.10b. This relatively simple horn geometry produce radiation patterns with very high coupling ($\sim 98\%$) to fundamental gaussian beam mode.

3.6.4 Smooth Conical Horn

This is the simplest type of horn obtained by flaring out circular waveguide with linear taper. One such smooth conical horn having opening angle $\alpha = 30°$ and aperture diameter of 8.33 mm in G-band (140-220 GHz) is studied here.

The radiation pattern of this horn along with it structure is shown in Fig. 3.11a and corresponding η_G values in Fig. 3.11b As discussed in section 7.6.3 of [67], the

(a) 3-D Patterns of Choke Horn

(b) Computed η_G values of Choke Horn
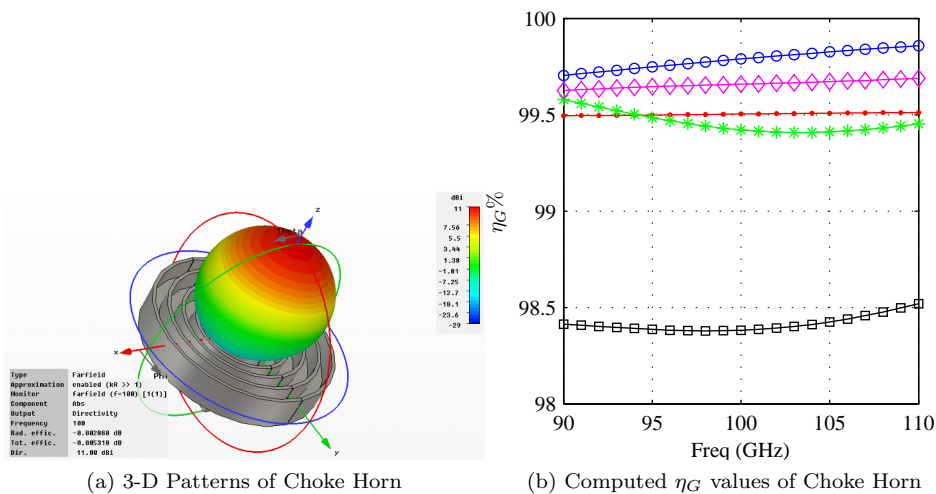
Figure 3.10: Gaussian Coupling of Choke Horn

(a) 3-D Patterns of Conical Horn

(b) Computed η_G values of Conical Horn
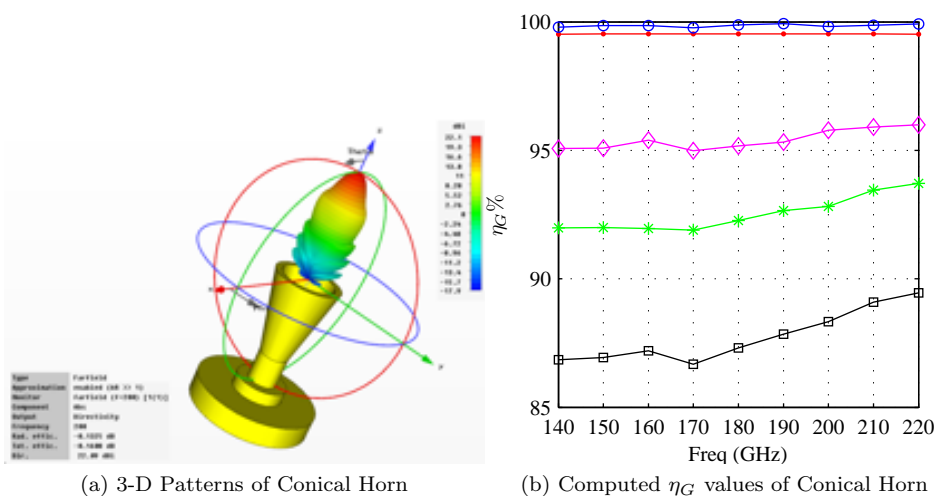
Figure 3.11: Gaussian Coupling of Conical Horn

η_G of this type of horn is $\sim 87\%$. This is also confirmed by computed η_G from the far-field. The reason behind lower η_G as compared to other horns is mainly because of increased cross-polar levels. This has resulted in lower η_{pol} as seen from Fig. 3.11b.

With this study it can be concluded that rotationally symmetric horn structures can achieve very high $\eta_G > 85\%$. But these type of 3-D structures become difficult to integrate with planar MMICs in THz bands. And therefore development of planar antennas with the goal of maximizing η_G is required for improved THz Quasi-optical systems.

3.7 Trade Off between η_{ap} and η_G

The aperture efficiency is maximum when the E-field over the aperture is uniform in amplitude and phase while on the contrary the Gaussian Coupling efficiency is maximum when the E-field over the aperture is Gaussian distributed. This directly translates to the tradeoff that for a given aperture size both η_{ap} and η_G can not attain maximum value. Also the η_G of 100% occurs when the Gaussian aperture distribution is not truncated. i.e. with infinite extent aperture. This type of aperture is in practice not possible.

To elaborate this paradox, the circular aperture size of 5λ is considered here. The E-field over this aperture is set to Gaussian but it is truncated at certain taper at the edge of it. The 3-D radiation patterns of such truncated aperture distribution can be computed using [75, 50].

The taper at the edge of the aperture is varied from -4 to -16 dB and corresponding far-field patterns are computed. From these far-field patterns, using algorithm developed in **Paper C**, η_G is computed. Also to compute aperture efficiency the difference between on-axis directivity (D_o) of these patterns to the D_{max} is used, as shown in (3.16).

$$\eta_{ap} = 10 \log_{10} \left[4\pi \frac{\pi (D/2)^2}{\lambda^2} \right] - 10 \log_{10} Do \tag{3.16}$$

Fig. 3.12a shows the 3-D radiation patterns of truncated Gaussian distribution when the taper at the edge is -8.7 dB. Thus the aperture is truncated at the exact size of beam waist (ω_o). The effect of this truncation is clearly visible with the presence of side-lobes. Here it is worth mentioning that the ideal Gaussian distribution has no side-lobes. These increased side lobe levels cause higher spill-over loss and less coupling of power to the ideal Gaussian beam and hence effectively η_G is lowered.

To further understand this effect, Fig. 3.12b shows the numerically computed η_{ap} & η_G values for various taper values. The higher η_{ap} is seen at lower taper values while on the contrary higher taper values resulted in higher η_G.
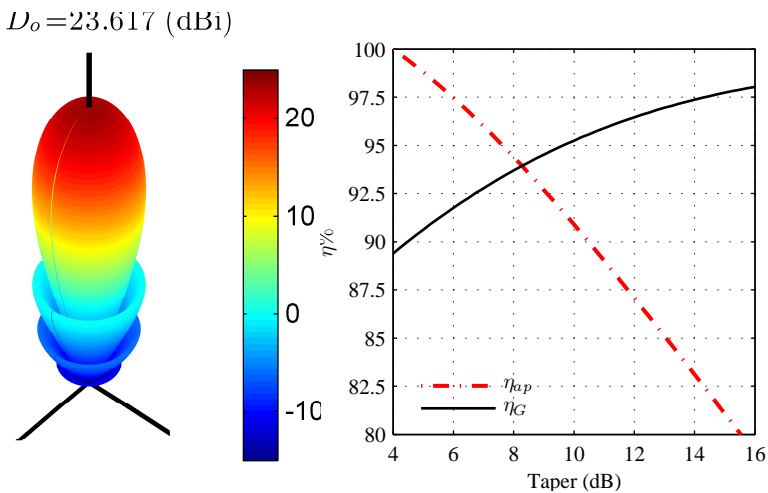
(a) Far-field of Truncated Gaussian Distribution (b) η_{ap} & η_G of Truncated Gaussian Distribution ($D = 5\lambda$ and Taper=-8.7dB)

Figure 3.12: Trade Off for η_{ap} & η_G

The understanding developed in this section is very useful while designing MMIC based planar antennas. In MMIC based designs often the area available for the design is very limited or it is expensive to reserve large areas for passive antenna structures. Then this type of simpler analysis helps the designer to get rough estimates on the required area when certain design goals are specified in terms required beam waist or antenna directivity.

In upcoming chapter, the definitions described here will be used to evaluate performance of different planar antenna designs made in MMIC processes described in Chapter 2.

CHAPTER 4

Antenna Topologies

There exists numerous attractive designs and topologies for millimeter and sub-millimeter wave antennas, but considering integration with active circuits, if the antenna can also be a part of a MMIC, then the resulting receiver would be more compact and can have added functionality. Hence, it is important to come up with antenna solutions which are completely compatible to the particular MMIC layer structure. Thus with given MMIC process entire antenna integrated receiver can be fabricated.

For this purpose, this chapter first introduces a brief classification of the radiating antenna structures based on their operating principles followed by the discussion on selection criterions for antenna elements considering compatibility of antenna structures to the particular MMIC process. Later on, based on the chosen antenna elements, their realization using available MMIC processes is shown in detail. The chapter concludes with the comparison of described antenna topologies in terms of antenna efficiencies and their relevance to the THz imaging applications.

4.1 Antenna Classification

Since the first demonstration of dipole structure by Heinrich Hertz as a radiator of electromagnetic waves in 1886, antenna engineers have found variety of ways, geometries/structures which transforms applied electric current excitation in to the free space radiated electromagnetic waves [49]. The extensive literature on these different antenna structures can be found in [48, 76, 77, 78, 79].

Based on the literature survey, the radiating antenna structures are classified in four different ways in this thesis and are described in Fig. 4.1. The first and simplest type of antenna elements are dipoles, slots, circular or square loops which are based on single resonance and offer input impedance match over narrow bandwidths. These structures are usually fed by TEM or Quasi-TEM lines. The second type of structures can be made by combing single resonances structure by cascading them with addition of appropriate phase shift for one element to the next. This type of approach helps in achieving very wide bandwidths and is often used in designing log-periodic antennas. The third type is based on gradually tapering out slot lines such that they start radiating. This type of tapering of slot lines is very common in Vivaldi type of antennas. The last type is based on radiating structures obtained from waveguides having TE or TM modes. So all types of horn antennas fall under this category along with slots excited by waveguides.

The reflector or lens antennas are not included here since they can be viewed more as focusing components and not as actual radiating structures. Similarly, antenna arrays are omitted since they are based on combination of these basic antenna elements with appropriate amplitude and phase. This type of classification helps in gathering a larger picture at a glance and further facilitates the selection of antenna topologies compatible with MMIC processing techniques.

Antenna Families

Single Resonance

- Dipoles[1]
- Folded Dipoles
- Monopoles
- Yagi-Uda
- Slots[2]
- Folded Slots
- Microstrip Patches
- Loops
- Dielectric Resonators
- Helix

Narrow Bandwidth

Cascaded Resonances

- Log-Periodic Arrays of Dipoles
- Log-Periodic Arrays of Folded Dipoles
- Log-Periodic Arrays of CPW fed Slots
- Bend Zig-Zag antenna

Wide Bandwidth

Gradual Tapering

- Bow-Tie Dipole
- Biconical Slots
- Linearly Tapered Slots
- Vivaldi
- Antipodal Vivaldi
- Self-complementary structures
- Disc cone antenna
- Log-periodic Spirals

Wide Bandwidth

Radiating Apertures

Rectangular Waveguide
- Rectangular Horns
- Pyramidal Horns
- Diagonal Horns
- Slot Arrays in Waveguide Walls

Ridge Waveguide
- Quadridge Horns

Circular Waveguide
- Smooth Conical Horns
- Corrugated Horns
- Dual Mode Horns
- Hard Horns

Moderate Bandwidth

[1]: Planar, Broad Side Radiation, Linearly Polarized
[2]: Planar, Broad Side Radiation, Linearly Polarized, Microstrip Feed, Feasible with MMIC Process

Figure 4.1: Classification of Different Antenna Structures

4.2   Antenna Element Selection Criterions

Based on this classification selection process can be performed. The foremost selection criteria in this process is that the radiating antenna element can be realized using planar metal layers of MMIC. Considering, the target application of this thesis, which is imaging, only linearly polarized antenna elements are selected. The chosen antenna elements should have a feed from Quasi-TEM lines such as microstrips or CPW. Since these lines are preferred interconnect lines on MMIC and finally the antenna elements should have radiation maximum in the broadside direction. i.e. perpendicular to the plane containing MMIC.

Apart from these required properties, considering their intended use in Quasi-optical systems; the selected antenna elements should assist in achieving high Gaussian coupling efficiencies with low ohmic losses along with -10 dB input matching over $\sim 10\%$ bandwidth. Even though the basic antenna elements can not directly achieve high Gaussicity from their radiation patterns, these elements can be combined in arrays to obtain required radiation pattern. These techniques are described in the later half of this chapter. Based on this discussion, these selection criterion can be summarized below.

- Planarization of Geometry

- Linearly Polarized

- Broad side radiation

- Microstrip Feeding

- Compatible to MMIC Processes

- Low ohmic losses

- High coupling of radiated power to Gaussian beam

- -10 dB bandwidth $\sim 10\%$

These selection criterions assist considerably to choose the appropriate radiating structures from Fig. 4.1. Dipoles, Folded Dipoles, Bow-Tie type of dipoles can be made planar and are feasible to fabricate in a single metal layer. But still these are excluded from selection because of two important reasons. 1. The MMIC processes described in Chapter 2 are based on thin dielectric layers. Hence, the dipole formed on top metal layer stays very close to the ground plane causing its input impedance to be very low(typically few ohms) and 2. dipole type of structures require balanced feeding which would require a BALUN on every element. Also many other attractive elements such as Vivaldi, Linearly Tapered Slots are eliminated due to their radiation being in end-fire direction. i.e. in the same plane of the planar antenna structure.

This narrows down to microstrip fed patch and slot antennas being most suitable candidates. Since microstrip patches can be made in single metal layer, they are feasible to fabricate in both MMIC processes described in Chapter 2. Slots are feasible in a MMIC process which offers patterning of ground plane and a top metal layer to make a microstrip line to feed them.

So far the radiation patterns of these suitable elements are not considered in the selection process. The basic radiation patterns of half wavelength dipole in free space, slot in an infinite ground plane and microstrip patch on infinite ground plane is shown in Fig. 4.2. As seen from the radiation patterns, none of them would couple radiated

energy efficiently to the fundamental mode of Gaussian beam. Hence, modifications in the pattern is needed to obtain more rotationally symmetric beam having higher directivity and smaller beam width.

(a) $\lambda/2$ dipole in free space (b) $\lambda/2$ slot in infinite ground plane (c) Microstrip Patch on infinite ground plane
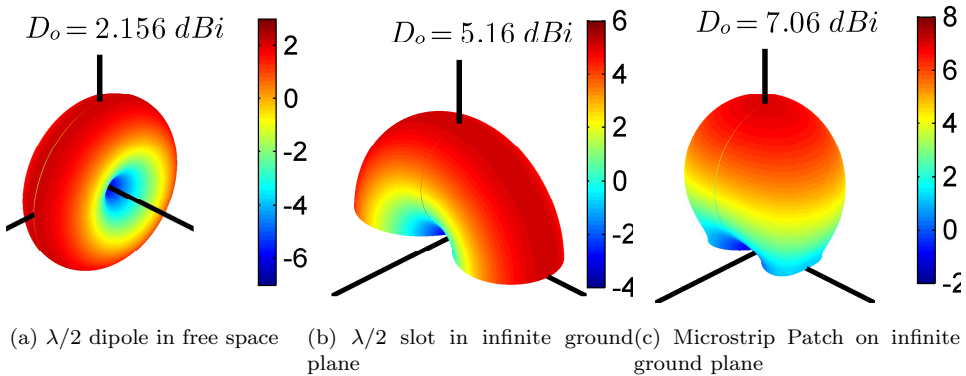
Figure 4.2: Radiation Patterns of Basic Antenna Elements

Finally based on the above discussion it can be concluded that the microstrip fed patch and slots are more attractive choice considering fabrication, input impedance, planarity and simplicity in feeding. But the inherent radiation pattern of single element is not suitable for high η_G. Hence, smaller arrays of these basic elements can be made to shape the beam. Also based on the maximum of beam direction, a further classification can be made for antenna topologies based on arrays of patches and slots. The first type being antenna topologies with microstrip patches having most of its radiated energy in broadside direction (i.e. at $\theta = 0°$ in spherical coordinate system) and the second being with slots having radiation maximum below the plane of the chip (i.e. at $\theta = 180°$). Therefore in this thesis these topologies are referred as 1. Broadside radiating and 2. Inverse Broadside radiating.

4.3 Substrate Definitions

The primarily used MMIC processes used in this thesis are described in Chapter 2. However in antenna perspective, it is more relevant to extract important information about dielectric layers and their electric properties for antenna design. Both processes, TSC HEMT and TSC DHBT can be generalized in terms of a more generic microwave substrate which can be used for antenna simulations.

The first process based in TSC DHBT has four metal layers and three dielectric layers made of 'benzocyclobutene' (BCB) having dielectric constant $\epsilon_r \sim 2.7$ [80]. The largest thickness with these layers is 5 μm with Gold (Au) top metal of 3 μm thick. This results in a substrate shown in Fig. 4.3a and it is referred as Process Definition I in this chapter.

The second process of TSC HEMT is on 50μm thick semiconductor substrates with 3.3 μm thick top metal and 5 μm thick ground metallization layer as shown in Fig. 4.3b. This is referred as Process Definition II. These substrates definitions will be used further in the chapter for antenna computations and performance comparisons.

The important aspect to look at for these substrates is the cut-off frequencies for substrate modes. Since any antenna structure designed at frequencies higher than the cut-off frequency might cause excitation of unwanted substrate modes and would

(a) Process Def. I

(b) Process Def. II
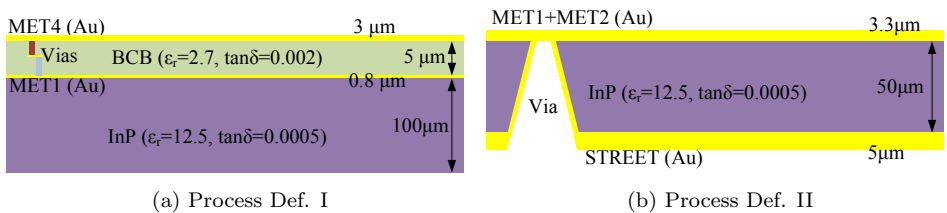
Figure 4.3: Substrate Definitions

degrade the radiation pattern and efficiencies of the structure. The lower most cut-off frequency for both TE and TM modes for a ground dielectric slab is given by (4.1) using [81]. From this formula, the cutoff frequencies for 100 μm and 50 μm InP substrates are 221 GHz and 442 GHz respectively. For BCB layer of 5 μm it is 11.49 THz due to ultra thin nature and low dielectric constant.

$$f_c = \frac{C_o}{4h\sqrt{\epsilon_r - 1}} \tag{4.1}$$

4.4 BroadSide Radiating Antenna Geometries

The microstrip patch based designs are primarily fall under this category. The topologies using microstrip patches can be realized using both process definitions but the choice of the process is more a trade-off between ohmic loss and impedance bandwidths obtained from the patches. Since it is empirically understood that the broadband microstrip patch can be realized using low dielectric constant and thick substrate [82]; both MMIC process definitions do not offer optimum choice. Since in Process Def. I, the low dielectric constant BCB is a preferred choice, the microstrip patches realized on it would suffer due to poor ohmic efficiency while patches made on Process Def. II would be narrow band due to high dielectric constant of InP.

Therefore in this thesis all microstrip patch based designed are done using Process Def. I while slots based Inverse broadside designs are made using Process Def. II. For each design describe henceforth, it is characterized in terms of ohmic, reflection and Gaussian Coupling efficiency considering their intended use in Quasi-optical systems. For each topology presented, the simulated results are summarized at the end of the chapter for comparison.

4.4.1 Microstrip Patch Array 2x1

As seen from Fig. 4.2c, the H-plane of a patch has null along the ground plane while the E-plane does not vanish along the ground giving unequal E- and H-planes which would reduce the coupling to Gaussian beam. Hence, a combination of two patches separated by a distance $\sim \lambda/2$ in E-plane helps in narrowing beam width in E-plane. The two patches can be combined in phase by making use of Microstrip Tee based feed network with appropriate impedance matching quarter wavelength transformer. The traditional topology with this type of corporate feed network is shown in Fig. 4.4a.

The main disadvantage in using in phase feeding of the patches is that the microstrip feed network occupies more space on MMIC and at the same time at high frequencies such as 340 GHz, the feed lines causes spurious emission which results in loss as well as un-symmetries in the radiation pattern. The cross-polar levels increase

and the overall coupling to fundamental Gaussian beam mode degrades. It is shown in **Paper C** that polarization efficiency is a sub-efficiency term in η_G computations and therefore any unwanted radiation by microstrip based feed network is a loss.

(a) Corporate Feed   (b) Differential Feed
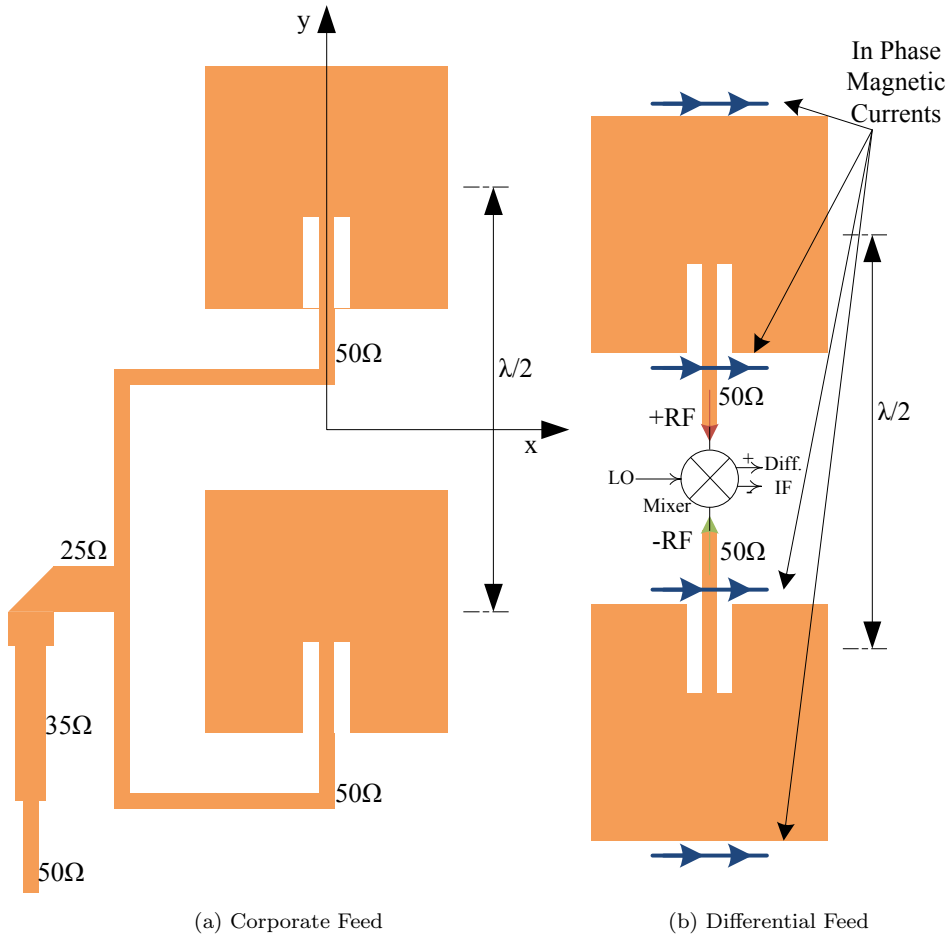
Figure 4.4: Feed Networks for 2 x 1 Patch Array

Also it will be explained in the next chapter on Mixers that many microwave mixers require balanced RF excitation and therefore traditionally microwave mixers are made with RF hybrid. But since in this work, the focus is on integration of antenna + mixer on a single MMIC, the overall combination of corporate feed network based antenna array with RF hybrid and mixer would occupy large space on a chip which in turn increases the cost associated with the circuit.

To overcome this limitation, this thesis focuses on those antenna topologies which can directly offer balanced RF output but still be able to retain broadside symmetric beam. This can be achieved simply by rotating one of the microstrip patch by 180° as shown in Fig. 4.4b. Thus the plane wave incident from broadside direction would results in the in-phase E-field in the radiating edges of the microstrip patches but out of phase current on the microstrip feed lines. Thus a unbalanced microstrip antenna array is deliberately made balanced or differential for compact integration with balanced mixers. This will be explained more in the discussion chapter on antenna integrated

receivers. To summarize, the advantages of making differential antenna topologies are listed below.

- Differential RF output in terms of two microstrip lines carrying out of phase signals

- Reduced complexities of microstrip based feed networks

- The spurious emission from feed lines cancels on axis giving null for cross-polarization

- Reduced cross-polarizations levels with respect to co-polar maximum

- Suitable to integrate with balanced mixers

- Requirement of RF hybrid from mixer side is eliminated

- Compact integration

- Ohmic Losses are reduced due to elimination of corporate feed network

Now the antenna described in Fig. 4.4 can be designed using Process Def. I with patch on MET4 and ground on MET1. To give a fair comparison between corporate feed and differential topology both antennas are simulated and from simulations η_{ohmic}, η_{refl} are computed. These are shown in Fig. 4.5a and their $\phi = 45°$ co- and cross-polar patterns are shown in Fig. 4.5b. Due to the requirement of extra microstrip lines for feed network, the ohmic losses in corporate feed based patch array are 3 dB worse than the differentially fed patch array. Also the spurious radiation from the feeder lines have caused high on-axis cross-polar levels and also reduction of on-axis directivity as compared with differential topology. Thus from simulation results, it is conclusive that the differential fed patch array show superior performance.

(a) Ohmic and Reflection Efficiencies   (b) $\phi = 45°\ Plane Patterns$
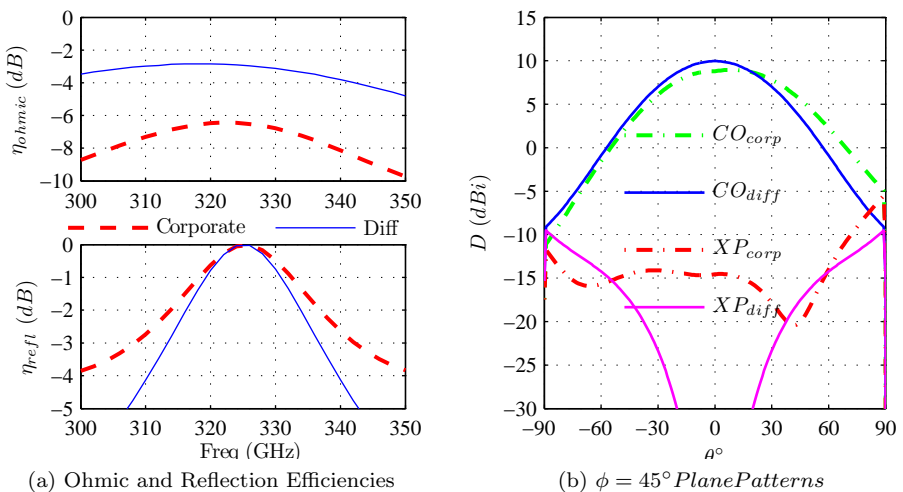
Figure 4.5: Comparison of Corporate and Differential Feed

Therefore, the improved differential topology can now be studied in terms of η_G for Quasi-optical systems. The computed Gaussicity and beam parameters from the

simulated far-fields of this 2x1 differentially fed patch array (Fig. 4.4b) are shown in Fig. 4.6.
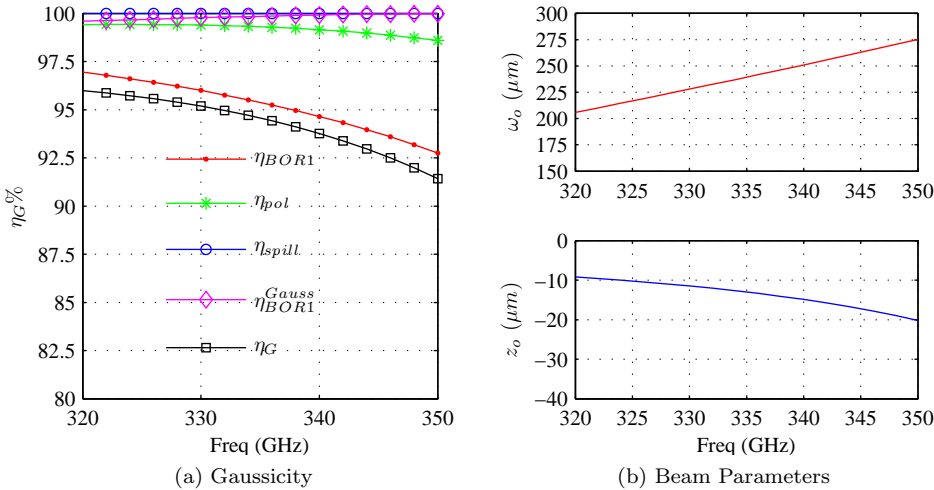
Figure 4.6: Gaussian Beam Analysis of 2x1 Patch Array

The main disadvantage which is seen from Gaussian beam analysis of 2x1 patch array is that the beam waist side is typically 0.25λ. Even though, the high $\eta_G > 90\%$ is obtained, the small beam waist would result in excessive size of primary / sub-reflector in Quasi-optical systems. Since small beam waist results in fast diverging beam, it causes difficulty in obtaining slow optics system with higher depth of focus for imaging applications.

As seen from Fig. 4.6b, the variation of beam waist location is very small over frequency and it is very close to the ground plane. This is an added advantage since it reduces de-focussing losses.

Here it is also important to note that the practical lower limit on the beam waist size is 0.2λ below which the Gaussian beam approximation completely fails [68]. The beam waist size $\omega_o > 0.9\lambda$ is considered as the limit above which Gaussian beams can be safely used to model Quasi-optical systems. Considering these aspects of Quasi-optical systems, the differentially fed 2x1 patch array is not an appropriate choice even though it offers high coupling and occupy less area on MMIC. Therefore, more elements need to be added in the array to make beam narrower which results in increased beam waist size. This is shown in next sub-sections with increased number of elements in arrays.

4.4.2 Microstrip Patch Array 2x2

This geometry is derived from 2x1 patch array by in phase addition of extra 2x1 patch array. Thus the total patch elements are four and pairs of two are fed in phase and finally a differential output is obtained as shown in Fig. 4.7a. The simulated η_{ohmic} and η_{refl} are shown in Fig. 4.7b.

The Gaussian beam analysis on this type of array offers improved coupling as well as increase beam waist size of the order of 0.5λ. The location of beam waist is very close to ground and can be considered as constant with respect to the wavelength.

(a) Geometry   (b) Ohmic Efficiencies
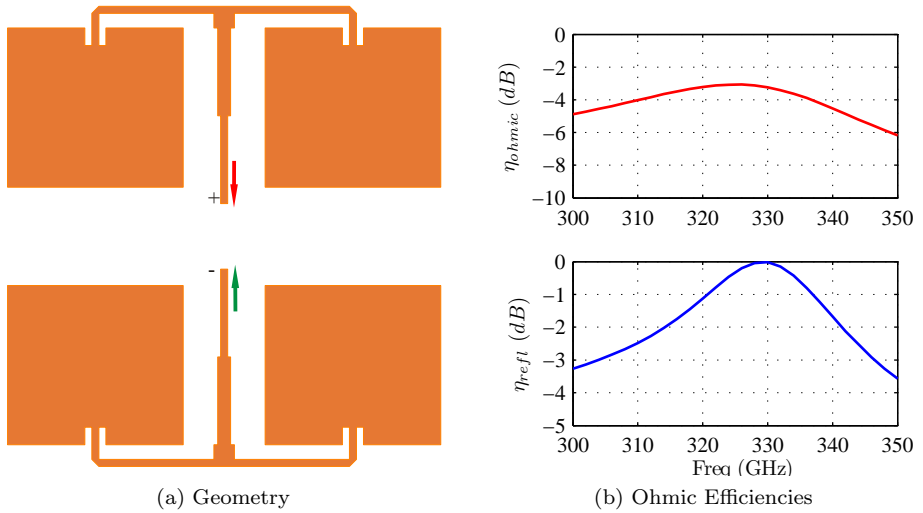
Figure 4.7: Differentially Fed 2 x 2 Microstrip Patch Array

This topology is attractive since it offers high coupling and occupy small area on MMIC, but still the beam waist is lower than practical limit of 0.9λ. The computed η_G and beam parameters from simulated far-field are shown in Fig. 4.8.

(a) Gaussicity   (b) Beam Parameters
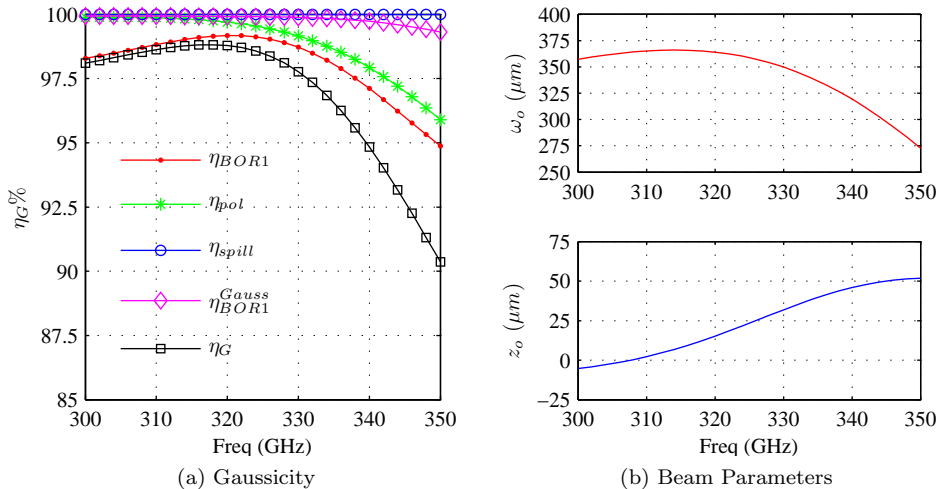
Figure 4.8: Gaussian Beam Analysis of 2x2 Patch Array

The implementation of this topology and its integration with the active differential mixer is successfully achieved using TSC DHBT process and is presented in **Paper A** of this thesis. This integration work is discussed more in the Chapter 7.

4.4.3 Microstrip Patch Array 4x4

To further increase the beam waist, the number of array elements can be doubled which would result in 4 x 4 patch array. Again the differential topology can be obtained by careful combination of elements and minimizing the required feed network as shown in Fig. 4.9a. Here, the core idea is to combine in phase two 2x4 sub-arrays of differentially fed patches. Thus the complete layout shown in Fig. 4.9a has four ports. Out of these ports, two ports on 2 x 4 sub-array form one differential port (marked with $+/-$ signs). The received RF signal over these differential ports can be first down converted to IF using a balanced mixer and then further two IF outputs can be combined to form a complete 4 x 4 patch array.

The advantages of this approach as well as its possible integration with active components is at present considered as future work direction and it is described in detail in Chapter 8. But considering scope of this chapter on antenna topologies comparison, this topology can also be evaluated in terms of η_{ohmic} and η_{refl} which are shown in Fig. 4.9b. The need of additional feed network has increased the ohmic loss to $\sim 6-8$ dBs over operation bandwidth of 10% around 340 GHz.

|(a) Geometry|(b) Ohmic Efficiencies|
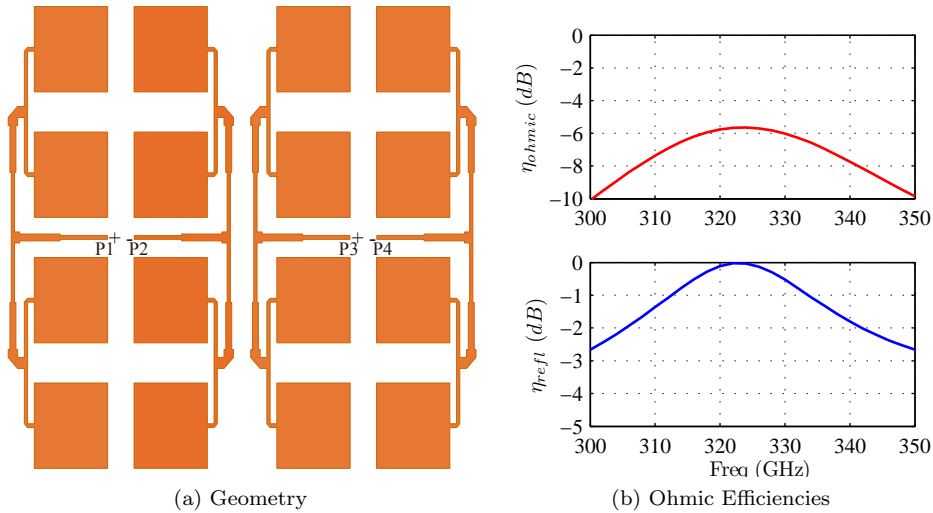
Figure 4.9: Differentially Fed 4 x 4 Microstrip Patch Array

The simulated patterns of these complete topology of 4x4 patch array offers narrow beam width but at the expense of increased side-lobe levels since all patches in the array are excited with uniform phase and amplitude. This approach gives increased directivity, narrow beam but reduced Gaussicity. At this point, it is important to re-focus on η_G and η_{ap} trade-off discussed in section 3.6 of this thesis.

In this case, the increased side-lobe levels due to uniform excitation of bigger array cause degradation of BOR_1 to Gaussian coupling sub-efficiency which in turn reduces η_G. Even though this trade-off exists, the over all antenna pattern achieves $\eta_G > 70\%$ over wide bandwidth and it is $> 75\%$ over narrow bandwidth of $\sim 7-8\%$ as shown in Fig. 4.10a.

The beam waist in this case is close to 1λ. The variation of beam waist location is high over 300-350 GHz but in the frequency band close to 340 GHz the beam location stays constants at a distance of $\sim 0.25\lambda$ below the ground plane. To summarize, even
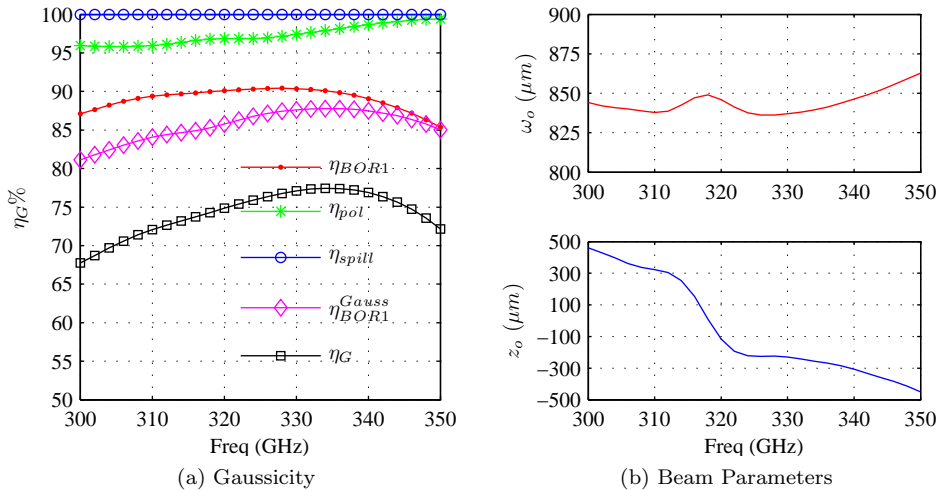
Figure 4.10: Gaussian Beam Analysis of 4x4 Patch Array

though this topology offers lower η_G it has potential to form a linear array of multi-pixel receivers. These aspects will be elaborated in detail in Chapter 8 discussing future work directions.

4.5   Inverse Broadside Radiating Antenna Geometries

These type of antennas radiate most of their power in the direction opposite to that of Broadside. i.e. below the MMIC. Hence, these structures are only possible for MMIC processes which have patternable ground layer or STREET layer to create radiating apertures. Therefore, the Process Def. II is more suitable process for these structures. But Process Def. I can also be used with ground openings in MET 1 layer.

It is common practice that the radiation caused by openings in the ground layer is focused using a lens attached to the substrate. The main purpose of doing this is to avoid substrate modes in thick-semiconductor substrates used for active device fabrication [83, 84]. Therefore, the choice of lens material and its shape are also important aspect on these type of antenna solutions. Hence first the design considerations for Silicon based lens are discussed and later on the actual feed structure, using two parallel slots etched in the ground plane, is described in detail.

4.5.1   Synthesized Silicon Lens

Radiating antenna structures having operating frequency higher than the cut-off frequency of substrate modes suffer from power loss due to coupling of radiated energy in the substrate modes. The common solution to overcome this problem is to integrate a dielectric lens having dielectric constant very close to substrate. Considering MMIC technology which uses high mobility, semi-insulating, semi-conductor substrates such as Silicon, GaAs, InP, InAs; the ϵ_r of these materials is in the range of 11-13. This results in Silicon ($\epsilon_r = 11.7$) as preferred choice of material for fabricating substrate integrated lens.

$\epsilon_r = 11.7 \ a = 4747 \ \mu m \ b = 4541 \ \mu m$
$L = 1725 \ \mu m \ \Phi = 10\lambda \ @ \ 340 \ GHz$

——— Ellipsoidal

— — — Synthesized

Anti-Reflection $\epsilon_r = 2.9, \ t = 135 \ \mu m$
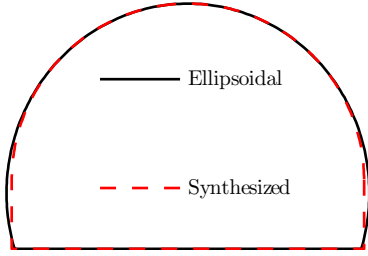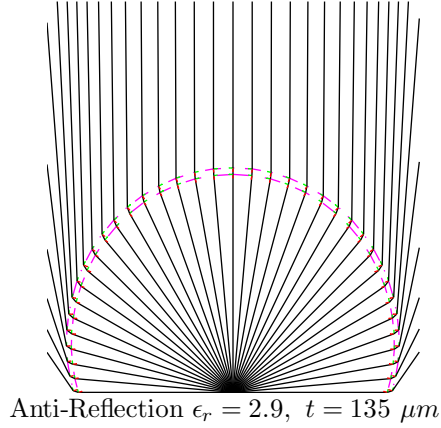
(a) Synthesized Lens   (b) GO Rays

Figure 4.11: Silicon based focusing Lens with Anti-reflection coat

The shape of the Lens is another importance aspect which influences the resultant radiation pattern from MMIC based feed structure + Integrated Lens. If the shape of the Lens is ellipsoidal with eccentricity equal to inverse of refractive index then the radiating feed structure placed at its focus would result in parallel propagating waves and a far-field pattern with diffraction limited main beam. One such example of this lens using Silicon as dielectric and having eccentricity of 0.29 ($e = 1/\sqrt{\epsilon_r}$) is shown in Fig. 4.11a. It has diameter of 8.8 mm.

This type of ellipsoidal lens can also be synthesized using a half hemi-sphere with cylindrical extension. The best fitted ellipse values for such lens are $a = 1.07691$ and $b = 1.03$ for major and minor axis respectively. The optimum extension length for peak directivity is computed using (4.2) [83]. The resultant shape from combination of half-hemisphere of diameter Φ and a cylinder with length L is shown also in Fig. 4.11a.

$$L = \left(a + \sqrt{a^2 - b^2} - 1 \right) \cdot \frac{\Phi}{2} \tag{4.2}$$

These type of lenses can be analyzed for far-field by Geometrical Optics ray tracing (GO) of radiated field from the feed in the interior parts of lens followed by Physical Optics (PO) integration of induced electric, magnetic current on the lens surface [85, 86, 87]. Here it would be important to note that such analysis would give less accurate results if the reflections of GO rays at the lens boundaries are ignored. Due to high contrast between the dielectric constants between Si and air, multiple internal reflections would occur of the transmitted ray from the feed structure. Also due to Brewster angle condition, some of rays would be totally internally reflected without transmission of any power in air. Therefore, these reflections must be take into account in GO-PO analysis of such lenses [88, 89].

One way to reduce these reflections is to introduce quarter wavelength matching layer on lens surface. The ideal dielectric constant for a single matching layer is 3.42 ($\sqrt{11.7}$). The thickness of this layer would be $\lambda_m/4$ where λ_m is the wavelength in the matching layer. But this thickness would make reflection coefficient zero for normal incident direction only. To minimize the reflection coefficient over wider incident

angles, the thickness can be altered using (4.3) [67].

$$t_m = \frac{\lambda_{air}/4}{\sqrt{\epsilon_m - \sin^2 \theta_i}} \quad (4.3)$$

Using this approach, the GO traced rays for lens of Fig. 4.11a with matching layer made of *Stycast 1264* having $\epsilon_r = 2.9$ are shown in Fig. 4.11b. The estimated matching layer thickness for incident angles up to $\theta_i \leq 30°$ comes out to be $t_m = 135\mu m$ @ 340 GHz using (4.3). It is seen that the rays originated from the feed placed at the focus of lens results in rays parallel to optical axis after refraction from lens and matching layer. This lens will now be used to perform more complete analysis of far-field pattern using realistic feed structure in the next subsection.

4.5.2 Double Slot Antenna with Si Lens

The use of two parallel resonant slots separated by distance $\sim \lambda_{si}/2$ forms a radiation pattern of feed structure with similar E- and H-planes [83]. This structure is very widely used for antenna integrated bolometers where the CPW fed slots couple radiation into the bolometer [26]. But for MMIC based active devices like HEMTs, the use of microstrip feeding is more common. Hence, the topology of CPW fed double slots can be modified by etching out the slot in the ground plane (STREET layer of Process Def. I) and feeding it with the microstrip line from the top metal.

With this approach, the slot radiates predominantly in the Si lens and partially in air. The excitation of such slot using microstrip line along with E-field in the slot is shown in Fig. 4.12a. The impedance of such microstrip fed slot has been studied and this discontinuity in the ground plane of the microstrip line can be modeled as the series impedance with the line [90, 91]. For a practical design, the other end of microstrip line can terminated in a radial stub giving inductive loading which results in good impedance match at the input of feeding microstrip line. Finally, the two slots can be combined further in phase using microstrip based corporate feed network as shown in Fig. 4.12b.

(a) Microstrip Feeding of Slot   (b) Corporate Feed of Double Slot
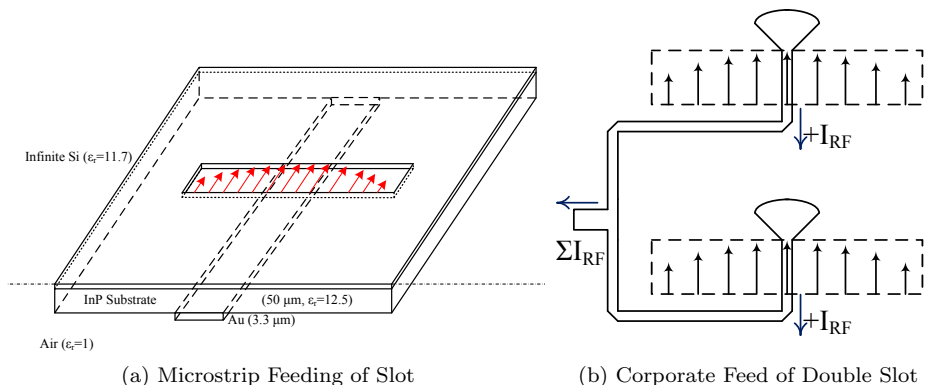
Figure 4.12: Double Slot Antenna Fed by Microstrips

This type of antenna structure is designed, fabricated and tested using GaAs-mHEMT MMIC process and is described in **Paper D** of this thesis. The double slot antenna as shown in Fig. 4.12 is integrated with balanced mixer on the said

(a) Differential Microstrip Feeding with Radial Stubs

(b) Via hole terminated slots
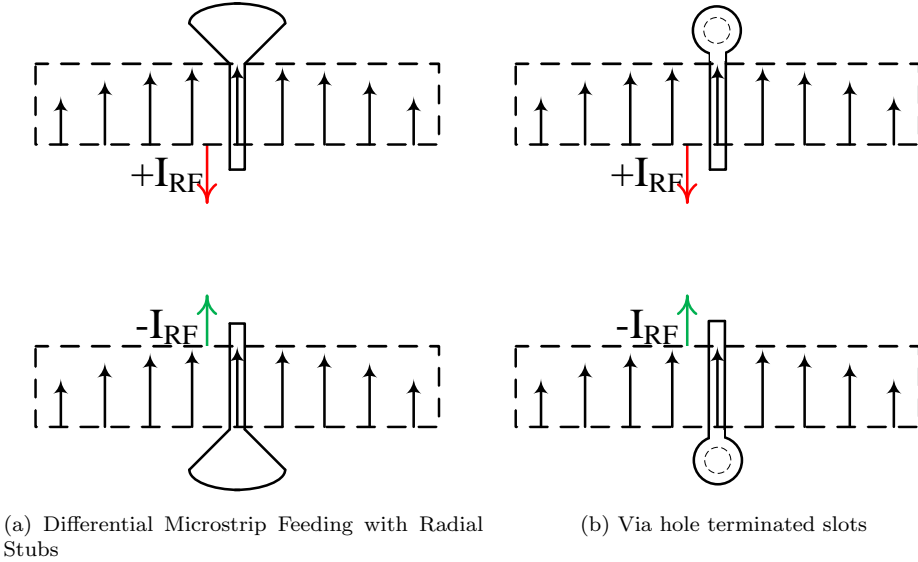
Figure 4.13: Differentially Fed Double Slot Antenna

process. Here, it is worth to mention again that due to the use of corporate feed the overall area occupied for MMIC was large since both microstrip feed network as well as RF hybrid are required in the integrated layout of the MMIC presented in **Paper D**. This shortcoming can be easily overcome by making the output of Double slot antenna differential as shown in Fig. 4.13.

Similar to the differentially fed 2x1 microstrip patch arrays, double slots can be made balanced by rotating one of the microstrip line feed by 180° as shown in Fig. 4.13a. The same topology can be made more compact by terminating the microstrip line with a Via hole available in MMIC process. Since a Via hole offering short circuit to the ground has certain finite inductance which in combination with a transmission line can act as a terminating load for the slots giving improved impedance matching [92].

The topology shown in Fig. 4.13 is fabricated in 50nm InP HEMT process along with integrated balanced mixer. It is discussed in brief in the Chapter 7 and details of the MMIC are given in **Paper B** of this thesis. The use of differential topology has resulted in very compact layout. To further investigate this topology at the desired frequency of 340 GHz, the radial stub matched differential double slot antenna is designed using Process Def. II, and it is integrated with synthesized hemi-spherical lens as discussed in subsection 4.5.1. Since here the goal is to maximize Gaussicity, the synthesized lens with smaller extension length of 0.147Φ is used.

Even though, the GO-PO based analysis for such a lens structure is feasible, its accuracy depends upon the number of internal reflections considered in the computations. Therefore, for more accurate analysis FDTD based CST MWS tool is used to model and simulate complete lens along with anti-reflection and the feed structure of double slots. For double slots, the separation of $0.6\lambda_{Si} \sim 0.176\lambda_{air}$ is used and for impedance matching microstrip fed slots with length of $\sim 0.55\lambda_{Si}$, terminated with radial stubs are used under differential condition as shown in Fig. 4.13a. For this

(a) Input Reflection for Microstrip Fed Slots

(b) η_{ohmic} and η_{refl}
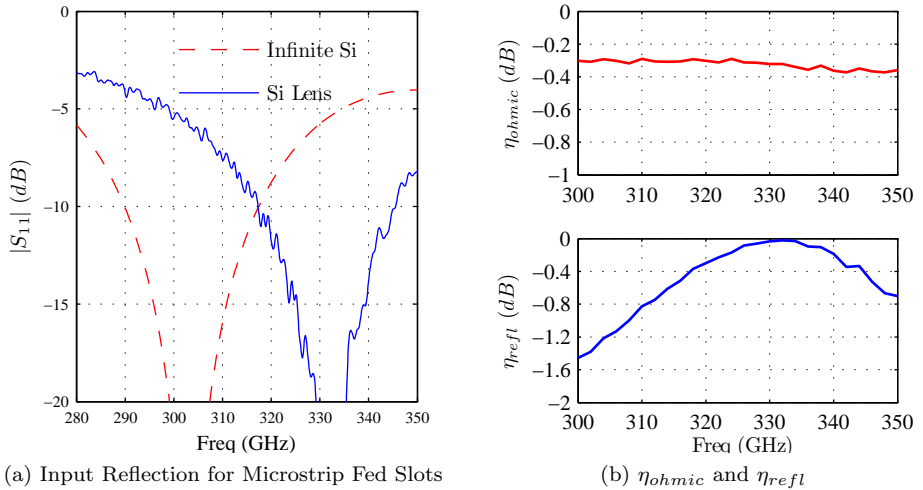
Figure 4.14: Impedance Matching and Efficiencies of Differential Double Slot Antenna

analysis the dielectric losses in Si and anti-reflection coat are neglected.

The input reflection of slots on a 75Ω microstrip line is shown in Fig. 4.14a when slots radiate in semi-infinite spaces of Silicon and air. For the same feed structure the input reflection when it is simulated with Si Lens is also shown in the same figure. Here it is worth to note that due to multiple reflections inside the lens and non-ideal anti-reflection coat, the input reflection shows ripples as well as upward shift of a few percents. But still the $-10\ dB$ impedance matching bandwidth of $\sim 8\%$ is achieved. The simulated η_{ohmic} and η_{refl} are plotted in Fig 4.14b. For ohmic efficiency computations the dielectric loss in homogeneous Silicon is neglected. Therefore η_{ohmic} mainly originates due to the losses in the feed structure.

The 3-D radiation pattern after the Lens is shown in Fig. 4.15a for frequency of 340 GHz. For the same frequency, the $\phi = 45°$ plane patterns are shown in Fig. 4.15b. Due to imperfect anti-reflection coat, increased cross-polar levels are seen in the $\phi = 45°$ plane patterns and also the back lobe level of $\sim -25\ dB$ w.r.t. on axis maximum is observed.

With the radiation patterns computed, the main characterization parameter i.e. η_G can now be computed. Similar to earlier antenna topologies from the simulate Far-field over complete sphere the η_G computations are performed using algorithm from **Paper C** for this structure. The computed Gaussicity values are are shown in Fig. 4.16a and corresponding beam parameters are shown in Fig. 4.16b.

As seen from the computed patterns (Fig. 4.15), there is significant radiated power in cross-polar levels and as well as some radiation in the back lobe direction. This directly translates to reduced η_{pol} as well as degraded η_{spill}. Therefore, even though the coupling of power from BOR_1 components to Gaussian beam is high ($\sim 90\%$) the overall Gaussicity is $\sim 60\%$. This value is in close agreement with the measured value of a similar lens design at 246 GHz as shown in Fig. 20 of [83].

With the presence of lens as a focusing component the resulting Gaussian beam has larger beam waist of $\sim 2\lambda$ as compared with earlier topologies. Also the ω_o stays constant over the operation bandwidth of $\sim 10\%$. The location of fitted beam waist is found out to be $18 - 19\lambda$ below the ground plane of MMIC and towards the air side.

$D_o = 25 dBi$

(a) 3-D Patterns

(b) $\phi = 45°$ plane patterns
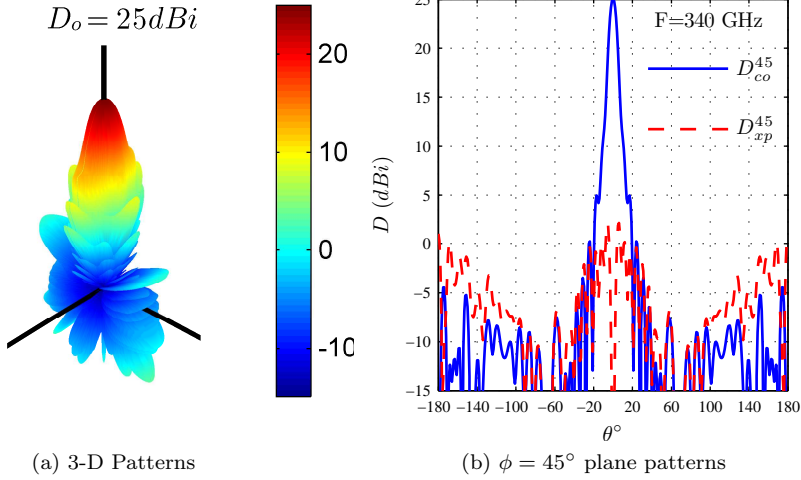
Figure 4.15: Radiation patterns of Differential Double Slot with Si Lens + Anti-reflection coat

(a) η_G

(b) beam parameters
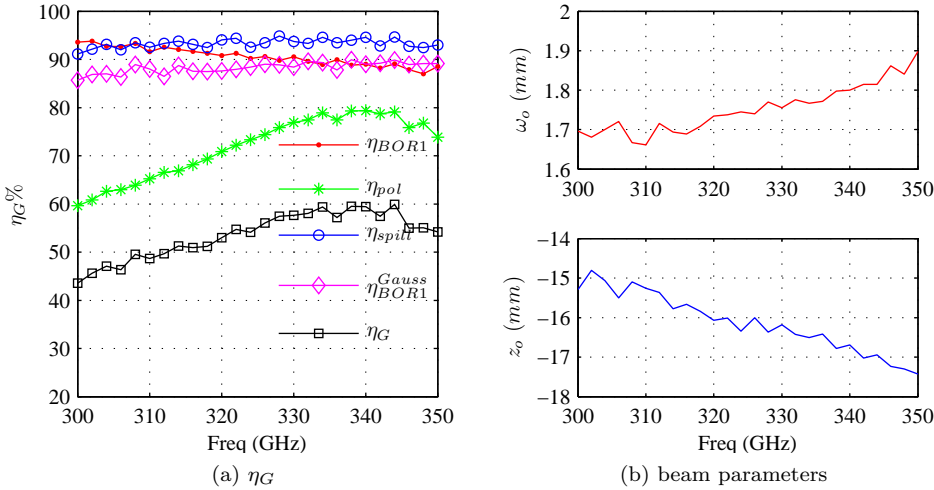
Figure 4.16: Gaussian Coupling Efficiency for Differential Double Slot with Si Lens + Anti-reflection coat

Thus with simpler lens structure such as a semi-hemisphere with cylindrical extension, moderate Gaussian coupling efficiencies can be obtained. But to further improve η_G values more extensive lens shape optimization process can be envisioned [93].

Another a similar design can be obtained by etching out a rectangular slot in the ground plane and feed it with a microstrip patch on a top metal. This topology has been fabricated in GaAs/InP substrate in [94, 95] but is not considered in this work due to higher cross-polar levels in the radiation patterns. Furthermore, the improvements in Si lens based structures are published recently using leaky wave antenna concept

Table 4.1: Comparisons of Planar Antenna Topologies

Topology	Process I/II	Z_c Ω	BW (%)	η_{ohmic} (dB)	η_G (%)	$\frac{\omega_o}{\lambda}$ @f_c	Area μm^2
2x1 Microstrip Patch Array	I	50	2.15	-3	92	0.28	350x750
2x2 Microstrip Patch Array	I	50	3.0	-3.65	95	0.37	880x880
4x4 Microstrip patch Array	I	50	4.0	-6.5	75	0.95	1500x1500
Double Slot with Si Lens	II	75	8	-0.4	60	2.05	150x350

BW @ $S_{11} \leq -10$ (dB)

[96, 97, 98] which has potential to form multi-pixel arrays for imaging [99]. This type of antenna structure will be considered as one of the future work directions.

4.6 Summary of Antenna Designs

In this chapter a selection is made on antenna topologies from the various basic antenna elements which are suitable to fabricate for MMIC processes discussed in the Chapter 2. Considering various selection criterion discussed in section 4.2, microstrip fed patch and microstrip fed slots are considered as the most suited elements. Based on this, both broadside and inverse broadside radiating antenna topologies are obtained in sections 4.4 and 4.5.

Since the intended use of these antenna topologies is for Quasi-optical system; all the antenna topologies presented in this chapter are evaluate in terms of ohmic, reflection and Gaussian coupling efficiencies. To have a consistent and fair comparisons between these topologies, the center frequency close to 340 GHz is chosen and from the simulated results important parameters such as bandwidth, efficiencies, beam parameters are obtained for each topology. These values are summarized in Table 4.1.

One more important aspect to consider for antenna topologies is the area they occupy on MMIC. For MMIC based structure considering cost and yield issues smaller areas are preferred. Hence, the selection of appropriate topology suffers from various performance trade-offs.

Microstrip patch based designs are attractive in terms of η_G but they occupy more area as well as have higher ohmic losses. On the other hand, slots based designs can be compact but for higher η_G values extensive Lens shape optimization is required.

Therefore, the choice of appropriate topology is very much dependent on the Quasi-optical system design and at this moment no clear conclusion is made on the choice of topology. But considering efficiency trade-offs, the 4x4 microstrip patch array topology can be modified for more compact integration with active components which maintaining high η_G. These aspects of integration are elaborated more in the Chapter 8. Hence, at this stage it is more evident to conclude that the differential way of feeding antenna arrays helps in reducing microstrip feed network as well as minimizing cross-polar levels. The additional advantage is the simplicity with which they can be combined with balanced mixers. These mixers are discussed in upcoming chapter.

Mixer Topologies

In majority of microwave heterodyne receiver systems a low noise amplifier is an irreplaceable component after the antenna for a low noise receiver. But for the sub-millimeter wave applications where low noise amplifiers based on modern transistors are still in research phase [33]; better established practice is to combine mixer as the first stage after an antenna.

Mixer begin a device having non-linear Current-Voltage characteristics (IVC), mixes a local oscillator (LO) signal and an input radio frequency (RF) signal. The resultant signal waveform have mixing products with sum and difference of LO and RF frequencies as well as higher order mixing terms. From this waveform a signal having a frequency equal to the difference between LO and RF frequency can be extracted using a low-pass filter and is referred as intermediate frequency (IF).

For a mixer the efficiency with which the information on RF frequency gets down converted to IF frequency is an important characterization parameter and it is often quantified as conversion loss (L_c) of a mixer. The conversion loss being a ratio of down-converted IF power to input RF power depends mainly on the LO signal power as well as on the mixer topology used. For THz applications where the LO power is often a limiting factor, a choice of appropriate mixer topology is more important. Therefore, this chapter focuses on various feasible mixer topologies and their comparison in terms of conversion loss, required LO power, bias conditions.

The profound work on mixers in microwave region has resulted in various different mixer circuits and topologies [100, 101, 102]. Out of these, the mixer topologies employing the transistor as an active device can be broadly classified in three categories, namely 1. Resistive Mixers, 2. Transconductance Mixers and 3. Gilbert Cell Mixers. Out of these resistive mixers and Gilbert cell mixers are commonly used for sub-harmonic operation where the LO frequency is half the fundamental frequency. The sub-harmonic mixers are more attractive in THz band since they can be pumped at $1/2F_{LO}$ where comparatively higher power is available.

Therefore considering the THz imaging applications as well as MMIC process of HEMT and HBT devices as a background, the scope of this chapter is limited to the Resistive and Gilbert Cell based mixer topologies with more focus on sub-harmonic topologies having balanced RF input. Each topology discussed in this chapter is compared in terms of its conversion loss and required LO power. Also to get a consistent comparison a RF frequency of 340 GHz and IF frequency of 4 GHz is chosen. The chapter concludes with a summary on mixer topologies and their possible integration with antenna elements discussed in the last chapter. The practical implementation of the antenna integrated mixers is discussed in the upcoming chapter.

5.1 Resistive Mixers

In its simplicity a mixer can be viewed as a switch whose switching action is controlled by a LO frequency as shown in Fig. 5.1a. With this approach, the applied RF voltage from the generator gets modulated with the switching waveform and resultant signal as a product of sinusoidal RF and Square Wave LO, appears across the load. By
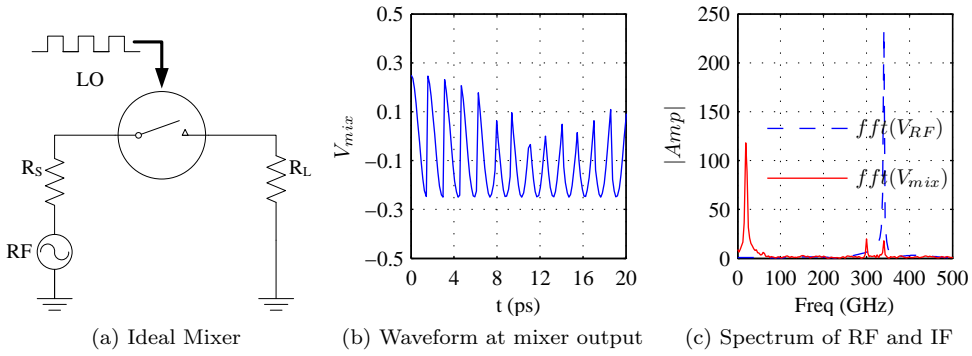
Figure 5.1: Ideal Switching Mixer

(a) Ideal Mixer (b) Waveform at mixer output (c) Spectrum of RF and IF

assuming source and load impedances are complex conjugate matched ($Z_S = Z_L^{\star}$), the resultant output voltage waveform across load resistor can be numerically computed. To further illustrate this a LO voltage of 1V peak amplitude is mixed with sinusoidal RF voltage of 0.25V peak amplitude at frequency of 340 GHz. The mixing waveform is shown in Fig. 5.1b and corresponding spectrum is shown in Fig. 5.1c. From the amplitudes of the FFTs, the L_c is numerically computed as the ratio of amplitudes at IF and RF as given in (5.1).

$$L_c = -20 \cdot \log_{10} \left| \frac{V_{IF}}{V_{RF}} \right| = 3.9 \ dB \tag{5.1}$$

This type of mixer in reality can be implemented using a resistor whose resistance varies linearly between very low (few Ω) to very high $\gg k\Omega$ values. Since, the mixing of frequencies is obtained mainly by linear time-varying resistor, these mixers are referred as resistive mixers and are inherently lossy. i.e. they can not offer conversion gain. Even though lossy, these mixers are very attractive since they offer very low intermodulation due its linear mixing property.

The practical way to implement this type of mixer is to use a FET at very low or zero drain bias since at zero drain bias ($V_{DS} = 0$) the channel resistance of FET behaves very similar to linear resistor whose value can be controlled by applied bias at the gate. A FET with very low on resistance (R_{ON}) and high off resistance (R_{OFF}) becomes analogous to the switch shown in Fig. 5.1a and its theoretical lowest conversion loss becomes $\frac{\pi^2}{4}$ i.e. 3.9 dB. The detail analysis on these type of FET based resistive mixers can be found in [103, 104, 105].

Based on this operating principle various different topologies of resistive mixer exists today, out of these a few topologies which are more appropriate for THz MMICs are considered below. Since, a resistive mixer can only be implemented using FET device, a 2 x 20 μm HEMT device from TSC 50nm HEMT MMIC process is chosen for performance comparison of different topologies in subsequent sub-sections.

5.1.1 Fundamentally Pumped Single Ended

This type of mixer first appeared in [106] and uses a FET device with fundamentally pumped LO at the gate and RF is applied at the drain. The IF is extracted from the drain with the use of a low pass filter as shown in Fig. 5.2a. Typically at RF side a

(a) Topology   (b) Conversion Loss
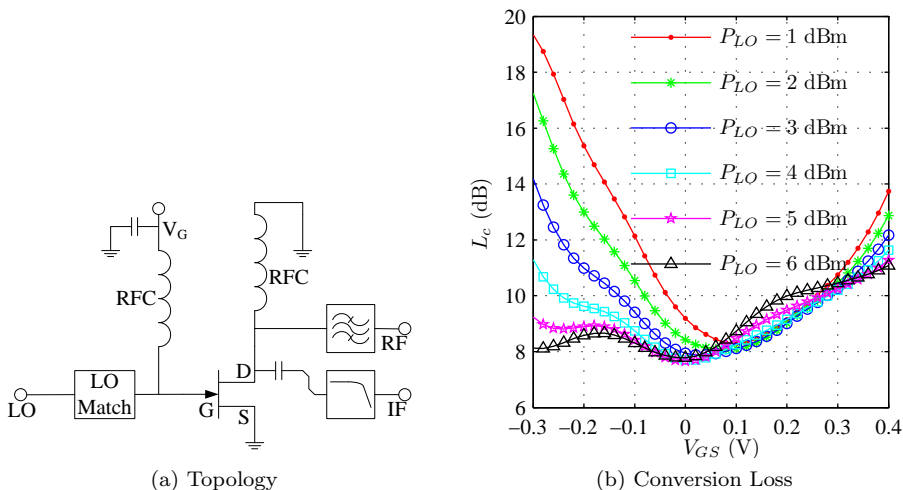
Figure 5.2: Fundamentally Pumped Single Ended Resistive Mixer

short circuit termination is placed at LO frequency and similarly short circuit for RF at the gate is introduced. The drain is grounded for DC using a RF choke. The gate is biased close to pinch off and is driven with higher LO power.

To understand this behavior, a 50nm 2 x 20 μm HEMT device is used for simulation with ideal passive components. The required filters at RF, IF and short circuit terminations are assumed ideal in simulations to extract out conversion loss which now predominantly depends upon the device. The L_c as a function of V_{GS} for different LO powers is shown in Fig. 5.2b for applied RF frequency of 340 GHz and LO pump frequency of 336 GHz resulting in 4 GHz IF.

The simulated conversion loss with ideal passive components is $\sim 8-9$ dB for close to zero gate bias and with moderate LO power levels of 4-6 dBs. This is higher than theoretical minimum of 3.9 dB due to non-ideal conductance waveform of the device. This topology is integrated with corporate feed based double slot antenna using 100nm GaAs mHEMT process and its details are presented in the **Paper D** of this thesis.

5.1.2   Fundamentally Pumped Balanced

The topology of Fig. 5.2a can be modified by using two HEMT devices with RF applied in Phase to the drains while LO applied out of phase to the respective gates as shown in Fig. 5.3a. The design considerations for this topology are similar to that of single ended resistive mixer. The advantage with this topology is the drain terminals are virtual ground for LO giving required short circuit for LO frequencies at the drain. The simulated L_c values are slightly better than that of singled ended version as shown in Fig. 5.3b.

Approximately 2 dB improvement in L_c is seen from Fig. 5.3b when the device is biased at V_{GS} of -0.2 V (This is a pinch off voltage for 2 x 20 μm device as seen from 2.5b). This negative gate voltage demands for harder pumping of the device by LO frequency resulting in 10 dB LO power requirement for lowest conversion loss. This high power is often difficult to achieve at such high frequencies (> 300 GHz). There-
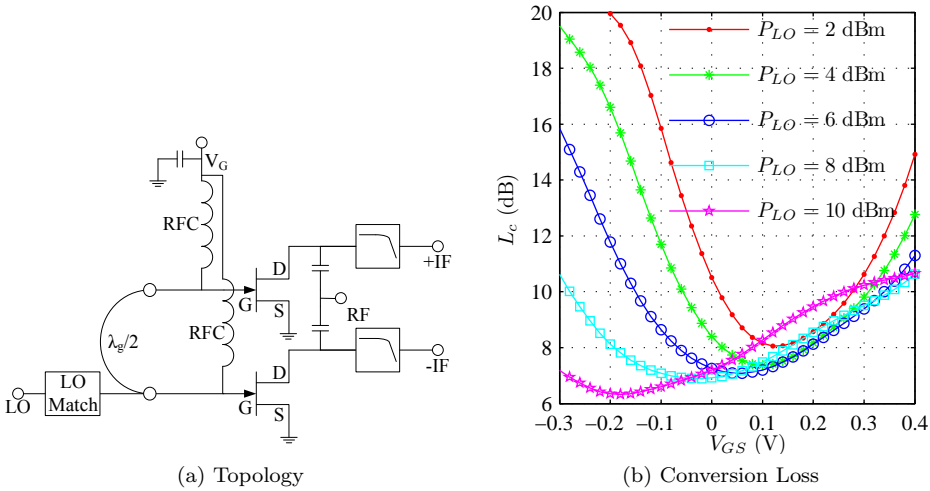
Figure 5.3: Fundamentally Pumped Balanced Resistive Mixer

fore, the possibilities of mixer to be pumped at the sub-harmonics of LO frequency is of advantage. Practical implementation of this topology with integrated double slot antenna is presented in the **Paper D** of this thesis.

5.1.3   Sub-Harmonically Pumped Single Ended

The main advantage of using sub-harmonically pumped resistive mixer is the pumping frequency being half the fundamental frequency. Since at mm, sub-mm wavelengths the lack of LO power is often a constraint in mixer conversion loss optimization, the ability to pump a mixer at lower frequency where comparatively higher LO source power is available, makes sub-harmonic mixers as a preferred choice. Along with this attractive feature, the use of sub-harmonic frequency for LO directly helps in achieving high LO-RF and LO-IF isolation.

Also considering phase noise requirements on LO source, it is a common practice in THz band to employ a low noise VCO along with multiplier chains to produce required LO frequency instead of direct design of VCO at desired frequency. This reflects on the fact that if the mixer is fundamentally pumped then the MMIC would require multiplier chain which is capable of producing fundamental LO frequencies and in turn MMIC complexity and area would grow due to integration of more multiplier blocks. Therefore, if the mixer is sub-harmonically pumped it helps in reducing LO drive complexity since usually a last doubler (x2 multiplier) can be omitted.

The diode based sub-harmonic mixers have been known since a long time but HEMT based resistive sub-harmonic mixers first appeared in 1991 [107] and later in [108]. The basic topology of this type of mixer is shown in Fig. 5.4a. In this topology, the LO is applied out of phase at the gates of two parallel transistors with drain terminals tied together and source is grounded. The RF is applied in phase at both drains and IF is extracted by a low pass filter at the same node.

The main principle of operation is that with both transistors biased close to pinch off, the first half of LO cycle turns on first transistor while the second one is in cut-off. In the next half cycle the situation is reversed with first transistor now is in cut-off

(a) Topology   (b) Conversion Loss
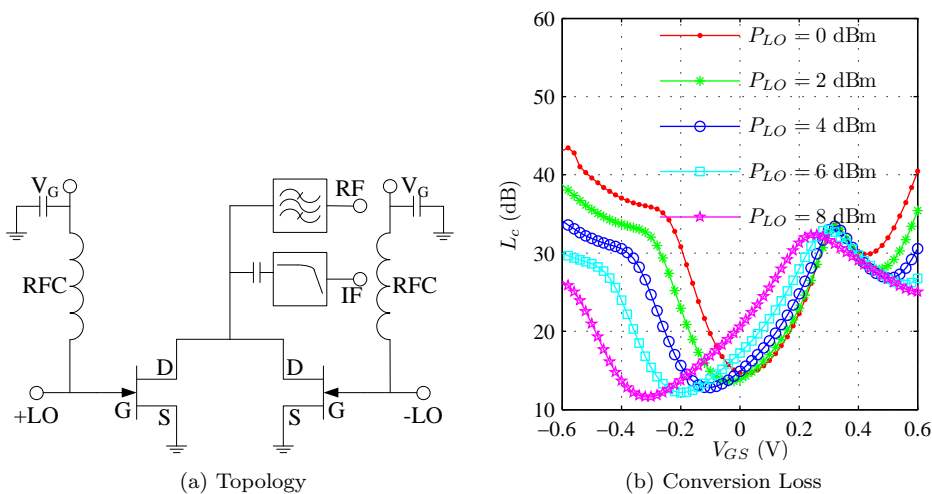
Figure 5.4: Sub Harmonically Pumped Single Ended Resistive Mixer

(a) Topology   (b) Conversion Loss
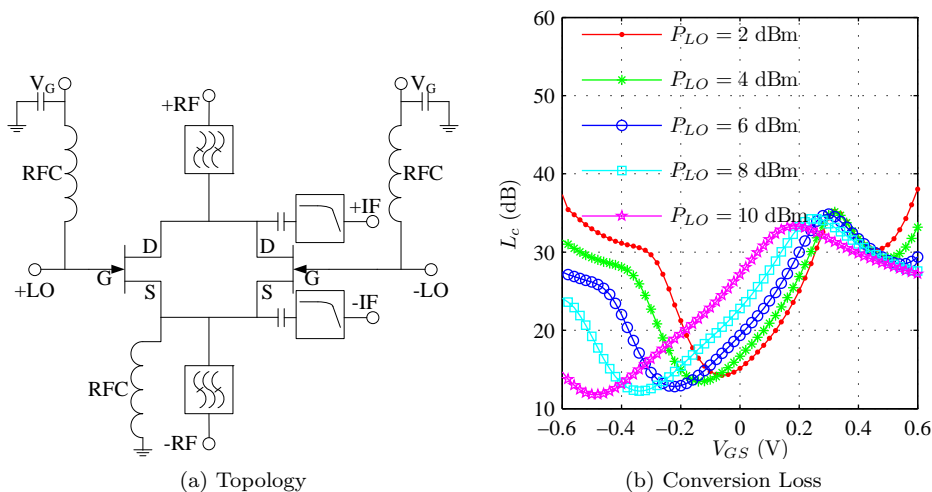
Figure 5.5: Sub Harmonically Pumped Balanced Resistive Mixer

while the second is turned on. This results in a conductance waveform similar to full wave rectified sinusoid having only even harmonics of the applied LO frequency. Since drain terminals are at virtual ground for applied LO frequency no mixing occurs for the fundamental component. On the other hand, the even harmonics are present at the drain and since second harmonic being strongest of all, it gets mixed with applied RF to produce down converted IF signal.

The only draw back of this topology is that it has conversion loss at least few dBs worse than the fundamentally pumped mixers. This is clearly seen in Fig. 5.4b where the variation L_c as a function of LO power and gate bias is plotted. The lowest $L_c \sim 12$ dB is higher by 4 dBs when compared with L_c obtained in Fig. 5.2b.

5.1.4 Sub-Harmonically Pumped Balanced

As discussed in the earlier section, a sub harmonic mixer is the preferred choice for MMIC based circuits since it can offer less complexity, lower intermodulation as well as it assists in making compact size MMIC circuits. The topology of single ended sub-harmonic resistive mixer discussed in earlier section has single ended RF input. Thus for an attempt to integrate it with planar antenna topologies discussed in last chapters, the antenna needs to have singled ended RF output which in turn require corporate based feed network having several drawbacks.

Therefore if the topology of the sub-harmonic mixer can be modified to accept balanced RF signal then it would be easier to integrate it with the balanced antenna. In this way both compactness in MMIC layout as well as low loss, low cross-polar, high η_G antenna integrated mixer can be achieved. This can be done by applying differential RF across drain-source instead of grounding the source as in the previous topology. The IF can be extracted differentially across drain and source terminals and can be amplified further with differential low noise amplifier. The gate bias can still be applied to bias the channel close to pinch off but in this case special care has to be taken to ground the source terminal for DC. The resulting topology is shown in Fig. 5.5a and corresponding L_c is shown in Fig. 5.5b.

The resulting conversion loss is comparable to single ended version of sub-harmonic mixer and for 6 dBm LO power it is $\sim$ 12.8 dB for $V_{GS} = -0.2$ V. It is still 3-4 dB worse than fundamentally pumped but this differential topology comes with a advantage that it retains all good properties of single ended sub-harmonic mixer as well as it is extremely suitable to integrate with balanced planar antenna structures. This topology has been fabricated using 50nm HEMT process with integrated differential Double slot antenna and its successful implementation is given in the **Paper B** of this thesis.

Another variant of this topology is to feed both gates of the transistor in phase, thus the conductance waveform becomes similar to half-wave rectified sinusoid and then its second harmonic can be used for mixing. Thus it becomes very similar to harmonic mixer. This makes the mixer layout more compact since the need of LO hybrid is eliminated but this comes with a trade off that the mixer conversion loss worsens further by a few dBs.

5.2 Gilbert Cell Mixers

The Gilbert cell mixer originates from a four quadrant multiplier circuit and it can be seen as a doubly balanced mixer [102, 109]. This type of mixer predominantly uses bipolar transistor for implementation and its operation is similar to doubly balanced FET mixer. The example of HEMT based Gilbert mixer can be seen in [110]. However in this thesis, the focus is mainly given on bipolar transistor based Gilbert cell mixers which can be implemented using 250nm DHBT MMIC process discussed in the Chapter 2. Therefore in this section both fundamentally and sub-harmonically pumped Gilbert cell mixer topologies are presented and their performance is evaluated using 250nm DHBT devices.

5.2.1 Fundamentally Pumped Balanced

The basic topology of fundamentally pumped Gilbert cell mixer is shown in Fig. 5.6a and its operation is similar to doubly balanced FET mixer [101]. The circuit employs 8 bipolar transistors, out of which transistors Q1-Q4 are used as switches driven by

(a) Topology

(b) Conversion Loss
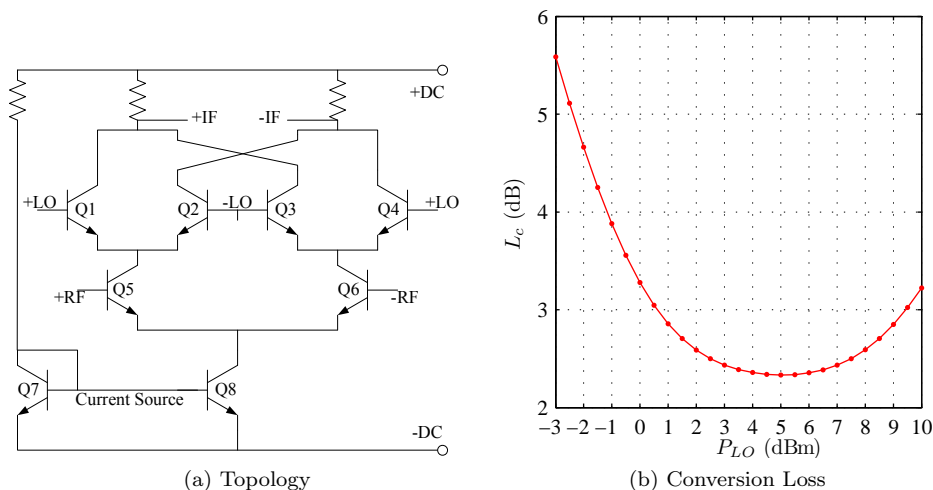
Figure 5.6: Fundamentally Pumped Gilbert Cell Mixer

LO. The transistors Q5-Q6 are biased in active region and they form a differential amplifier for RF signal. The transistors Q7-Q8 are used to form a current mirror at the emitter of Q5-Q6.

The collectors of transistors Q5-Q6 are virtual ground for LO frequency while the common emitter of transistor Q5-Q6 becomes a virtual ground for RF. The IF is extracted differentially across the collectors of transistors Q1-Q4. In one LO cycle the transistors Q1-Q2 switches on and off alternatively forming a switching waveform which results in mixing.

The simulated conversion loss values for this type of mixer using $0.25x4$ μm TSC DHBT devices is shown in Fig. 5.6b. Again to the RF frequency of 340 GHz and IF of 4 GHz is chosen for simulations with ideal LO feeding network and IF baluns. The LO transistors are biased closed to cut-off while RF transistors are in active region. The lowest L_c of ~ 2.5 dB is found for LO power of 5 dB.

5.2.2   Sub-Harmonically Pumped Balanced

The fundamentally pumped Gilbert mixer topology can be modified to operate as a sub-harmonic mixer by introducing additional four bipolar transistors as LO switches as shown in Fig. 5.7. As seen from the Fig. 5.7, the mixer core consists of four switching pairs of HBTs which are biased in cut-off and driven hard by applied LO at the base with appropriate phase.

The lower transistor pair (Q9-Q10) is biased in active region and balanced RF signal is applied to its base. Similar to fundamentally pumped configuration the lower transistor pair acts as a differential amplifier for RF signals and hence emitters of it are at virtual ground for RF. Analogous to this operation, the emitters of all switching pairs are virtual ground for LO and no LO voltage exists on the collectors of RF transistors (Q9-Q10).

For minimum conversion loss, the biasing of the transistors is very important and further optimization can be performed using appropriate device size for LO, RF and current mirror transistors. As a design example in this chapter, the lowest possible
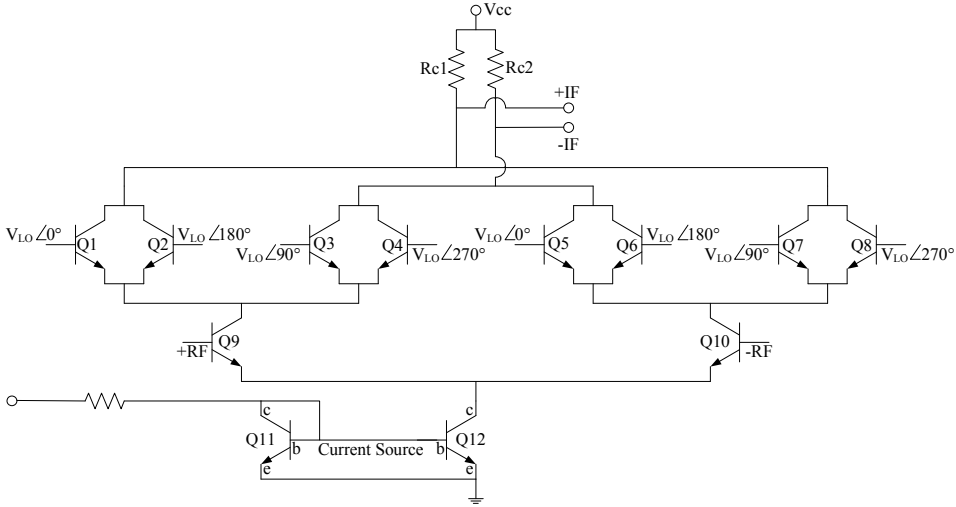
Figure 5.7: Topology for Sub Harmonic Gilbert Mixer

size of $0.25x2$ μm with minimum parasitics is used for LO switching pairs (Q1-Q8). The DC bias current at the collector for RF transistors (Q9-Q10) is typically ~ 4 times the collector current on any one of LO transistor. Therefore, the RF transistor must be capable of handling higher DC currents. This reflects on the selection of $0.25x4$ μm device for RF differential pair. And finally $0.25x6$ μm device is used for current mirror formed by Q11-Q12 to limit max. current to ~ 7 mAs. The resultant bias conditions are shown in Fig. with I_B, I_C and V_{BE} marked for each transistor.

(a) DC Bias

(b) Conversion Loss
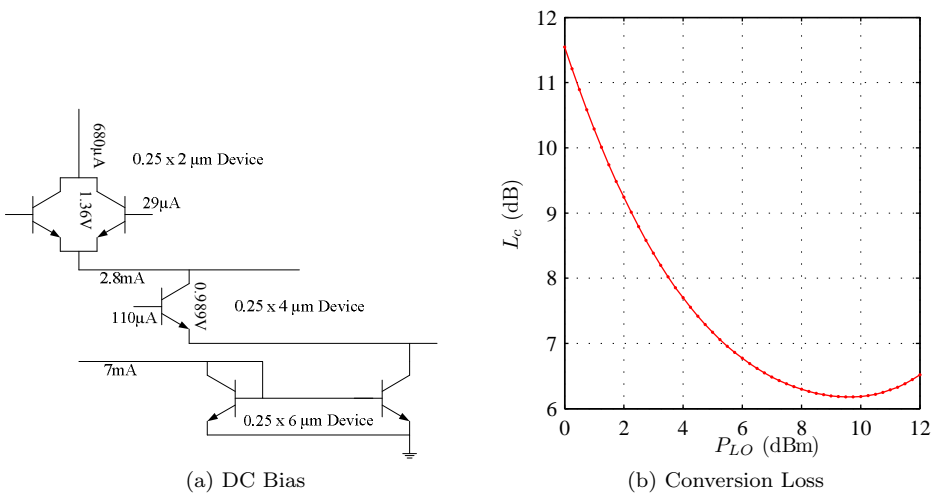
Figure 5.8: Sub-Harmonically Pumped Gilbert Cell Mixer Performance

The lowest $L_c = 6.2$ dB is seen for LO power of ~ 10 dB. This shows the L_c is worse

Table 5.1: Comparisons of Mixer Topologies

Topology	Process	LO	RF (dB)	IF (dBm)	L_c	P_{LO}
Resistive	50nm HEMT	Fundamental	Unbalanced	Unbalanced	8	6
Resistive	50nm HEMT	Fundamental	Balanced	Balanced	7	6
Resistive	50nm HEMT	Sub-Harmonic	Unbalanced	Unbalanced	12	6
Resistive	50nm HEMT	Sub-Harmonic	Balanced	Balanced	12	6
Gilbert	250nm DHBT	Fundamental	Balanced	Balanced	2	6
Gilbert	250nm DHBT	Sub-Harmonic	Balanced	Balanced	7	6

L_c @ $F_{RF} = 340\ GHz\ F_{IF} = 4\ GHz$

than fundamentally pumped topologies but still the advantage of pumping the mixer at 1/2 LO frequency can be seen as an advantage for sub-millimeter wave applications. This type of sub-harmonic mixer is implemented using 250nm TSC DHBT process along with an differential 2 x 2 microstrip patch antenna and is presented in **Paper A** of this thesis. Another possible implementation scheme using stacked LO approach for sub-harmonic Gilbert mixer is discussed in [111, 112].

5.3 Summary of Mixer Topologies

In this chapter, various different mixer topologies using both state of the art HEMT and HBT devices are presented. Even though, the conversion loss values obtained use ideal components they reflect well on the behavior of each mixer topology. The purpose here is to summarize these topologies and compare them. The Table 5.1 shows the summary of L_c values obtained using these topologies. For more consistent performance evaluation a fixed LO power of 6 dBm is chosen.

It is obvious that fundamentally pumped mixers achieved lower conversion loss values but considering MMIC based implementation at THz frequencies the sub-harmonic topology is preferred. Also considering their integration with differential antenna, the balanced RF input with balanced IF output based mixer topology has better advantage. Hence, sub-harmonically pumped balanced mixer topologies are conclusively preferred choice for antenna integrated MMICs. The practical realizations of these topologies are presented in **Paper A**, **Paper B**. Based on this understanding as well as the review of antenna topologies from the last chapter, a discussion on practical integration schemes for antenna integrated heterodyne receivers are presented in the next chapter.

Discussion on Antenna Integrated Heterodyne Receivers

In this thesis, the focus has been on integration of antenna with heterodyne receiver architectures using MMIC process. The goal at this work is to achieve multi-pixel receivers in lower end of THz band around 340 GHz. To reach this goal various different antenna integrated mixers are designed and tested at lower frequencies first and the experienced gained from low frequency work has been translated on possible integration schemes in sub-millimeter wave bands. Therefor this chapter mainly summarizes the measured results obtained based on the work carried out in this thesis.

The Chapter 4 of this thesis has discussed different antenna configurations while the Chapter 5 has summarized different mixer topologies. Now, these topologies can be combined together to form a antenna integrated heterodyne front end. Based on this, in subsequent sections the manufactured prototypes of such receivers in different frequency bands are presented along with a brief discussion on implementation aspects and measured performance. The antenna integrated circuits presented here are from the **Paper A, B, D and E** of this thesis.

6.1 4x4 Microstrip Patch Array with Self-Oscillating Mixer

For antenna integrated mixer circuits, LO source is foremost requirement. Therefore, if the LO is also generated on chip then higher level of integration can be achieved. A neat idea to achieve this is to use a combinations of oscillator and a mixer achieved by the same transistor. This is referred as a self oscillating mixer (SOM) [113]. A SOM can be designed as a combination of a single-ended mixer and a common source oscillator. The MMIC based transistors having $f_{max} \gg 100 GHz$ can be used to fabricate such a SOM for THz applications [114].

In this work however (**Paper E**), low frequency 24 GHz band is chosen for validating the operation of this type of mixers. Also considering the requirement of sub-harmonic mixing at THz frequencies, the SOM topology is made balanced as shown in Fig. 6.1a. It uses two identical SOM which are connected together by a transmission line at respective gate terminals. The middle point of the gate transmission line acts as virtual ground.

The principle of operation is both transistors are made to oscillate at sub-harmonic frequency. (i.e. 12 GHz in this case) The oscillation signals by these two transistors become 180 degree out of phase. And therefore at the middle point of gate transmission line they cancel out. Thus the fundamental frequency and all odd harmonics of LO cancel out at both RF and IF ports, while the even harmonics add in phase.

Now the applied RF at the middle point is down converted into IF by mixing of RF and the second harmonic of LO. The virtual ground condition at the middle point make oscillation condition independent of applied RF.

The manufactured prototype using this topology is shown in Fig. 6.1b. The RF is applied through the on board antenna. Due to availability of only one metal layer for antenna, the patch antenna array of 4x4 elements is designed [82] and is integrated

(a) Topology (b) Prototype
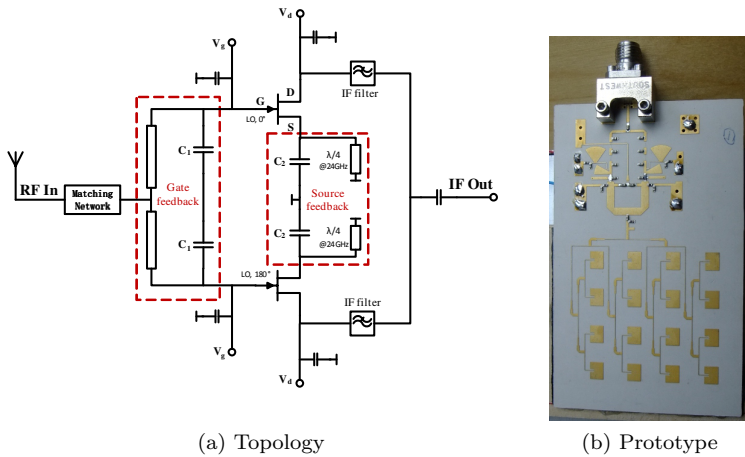
Figure 6.1: Self Oscillating Mixer with Integrated Patch Array

with the balanced SOM. The conversion loss of SOM alone is measured and is found to be better than 15 dB. The patch antenna array achieved a gain better than 16dB. The integrated receiver has shown a 3dB-bandwidth of 800 MHz with peak effective isotropic receiver gain of 5.9 dBi.

Thus the principle of operation of balanced SOM with integrated antenna is evaluated and design of such topology in THz bands is considered as one of the future work directions along with important aspect of LO phase locking for multi-pixel systems.

6.2 Double Slot Antenna with Resistive Mixer

In this work the Double slot antenna as discussed in section 4.5.2 is used to integrate it with a resistive mixer using 100nm GaAs mHEMT technology. Both single ended as well as balanced resistive mixer topologies discussed in section 5.1.1, 5.1.2 are implemented at the operating frequency of 200 GHz. The LO is fundamental and for pumping the chip the LO power of 3-5 dBm is used. The photographs of the fabricated chips are shown in Fig. 6.2a and Fig. 6.2b respectively.

The measured results from **Paper D** on these chips show that the L_c of ~ 8 dB was obtained from the single ended resistive mixer while the L_c of ~ 12 dB was obtained for balanced versions. With antenna gain taken into account, the effective isotropic receiver gains of 15.4 and 11.2 dB were measured for respective mixers.

For resistive mixer it is usually known that the noise figure is similar to its conversion loss, since the thermal noise is the dominant contributor. But to measure such high noise figures (> 10 dBs), the conventional Y-factor method is not suitable since the resultant Y-factor becomes comparable to the measurement accuracy of power meter. To counter this problem, a modified method for measurement of high noise figure is developed and this method is described in detail in *Appendix C*. Using this new method the above mixers are evaluated for their noise figure. And it is found that the noise figure of antenna integrated receiver is approximately 1 dB higher than the conversion loss of the respective mixer. Therefore more efforts can be put in this direction to qualitatively understand sources of noise in the resistive mixers.

(a) Single Ended   (b) Balanced
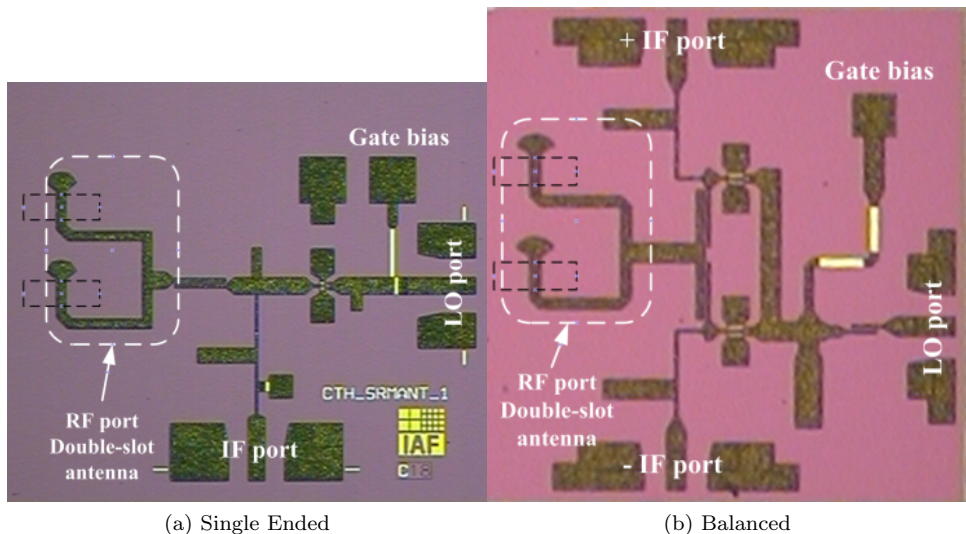
Figure 6.2: Corporate Feed based Double Slot Antenna with Resistive Mixer

Considering the results obtained in this paper, the integration of antenna with mixer worked well but due to corporate based feeding the area of occupied on the chip is high.

6.3 Differential Double Slot Antenna with Sub-Harmonic Balanced Resistive Mixer

The shortcoming from the before mentioned work, is the compactness of the topology. It is still a combination of two different layouts on one chip rather than effective integration. To overcome this drawback, two important steps are necessary. 1. Make the output of antenna differential and remove RF hybrid and 2. Implement balanced mixer topology. The first step can be done by using the differential topology of double slot antenna as shown in Fig. 4.13 along with a balanced resistive mixer discussed in section 5.1.3. The choice of sub-harmonic balanced mixer for THz frequencies is obvious because of the availability of more LO power at lower frequencies.

This discussion results in a new topology which is here referred as Differential Double Slot Antenna with Balanced Sub-Harmonic Resistive Mixer and is shown in Fig. 6.3. This novel topology is fabricated using 50nm TSC HEMT technology and details of the design are presented in **Paper B**. The photograph of the fabricated chip is shown in Fig. 6.3b.

The novelty with this topology is the HEMTs can be directly placed between two double slots. This results in improved compactness as well as elimination of extra microstrip lines to bring RF signals from antenna to Drain-Source terminals.

The measured results on this topology show that the Sub-Harmonic mixer can achieve 15 dB conversion loss with relatively low LO power of +3 dBm at 100 GHz and corresponding Noise Figure is $\sim 1-2$ dB higher than the conversion loss. Even though higher conversion loss as compared to fundamentally pumped mixer (~ 12 dB) the resultant topology is very compact and more preferable for multi-pixel front ends.

(a) Topology   (b) Fabricated MMIC
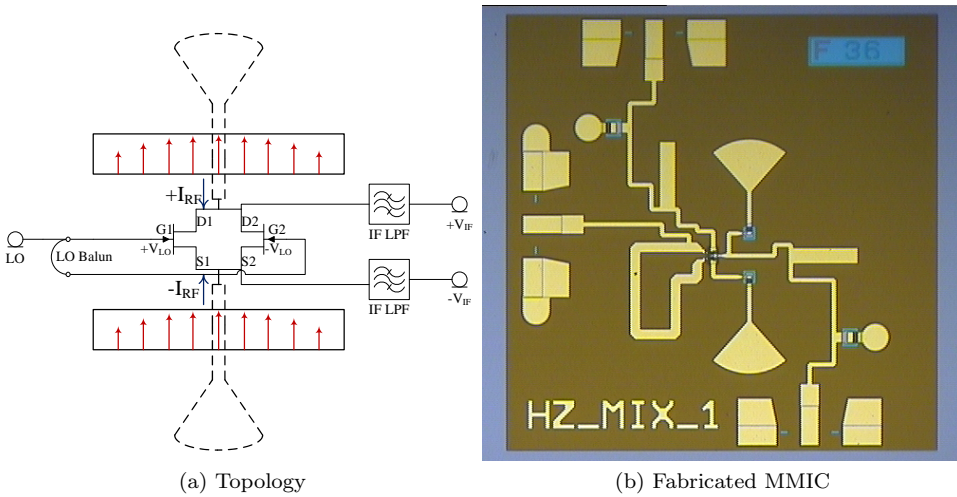
Figure 6.3: Differential Double Slot Antenna with Balanced Sub-Harmonic Resistive Mixer

The same topology can be made even more compact by exclusion of LO BALUN. This results in phase excitation of LO at the two gates of the HEMTs and the mixing occurs using the second harmonic of the transconductance waveform. This worsens the conversion loss further. Furthermore, the area of the chip can be reduced using Via-hole matched slot antennas instead of radial stubs. With this approach, the measured L_c of the integrated receiver was found to be 16.5 dB for +4 dBm of LO power.

The results obtained with this novel topology are very encouraging. The lower value of conversion loss can be optimized further by doing careful study of on L_c dependence on the device size and this has been considered as one of the future work directions. Also the improvement in LO BALUN, IF filters as well as integration with active differential amplifier would assists in improving performance of this topology.

6.4 Differential 2x2 Microstrip Patch Array with Sub-Harmonic Gilbert Mixer

The earlier work clearly highlights the usefulness of having differential antenna with balanced mixer, and the experience gained from that work has been extended to achieve a target frequency of 340 GHz using 250nm TSC DHBT technology. Since with this MMIC process, the broadside radiating antenna elements are feasible a 2x2 microstrip patch array is integrated with sub-harmonically pumped Gilbert Cell mixer as discussed in section 5.2.2. The details of this design are given in **Paper A**.

The block diagram of this MMIC is shown in Fig. 6.4a. The design using this approach consists of a sub-harmonic Gilbert mixer along with its LO phase network comprising of one 180° hybrid and two 90° hybrids. The differential IF amplifier is also integrated. The 2x2 differential microstrip patch antenna arrays is used to feed balanced RF to the mixer. The fabricated chip photo is shown in Fig. 6.4b.

The measured performance of this MMIC at 338 GHz RF and 170GHz LO with +4 dBm LO power, show peak gain of 11.8 dB for the entire antenna integrated receiver. For the mixer+ IF amplifier with antenna excluded the measured conversion gain is

(a) Chip Block Diagram   (b) Fabricated MMIC
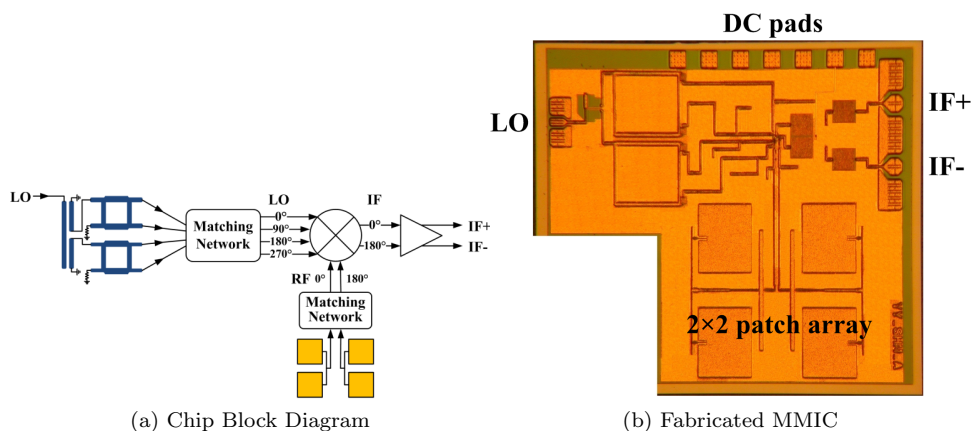
Figure 6.4: Differential 2x2 Patch Array with Gilbert Cell Mixer

found out to be 14.0 dB. A double-sideband noise figure of 17 dB at room temperature is also measured for this chip.

The performance of chip over RF band of 320-338 GHz shows the receiver gain variation of 3-12 dB. This has mainly due to poor antenna ohmic efficiency, narrow bandwidth as well as un-optimized gain flatness of IF amplifier. Even though not the best performance, the topology shows substantial potential for planar multi-pixel front ends. And it can be improved further by careful design of IF amplifier along with integration of LO multiplier chains.

Conclusions

The work carried out in this thesis deals with detail characterization of antennas for different applications and their integration with active devices using MMIC technology.

Out of different antenna characterization parameters the ohmic efficiency and reflection efficiency are important for possibly every application of antennas. Therefore minimization of antenna losses and improving impedance bandwidth will always be a part of design challenge.

The more application specific characterization parameters are aperture and Gaussian coupling efficiencies. The η_{ap} is mainly used when the intended use of the antenna is as a feed for reflectors and it reflects on the deviation from the maximum possible directivity for given size of the aperture. While the η_G reflects on coupling of radiation from antenna to Quasi-optical systems. For sub-mm wave applications, the characterization of planar MMIC antenna interms of η_G is more relevant along with η_{ohmic} & η_{refl}.

The integration of antennas with MMIC is feasible at sub-millimeter wavelengths. And practical choice is to integrate antenna with a sub-harmonic mixer. Considering, the goal of maximizing η_G values a single antenna element is often not enough and therefore small arrays of antenna elements can be used to shape the pattern for higher η_G.

The integration of antenna array based on corporate feed with mixer suffers from the higher cross-polar levels as well as higher physical area. These limitations can be overcome by making differential feeding network for antenna arrays and integrating them with balanced sub-harmonic mixer topologies.

The HEMT based balanced sub-harmonic resistive mixers can achieve conversion loss better than 15 dB and they can be integrated with differentially fed slot antenna arrays. The use of dielectric lens on such array of double slots can achieve rotationally symmetric radiation pattern and Gaussian coupling efficiency of $\sim 60\%$. These values can be improved by Lens shape optimization.

The HBT based sub-harmonic Gilbert cell mixers can achieve conversion loss better than 10 dB and can be integrated with broadside radiating differential microstrip patch arrays.

To conclude, differentially fed antenna with a balanced sub-harmonic mixer results in compact antenna integrated heterodyne receiver. Their practical implementation as a single pixel has been successfully demonstrated in this thesis. The compact integration along with low LO power requirement are key aspects to push these design topologies further for multi-pixel heterodyne frontends for various THz applications.

CHAPTER 8

Future Work

The work carried out in this thesis reflects on practical implementation of single pixel antenna integrated heterodyne receiver frontends using MMIC technology in sub-mm wave band. The concluded choice of differential antenna with a balanced sub-harmonic mixer is considered as a way forward to make multi-pixel front ends.

Considering multi-pixel THz imaging applications, the overall goals for future work can be summarized as follows.

- Pattern shaping for higher Gaussicity

- Effect of mutual coupling in linear antenna arrays

- Impedance bandwidth improvements ($> 10\%$) to improve radar range resolutions

- Minimization of conversion loss of sub-harmonic mixers

- Minimization of LO power requirements

- Integration of LO multiplier chains and IF amplifiers

- LO phase locking on multi-pixels

With this big wish list full of trade-offs, based on the work in this thesis some guidelines/directions can be extracted. Therefore comments are made on possible future work using both HEMT and HBT technology.

HEMT based circuits

The HEMT based circuits with 50nm and beyond transistor technology is now offering f_{max} close to 1 THz. With this modern transistors, the foremost work seen is to quantify effect of device size on the conversion loss of resistive mixer. The noise of the mixer can also be studied.

Considering the goal of multi-pixel system, in antenna perspective the detail studies of off axis fed Lens antenna is required. The double slot feeding structure with balanced resistive mixers have shown compact integration at 200 GHz and therefore they can be scaled down to 340 GHz and can be designed to form linear array of Nx1 pixels giving off axis feedings for dielectric lens. The off-axis feeding results in angularly separated beams for which the optimization of lens shape for higher η_G is required. Therefore accurate modeling of lens using GO-PO tools and shape optimization is foreseen as well.

The HEMT based multiplier chains as well as IF LNA integration is also important aspect of such multi-pixel MMICs. And here the influence on mixer conversion loss due to the available LO power from multiplier chains need to be studied.

HBT based circuits

The 250nm HBT presented in this thesis already have f_t close to 350 GHz. The use of this transistor for balanced sub-harmonic Gilbert mixer has resulted in working circuit at 340GHz. Therefore, the same MMIC process can now be pushed to higher level of integration.

The 2x2 microstrip patch array integrated with Gilbert mixer works well but suffers from the drawback that its radiation pattern is broad. This results in narrow beam waist and fast diverging beam. This limitation can be overcome by using 4x4 microstrip patch array. But this array occupies substantial place on MMIC. Hence, the array can be split in two 2x4 sub-arrays.

For each 2x4 sub-array, the integration of sub-harmonic mixer, LO multiplier chain and IF amplifier is feasible. Therefore, the IF outputs of sub-arrays can be combined either by analog or digital means to form a 4x4 array. The conceptual block diagram of this 2x4 array with integration scheme is shown in Fig. 8.1.
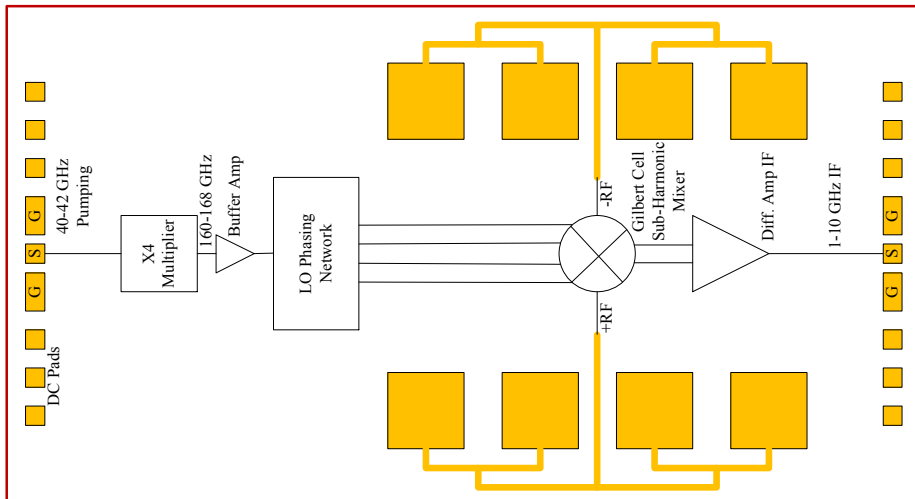
Figure 8.1: Block diagram of Half Pixel formed by 2x4 sub-array

Since one 4x4 array is formed by two 2x4 arrays, the chip layout of Fig. 8.1 is considered here as half-pixel. The main advantage with this approach is that the linear stack of such N+1 half pixels can be fabricated on MMIC and from which N simultaneous spatially separated beams can be achieved. For. e.g. the outputs of sub-array 1 and 2 can be combined to form first beam, the second beam results from in phase addition of half-pixel 2 and 3. The possible system integration of this concept is shown in Fig. 8.2.

This new concept is considered as a major future work direction. The advantage with this concept is the beams are spatially separated by only half the pixel size but still maintains moderate beam wait ($\sim \lambda$) and high η_G, typically $> 75\%$ as discussed in section 4.4.3. The effect of beam squint as a function of frequency as in the case of off-axis fed lens is also eliminated.

Therefore in upcoming future more focus will be on higher level of integration, LO power studies from multiplier chains as well as combination of IF outputs in digital domain.
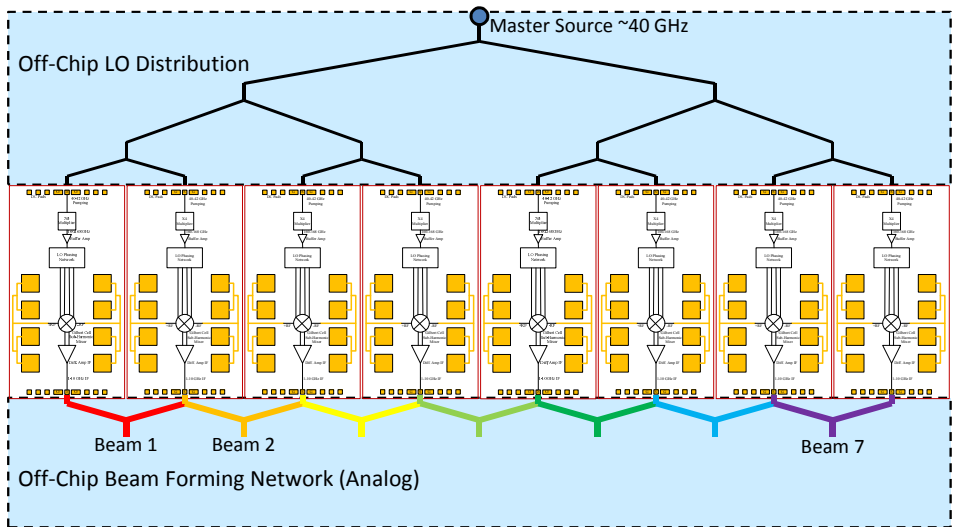
Figure 8.2: System integration of N+1 Half Pixels for N parallel beams

The effect of spatially separated beams in Quasi-optical focusing systems has to be studied as well to map actual beam shapes in the imaging plane at larger distances (> 25 m).

The current antenna ohmic efficiency with $5\mu m$ thick BCB layers from MMIC process is poor ($\sim 6-8$ dBs). Therefore, in process point of view thicker BCB layers are required to improve the bandwidth and ohmic loss of patch arrays.

Summing of all together, the multi-pixel heterodyne frontends for THz applications are in a rapid development stage and in near future of 3-5 years such complex, highly integrated frontends would facilitate the efficient use of relatively less explored THz band.

Here it is worth highlighting that the such advanced THz systems would result only by multi-disciplinary work with blend of knowledge and integration of expertise from passionate engineers!

Antenna sub-efficiency Integrals

$$G(\theta,\phi) = G_\theta(\theta,\phi)\hat{\theta} + G_\phi(\theta,\phi)\hat{\phi} = G_{co}(\theta,\phi)\hat{co} + G_{xp}(\theta,\phi)\hat{xp} \tag{A.1}$$

$$A_1(\theta) = \frac{1}{\pi}\int_0^{2\pi} G_\theta(\theta,\phi)\sin\phi d\phi \tag{A.2}$$

$$C_1(\theta) = \frac{1}{\pi}\int_0^{2\pi} G_\phi(\theta,\phi)\cos\phi d\phi \tag{A.3}$$

$$G_{co45}(\theta) = \frac{A_1(\theta)+C_1(\theta)}{2} \tag{A.4}$$

$$G_{xp45}(\theta) = \frac{A_1(\theta)-C_1(\theta)}{2} \tag{A.5}$$

$$\eta_{BOR_1} = \frac{2\pi\int_0^{\pi}\left[|G_{co45}(\theta)|^2 + |G_{xp45}(\theta)|^2\right]\sin\theta d\theta}{\int_0^{2\pi}\int_0^{\pi}\left[|G_{co}(\theta,\phi)|^2 + |G_{xp}(\theta,\phi)|^2\right]\sin\theta d\theta d\phi} \tag{A.6}$$

$$\eta_{spill} = \frac{\int_0^{\theta_o}\left[|G_{co45}(\theta)|^2 + |G_{xp45}(\theta)|^2\right]\sin\theta d\theta}{\int^{\pi}\left[|G_{co45}(\theta)|^2 + |G_{xp45}(\theta)|^2\right]\sin\theta d\theta} \tag{A.7}$$

$$\eta_{pol} = \frac{\int_0^{\theta_o}|G_{co45}(\theta)|^2\sin\theta d\theta}{\int^{\theta_o}\left[|G_{co45}(\theta)|^2 + |G_{xp45}(\theta)|^2\right]\sin\theta d\theta} \tag{A.8}$$

$$\eta_{ill} = 2\cot^2\left(\frac{\theta_o}{2}\right)\frac{\left[\int_0^{\theta_o}|G_{co45}(\theta)|\tan\left(\frac{\theta}{2}\right)d\theta\right]^2}{\int_0^{\theta_o}|G_{co45}(\theta)|^2\sin\theta d\theta} \tag{A.9}$$

$$\eta_{\o} = \frac{\left[\int^{\theta_o}|G_{co45}(\theta)|\tan\left(\frac{\theta}{2}\right)d\theta\right]^2}{\left|\int^{\theta_o}G_{co45}(\theta)\tan\left(\frac{\theta}{2}\right)d\theta\right|^2} \tag{A.10}$$

$$\eta_{BOR_1}^{Gauss} = \frac{\left|\int_0^{\frac{\pi}{2}}G_{co45}^A(\theta)\cdot G_{co45}^G(\theta)\sin\theta d\theta\right|^2}{\int_0^{\frac{\pi}{2}}\left|G_{co45}^A(\theta)\right|^2\sin\theta d\theta \int_0^{\frac{\pi}{2}}\left|G_{co45}^G(\theta)\right|^2\sin\theta d\theta} \tag{A.11}$$

$$\eta_{ap} = \eta_{BOR_1}\cdot\eta_{spill}\cdot\eta_{pol}\cdot\eta_{ill}\cdot\eta_{\o} \tag{A.12}$$

$$\eta_G = \eta_{BOR_1}\cdot\eta_{spill}\cdot\eta_{pol}\cdot\eta_{BOR_1}^{Gauss} \tag{A.13}$$

$\because$ θ_o is the half subtended angle of the prime focus reflector in case of aperture efficiency calculations while $\theta_o = \pi/2$ for Gaussian coupling efficiency calculations.

Gaussian Beam Far-field

The paraxial approximation of Gaussian Beams is a useful tool for modeling quasi-optical systems. These beams are often defined in cylindrical or rectangular coordinate systems. But for antenna, having it's far-field defined in spherical coordinate systems, to find its coupling to Gaussian beam modes; the far-field of Gaussian beams is required.

For accurate modeling of Gaussian Beam for far-field distances, the basic formulas describing the beam needs to be modified. The far-field of gaussian beam described in chapter 6.6.3 of [50] is based on beam radius and center of curvature of wavefront at aperture. On the other hand, the far-field described in (24) of [68] is based on beam waist with it's location at origin. Authors of [115] modify analysis of [68] further to get $\hat{\theta}$, $\hat{\phi}$ components of the field as shown in (33) of [115]. Thus several different definitions for Gaussian beam far-field exists. Hence, in this appendix, first the far-field of Gaussian beam is derived by modifying basic formulas for large distances and further different definitions of Gaussian beam far-field are compared with exact numerical results.

The normalized electrical field of Gaussian beam by it's definition is described in cylindrical coordinate system at point (ρ, z) using (2.26a-2.26d) of [67] and is as follows,

$$E(\rho, z) = \sqrt{\frac{2}{\pi}} \frac{1}{\omega} e^{\left(\frac{-\rho^2}{\omega^2} - jkz - \frac{jk\rho^2}{2R} + j\Phi_o \right)} \tag{B.1}$$

$$
\begin{aligned}
\because z_c &= \frac{\pi \omega_o^2}{\lambda} \\
\omega &= \omega_o \sqrt{1 + \left(\frac{z}{z_c} \right)^2} \\
R &= z + \frac{z_c^2}{z} \\
\Phi_o &= \tan^{-1}\left(\frac{z}{z_c} \right)
\end{aligned}
$$

But in far-field of an antenna, the electric field is described in spherical coordinate system at point R, θ. Now consider, the gaussian beam at distance much larger than it's confocal distance. i.e. $(z \gg z_c)$ Under this condition, the value of radius of curvature approaches to the distance z from the beam waist as shown in FigureB.1. The basic geometrical relations from FigureB.1 are given in (B.2-B.4)

$$\lim_{z \gg z_c} R = \lim_{z \gg z_c} z + \frac{z_c^2}{z} \qquad\qquad z = R \tag{B.2}$$

$$\rho = R \sin\theta \qquad\qquad z' = R \cos\theta \tag{B.3}$$

$$\rho + \Delta\rho = R \tan\theta \qquad\qquad R + \Delta R = R \sec\theta \tag{B.4}$$

Now, consider far-field at observation point R, θ. It is related to field at point ρ, z in cylindrical coordinate system by following relation,

$$E(R, \theta) = \lim_{z \gg z_c} E(\rho, z\prime) = \lim_{z \gg z_c} \alpha e^{j\beta} E(\rho, z) \tag{B.5}$$
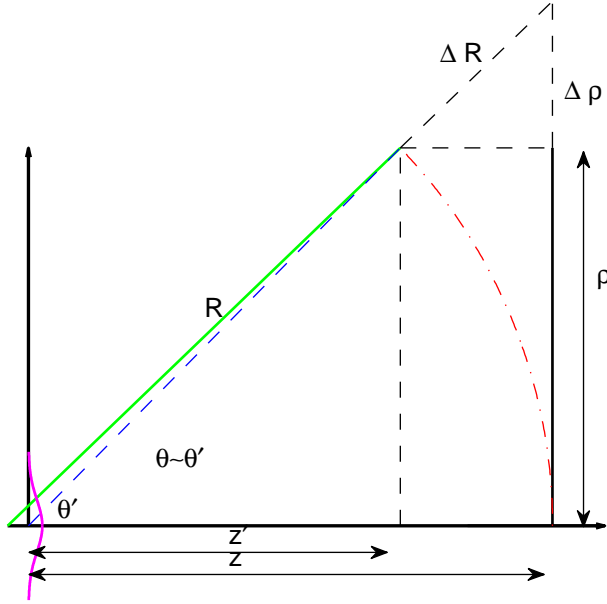
Figure B.1: Relation between Spherical and Cylindrical Coordinates

Assuming that $z \gg z_c$, the amplitude ratio α and phase difference β between the two fields can be evaluated as follows,

$$\alpha e^{j\beta} \;=\; \frac{E(\rho, z\prime)}{E(\rho, z)} \tag{B.6}$$

$$\therefore \alpha \;=\; \frac{|E(\rho, z\prime)|}{|E(\rho, z)|} \tag{B.7}$$

$$\therefore \beta \;=\; \angle E(\rho, z\prime) - \angle E(\rho, z) \tag{B.8}$$

The exact expression for α is given in (B.11) which can be approximated by $\cos(\theta)$ for paraxial beam. The difference between model and exact expression is shown in FigureB.2. Even though, the difference is large for higher values for θ; for $\theta < \theta_o$ i.e. -8.7 dB beam width, the error is negligible. Also the error shown in the FigureB.2 is for beam waist size of $\omega_o = 0.9\lambda$ which is the lowermost limit above which Gaussian beam formulation can be used safely [68].

$$\lim_{z \gg z_c} \omega \;=\; \omega_o \frac{z}{z_c} \simeq \frac{\lambda}{\pi \omega_o} \cdot R \tag{B.9}$$

$$\alpha \;=\; \frac{\omega}{\omega\prime} e^{-\frac{\rho^2}{\omega^2}\left(\frac{\omega^2}{\omega\prime^2}-1\right)} \tag{B.10}$$

$$\alpha \;=\; \frac{1}{\cos\theta} e^{-\left(\frac{\pi \omega_o}{\lambda}\right)^2 \sin^2\theta \tan^2\theta} \simeq \cos\theta \tag{B.11}$$

Similarly, for large distances β reduces to $k\rho^2/(2R)$. This is a useful result since

it removes the phase dependance of far-field from cylindrical coordinate ρ.

$$\beta = \frac{k\rho^2}{2R}\left[1 - \frac{R}{R\prime}\right] + kz\left[1 - \frac{z\prime}{z}\right] + \Phi\prime_o - \Phi_o \tag{B.12}$$

$$\lim_{z \gg z_c} \frac{R}{R\prime} \rightarrow 1 \tag{B.13}$$

$$\lim_{z \gg z_c} \Phi\prime_o - \Phi_o \rightarrow 0 \tag{B.14}$$

$$\beta \simeq kR[1 - \cos\theta] \simeq kR\left[1 - \sqrt{1 - \frac{\rho^2}{R^2}}\right] \tag{B.15}$$

$$\beta \simeq kR\left[1 - \left(1 - \frac{1}{2}\frac{\rho^2}{R^2}\right)\right] \tag{B.16}$$

$$\beta \simeq \frac{k\rho^2}{2R} \tag{B.17}$$

The approximate value of β agrees well with the exact phase difference between two field evaluated at distance of $z = 10z_c$ with in θ_o. This is also shown in FigureB.2.
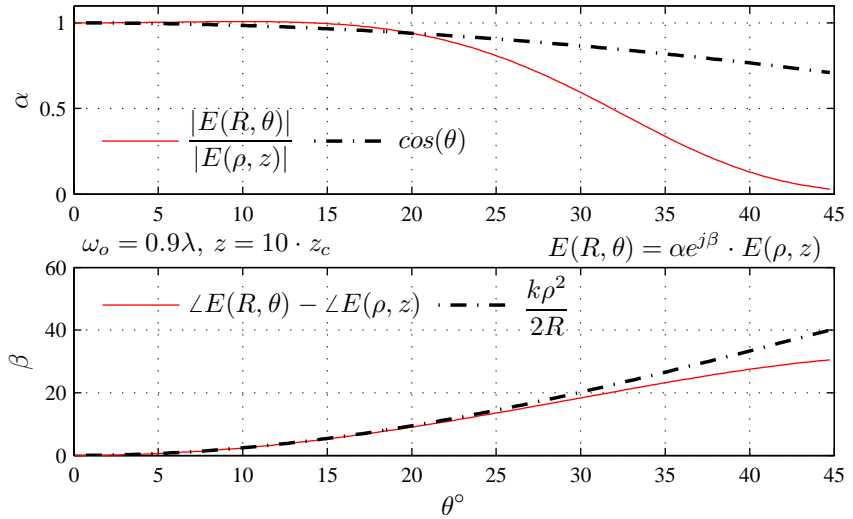
Figure B.2: Compare model with exact ratios between two fields.

As a last step, the field at point R, θ can now be evaluated by substituting (B.1-B.3),(B.17) and (B.11) in (B.5). The resultant E-field at far-field distance from origin is obtained in (B.20).

$$E(R,\theta) = \lim_{z \gg z_c} \cos\theta e^{j\frac{k\rho^2}{2R}}\sqrt{\frac{2}{\pi}}\frac{1}{\omega}e^{\left(\frac{-\rho^2}{\omega^2} - jkz - \frac{jk\rho^2}{2R} + j\Phi_o\right)} \tag{B.18}$$

$$E(R,\theta) = \cos\theta\sqrt{\frac{2}{\pi}}\lim_{z \gg z_c}\frac{1}{\omega}e^{\left(\frac{-\rho^2}{\omega^2} - jkz + j\Phi_o\right)} \tag{B.19}$$

$$E(R,\theta) = \frac{1}{R}e^{-jkR}\sqrt{\frac{2}{\pi}}\frac{\pi\omega_o}{\lambda}\cos\theta e^{-\left(\frac{\pi\omega_o}{\lambda}\right)^2\sin^2\theta + j\frac{\pi}{2}} \tag{B.20}$$

From this the far-field function can be extracted by suppressing the free space Green's function $1/Re^{-jkR}$ and normalizing the amplitude. Thus the resultant far-field function is given in (B.21).

$$G_{co45}(\theta) = cos\theta e^{-\left(\frac{\pi\omega_o}{\lambda}\right)^2 \sin^2\theta + j\frac{\pi}{2}} \tag{B.21}$$

This definition of far-field can now be compared with the exact analysis for Gaussian distribution on infinite size aperture using free space equivalent (section 6.3.2 of [50]) and rotationally symmetric circular aperture (section 6.5.3 of [50]). The accurate expression of far-field of Gaussian beam with beam waist ω_o at origin of coordinate system is given in (B.22). Also an approximate expression of far-field is available from section 6.6.3 of [50].

$$G_{co45}(\theta) = cos^2\left(\frac{\theta}{2}\right) e^{-\left(\frac{\pi\omega_o}{\lambda}\right)^2 \sin^2\theta} \tag{B.22}$$

$$G_{co45}(\theta) = e^{-\left(\frac{\pi\omega_o}{\lambda}\right)^2 \theta^2} \tag{B.23}$$
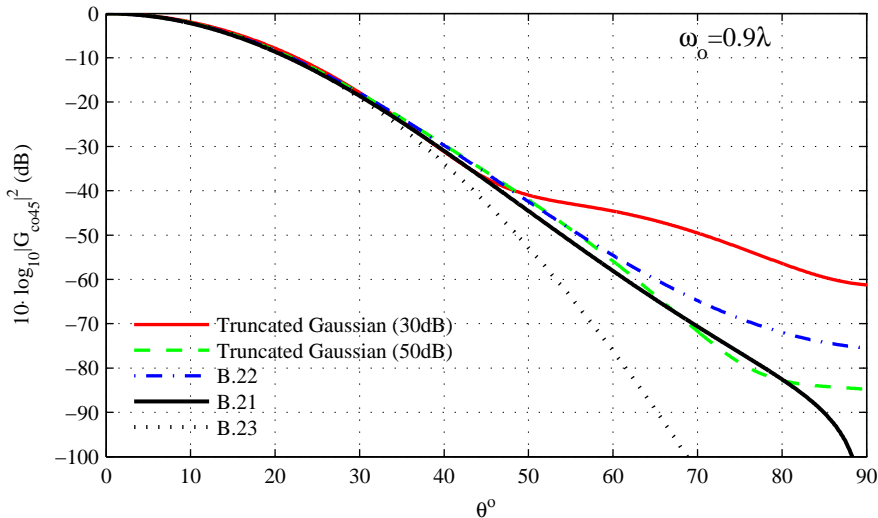
Figure B.3: Compare Gaussian Beam Far-field Expressions

These different expression are compared in FigureB.3 for beam waist size of 0.9λ. Also to get in depth understanding, the numerically computed far-field of truncated Gaussian distribution is also plotted for 30 dB and 50 dB taper at edge of aperture using [75]. It is seen from FigureB.3 that definitions (B.21),(B.22) and (B.23) produce similar beam patterns within 20 dB amplitude taper. After which, the approximate expression deviate from the accurate far-field of Gaussian distribution on infinite aperture.

With this analysis presented, the (B.21) is found to be the far-field of Gaussian beam and is used in this thesis for Gaussian Coupling Efficiency computations. But this definition still needs to be modified in terms of phase factor depending upon location of beam waist along z-axis. Hence, (B.21) is altered for beam waist location

z_o using (B.26).

$$G_{co45}(\theta, \omega_o, z_o) = G_{co45}(\theta)e^{-jkz_o\hat{z}\cdot\hat{r}} \tag{B.24}$$

$$G_{co45}(\theta, \omega_o, z_o) = G_{co45}(\theta)e^{-jkz_o\cos\theta} \tag{B.25}$$

$$G_{co45}(\theta, \omega_o, z_o) = cos\theta e^{-\left(\frac{\pi\omega_o}{\lambda}\right)^2\sin^2\theta + j\frac{\pi}{2} - jkz_o\cos\theta} \tag{B.26}$$

Signal Generator N-times Power Method

The conventional and most common method to measure noise of a two port network is a Y-factor method [116]. In this method, a noise source or HOT/COLD load is used to obtain ratio of two different resulting output powers. This ratio is referred as Y-factor and from which the system temperature is deduced using (C.1). In millimeter, sub-millimeter bands, to measure system noise of an antenna integrated receiver, a more practical approach is to first terminate antenna aperture with absorber at room temperature (referred as HOT) and later on with absorber soaked with liquid Nitrogen (referred as COLD). Again from the ratio of measured output powers, the system noise temperature is estimated.

$$T_{sys} = \frac{T_{HOT} - Y T_{COLD}}{Y - 1} \tag{C.1}$$

Usually the power is measured using a power meter along with a band pass filter to define measurement bandwidth. For moderate noise figures (up to several dBs) the Y-factor produced is more than half dB. But for noise figures exceeding 10 dBs, Y-factor ($\simeq$ 0.1-0.2 dB) becomes comparable to the measurement accuracy of the power meter and hence the measurement of high noise figures with this method can be erroneous. The Table B.1 shows the Y-factor values for Noise figures ranging from 1-16 dB.

Table C.1: Y-factors for moderate to high Noise Figures

Noise Figure (dB)	Noise Temperature (K)	Y-Factor (dB)
1	75.09	3.803
2	169.62	2.704
3	288.63	1.994
4	438.45	1.502
5	627.06	1.148
6	864.51	0.886
7	1163.44	0.688
8	1539.78	0.537
9	2013.55	0.421
10	2610.00	0.331
11	3360.88	0.261
12	4306.19	0.206
13	5496.26	0.163
14	6994.47	0.129
15	8880.61	0.102
16	11255.11	0.081

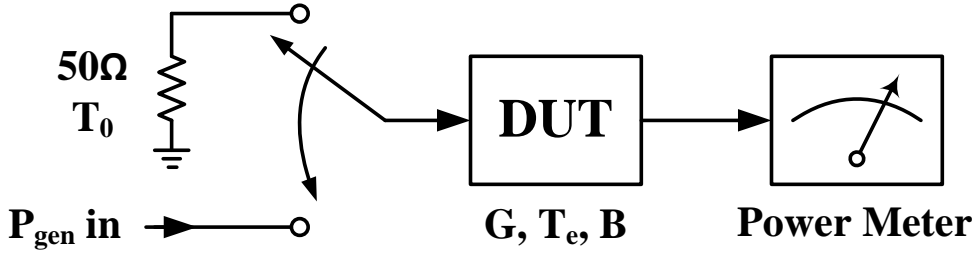$T_{HOT} = 290K$ and $T_{COLD} = 77K$

Figure C.1: Estimation of Noise Temperature using Signal Generator

To overcome this limitation, another more widely used method is "Signal Generator Twice Power Method" [117]. In this method, first the input is terminated with matched load and power is recorded. Later, the power from the signal generator is applied to the circuit such that the output power is twice the power under matched load. The value of generator power causing this 3 dB rise in output power is then used to estimate system temperature as in (C.2). The measurement setup for this method is shown in Fig. C.1.

$$T_{sys} = \frac{P_{gen}}{kB_n} - T_o \tag{C.2}$$

But when working in THz frequency bands, often the generator power is obtained using multiplier chains and the control over its output power is limited. Also there could be variations in the output power levels over the frequency band of interest. Hence, the Signal Generator Twice Power Method needs to be modified such that the known/available generator power can be used to estimate system temperature.

Let's assume that P_1 is the power measured in the noise bandwidth B_n of the bandpass filter when the system input is terminated using resistive load at room temperature (for antenna integrated receiver it is an absorber at room temperature). Hence, the output power is written using (C.3). Later known generator power P_{gen} is applied to the circuit and corresponding output power is measured as P_2. This power is the sum of noise power and generator power as shown in (C.4). Now if the ratio of powers P_2 to P_1 is referred as N then corresponding system temperature and noise figure is written as in (C.5),(C.6) respectively.

$$
\begin{align}
P_1 &= k\left(T_o + T_{sys}\right) B_n G_{sys} \tag{C.3} \\
P_2 &= k\left(T_o + T_{sys}\right) B_n G_{sys} + P_{gen} G_{sys} \tag{C.4} \\
T_{sys} &= \frac{P_{gen}}{kB_n(N-1)} - T_o \tag{C.5} \\
F_{sys} &= \frac{P_{gen}}{kT_o B_n(N-1)} \tag{C.6} \\
\because N &= \frac{P_2}{P_1} \tag{C.7}
\end{align}
$$

The equation (C.5) would reduce to (C.2) if the ratio of powers is 3 dB. Thus (C.5) is more generalized case of "Signal Generator Twice Power Method" and hence it is referred as "N-times method". This method can be used to measure noise figures resistive mixers which can be above 10 dBs.

References

[1] R. Mittra, "A tribute to jagadis chunder bose on the occasion of his sesqui-centennial birthday celebration [reverberations]," *Microwave Magazine, IEEE*, vol. 10, no. 2, pp. 118 –119, april 2009.

[2] P. Siegel, "Sir jagadis chunder bose: Traversing the interdisciplinary gap between physics and biology [reverberations]," *Microwave Magazine, IEEE*, vol. 10, no. 2, pp. 119 –121, april 2009.

[3] P. H. Siegel, "Terahertz technology," *Microwave Theory and Techniques, IEEE Transactions on*, vol. 50, no. 3, pp. 910 –928, mar 2002.

[4] Y. Yang, M. Mandehgar, and D. Grischkowsky, "Broadband thz pulse transmission through the atmosphere," *Terahertz Science and Technology, IEEE Transactions on*, vol. 1, no. 1, pp. 264 –273, sept. 2011.

[5] D. Dragoman and M. Dragoman, "Terahertz fields and applications," *Progress in Quantum Electronics*, vol. 28, no. 1, pp. 1 – 66, 2004. [Online]. Available: http://www.sciencedirect.com/science/article/pii/S0079672703000582

[6] F. Sizov and A. Rogalski, "Thz detectors," *Progress in Quantum Electronics*, vol. 34, no. 5, pp. 278 – 347, 2010. [Online]. Available: http://www.sciencedirect.com/science/article/pii/S007967271000025X

[7] P. Siegel, "Thz instruments for space," *Antennas and Propagation, IEEE Transactions on*, vol. 55, no. 11, pp. 2957 –2965, nov. 2007.

[8] P. H. Siegel, "Thz for space: The golden age," in *Microwave Symposium Digest (MTT), 2010 IEEE MTT-S International*, may 2010, p. 1.

[9] ALMA, "Atacama large millimeter/submillimeter array," http://www.almaobservatory.org.

[10] H.-J. Song and T. Nagatsuma, "Present and future of terahertz communications," *Terahertz Science and Technology, IEEE Transactions on*, vol. 1, no. 1, pp. 256 –263, sept. 2011.

[11] K.-C. Huang and Z. Wang, "Terahertz terabit wireless communication," *Microwave Magazine, IEEE*, vol. 12, no. 4, pp. 108 –116, june 2011.

[12] C. Jastrow, S. Priebe, B. Spitschan, J. Hartmann, M. Jacob, T. Kurner, T. Schrader, and T. Kleine-Ostmann, "Wireless digital data transmission at 300 ghz," *Electronics Letters*, vol. 46, no. 9, pp. 661 –663, 29 2010.

[13] P. Siegel, "Terahertz technology in biology and medicine," *Microwave Theory and Techniques, IEEE Transactions on*, vol. 52, no. 10, pp. 2438 – 2447, oct. 2004.

[14] Y.-C. Shen and P. Taday, "Development and application of terahertz pulsed imaging for nondestructive inspection of pharmaceutical tablet," *Selected Topics in Quantum Electronics, IEEE Journal of*, vol. 14, no. 2, pp. 407 –415, march-april 2008.

[15] K. Cooper, R. Dengler, G. Chattopadhyay, E. Schlecht, J. Gill, A. Skalare, I. Mehdi, and P. Siegel, "A high-resolution imaging radar at 580 ghz," *Microwave and Wireless Components Letters, IEEE*, vol. 18, no. 1, pp. 64 –66, jan. 2008.

[16] N. Llombart, T. Bryllert, G. Chattopadhyay, K. Cooper, R. Dengler, J. Gill, A. McNary, I. Mehdi, E. Schlecht, A. Skalare, and P. Siegel, "Thz heterodyne imaging applications, instruments and directions," in *Microwave Conference, 2008. EuMC 2008. 38th European*, oct. 2008, pp. 947 –950.

[17] N. Llombart, K. Cooper, R. Dengler, T. Bryllert, and P. Siegel, "Confocal ellipsoidal reflector system for a mechanically scanned active terahertz imager," *Antennas and Propagation, IEEE Transactions on*, vol. 58, no. 6, pp. 1834 – 1841, june 2010.

[18] K. Cooper, R. Dengler, N. Llombart, B. Thomas, G. Chattopadhyay, and P. Siegel, "Thz imaging radar for standoff personnel screening," *Terahertz Science and Technology, IEEE Transactions on*, vol. 1, no. 1, pp. 169 –182, sept. 2011.

[19] E. Grossman, C. Dietlein, M. Leivo, A. Rautiainen, and A. Luukanen, "A passive, real-time, terahertz camera for security screening, using superconducting microbolometers," in *Microwave Symposium Digest, 2009. MTT '09. IEEE MTT-S International*, june 2009, pp. 1453 –1456.

[20] J. Jackson, J. Bowen, G. Walker, J. Labaune, G. Mourou, M. Menu, and K. Fukunaga, "A survey of terahertz applications in cultural heritage conservation science," *Terahertz Science and Technology, IEEE Transactions on*, vol. 1, no. 1, pp. 220 –231, sept. 2011.

[21] H.-W. Hubers, "Terahertz heterodyne receivers," *Selected Topics in Quantum Electronics, IEEE Journal of*, vol. 14, no. 2, pp. 378 –391, march-april 2008.

[22] J. Zmuidzinas and P. Richards, "Superconducting detectors and mixers for millimeter and submillimeter astrophysics," *Proceedings of the IEEE*, vol. 92, no. 10, pp. 1597 – 1616, oct. 2004.

[23] V. Vassilev, D. Henke, I. Lapkin, O. Nystrom, R. Monje, A. Pavolotsky, and V. Belitsky, "Design and characterization of a 211-275 ghz sideband separating mixer for the apex telescope," *Microwave and Wireless Components Letters, IEEE*, vol. 18, no. 1, pp. 58 –60, jan. 2008.

[24] J. W. Kooi, R. A. Chamberlin, R. Monje, B. Force, D. Miller, and T. G. Phillips, "Balanced receiver technology development for the caltech submillimeter observatory," *Terahertz Science and Technology, IEEE Transactions on*, vol. 2, no. 1, pp. 71 –82, jan. 2012.

[25] A. Semenov, H.-W. Hubers, H. Richter, M. Birk, M. Krocka, U. Mair, Y. Vachtomin, M. Finkel, S. Antipov, B. Voronov, K. Smirnov, N. Kaurova, V. Drakinski, and G. Gol'tsman, "Superconducting hot-electron bolometer mixer for terahertz heterodyne receivers," *Applied Superconductivity, IEEE Transactions on*, vol. 13, no. 2, pp. 168 – 171, june 2003.

[26] S. Cherednichenko, V. Drakinskiy, T. Berg, P. Khosropanah, and E. Kollberg, "Hot-electron bolometer terahertz mixers for the herschel space observatory," *Review of Scientific Instruments*, vol. 79, no. 3, p. 034501, 2008. [Online]. Available: http://link.aip.org/link/?RSI/79/034501/1

[27] A. Maestrini, B. Thomas, H. Wang, C. Jung, J. Treuttel, Y. Jin, G. Chattopadhyay, I. Mehdi, and G. Beaudin, "Schottky diode-based terahertz frequency multipliers and mixers," *Comptes Rendus Physique*, vol. 11, no. 78, pp. 480 – 495, 2010. [Online]. Available: http://www.sciencedirect.com/science/article/pii/S1631070510000447

[28] B. Thomas, A. Maestrini, J. Gill, C. Lee, R. Lin, I. Mehdi, and P. de Maagt, "A broadband 835-900-ghz fundamental balanced mixer based on monolithic gaas membrane schottky diodes," *Microwave Theory and Techniques, IEEE Transactions on*, vol. 58, no. 7, pp. 1917 –1924, july 2010.

[29] B. Thomas, A. Maestrini, and G. Beaudin, "A low-noise fixed-tuned 300-360-ghz sub-harmonic mixer using planar schottky diodes," *Microwave and Wireless Components Letters, IEEE*, vol. 15, no. 12, pp. 865 – 867, dec. 2005.

[30] P. Sobis, A. Emrich, and J. Stake, "A low vswr 2sb schottky receiver," *Terahertz Science and Technology, IEEE Transactions on*, vol. 1, no. 2, pp. 403 –411, nov. 2011.

[31] W. Deal, X. Mei, K. Leong, V. Radisic, S. Sarkozy, and R. Lai, "Thz monolithic integrated circuits using inp high electron mobility transistors," *Terahertz Science and Technology, IEEE Transactions on*, vol. 1, no. 1, pp. 25 –32, sept. 2011.

[32] J. Hacker, M. Seo, A. Young, Z. Griffith, M. Urteaga, T. Reed, and M. Rodwell, "Thz mmics based on inp hbt technology," in *Microwave Symposium Digest (MTT), 2010 IEEE MTT-S International*, may 2010, pp. 1126 –1129.

[33] L. Samoska, "An overview of solid-state integrated circuit amplifiers in the submillimeter-wave and thz regime," *Terahertz Science and Technology, IEEE Transactions on*, vol. 1, no. 1, pp. 9 –24, sept. 2011.

[34] R. Pengelly and J. Turner, "Monolithic broadband gaas f.e.t. amplifiers," *Electronics Letters*, vol. 12, no. 10, pp. 251 –252, 13 1976.

[35] S. Marsh, *Practical MMIC Design*. Norwood, MA: Artech House, 2006.

[36] I. D. Robertson, *RFIC and MMIC design and technology*. United Kingdom: IEE circuits, devices and systems series; no. 13, 2001.

[37] F. Schwierz and J. Liou, *Modern Microwave Transistors, Theory, Design and Performance*. New Jersey: John Wiley & Sons, Inc., 2003.

[38] S. Iyer, G. Patton, S. Delage, S. Tiwari, and J. Stork, "Silicon-germanium base heterojunction bipolar transistors by molecular beam epitaxy," in *Electron Devices Meeting, 1987 International*, vol. 33, 1987, pp. 874 – 876.

[39] M. Urteaga, M. Seo, J. Hacker, Z. Griffith, A. Young, R. Pierson, P. Rowell, A. Skalare, V. Jain, E. Lobisser, and M. Rodwell, "Inp hbts for thz frequency integrated circuits," in *Compound Semiconductor Week (CSW/IPRM), 2011 and 23rd International Conference on Indium Phosphide and Related Materials*, may 2011, pp. 1 –4.

[40] G. Gonzalez, *Microwave Transistor Amplifiers Analysis and Design*. New Jersey: Prentice Hall, 1997.

[41] M. Urteaga, R. Pierson, P. Rowell, V. Jain, E. Lobisser, and M. Rodwell, "130nm inp dhbts with $f_t > 0.52$ thz and $f_{max} > 1.1$ thz," in *Device Research Conference (DRC), 2011 69th Annual*, june 2011, pp. 281 –282.

[42] T. Mimura, "The early history of the high electron mobility transistor (hemt)," *Microwave Theory and Techniques, IEEE Transactions on*, vol. 50, no. 3, pp. 780 –782, mar 2002.

[43] D.-H. Kim, J. del Alamo, P. Chen, W. Ha, M. Urteaga, and B. Brar, "50-nm e-mode in0.7ga0.3as phemts on 100-mm inp substrate with fmax > 1 thz," in *Electron Devices Meeting (IEDM), 2010 IEEE International*, dec. 2010, pp. 30.6.1 –30.6.4.

[44] A. Leuther, R. Weber, M. Dammann, M. Schlechtweg, M. Mikulla, M. Walther, and G. Weimann, "Metamorphic 50 nm inas-channel hemt," in *Indium Phosphide and Related Materials, 2005. International Conference on*, may 2005, pp. 129 – 132.

[45] D.-H. Kim and J. del Alamo, "30-nm inas pseudomorphic hemts on an inp substrate with a current-gain cutoff frequency of 628 ghz," *Electron Device Letters, IEEE*, vol. 29, no. 8, pp. 830 –833, aug. 2008.

[46] ——, "30-nm inas phemts with $f_t = 644$ $ghz$and $f_{max} = 681$ ghz," *Electron Device Letters, IEEE*, vol. 31, no. 8, pp. 806 –808, aug. 2010.

[47] D.-H. Kim, B. Brar, and J. A. del Alamo, "$f_t = 688$ ghz and $f_{max} = 800$ ghz in lg = 40 nm in0.7ga0.3as mhemts with $gm_{max} > 2.7ms/\mu m$," in *Electron Devices Meeting (IEDM), 2011 IEEE International*, dec. 2011, pp. 13.6.1 –13.6.4.

[48] C. Balanis, *Antenna Theory: analysis and design*. New Jersey: Wiley, 2005.

[49] J. Kraus and R. Marhefka, *Antennas: for all applications*. Boston: McGraw-Hill, 2002.

[50] P.-S. Kildal, *Foundations of Antennas: A Unified Approach*. Lund, Sweden: studentlitteratur, 2000.

[51] ——, "Ota measurements of wireless stations in reverberation chamber versus anechoic chamber: from accuracy models to testing of mimo systems," in *Antenna Technology (iWAT), 2010 International Workshop on*, march 2010, pp. 1 –4.

[52] K. Rosengren and P.-S. Kildal, "Study of distributions of modes and plane waves in reverberation chambers for the characterization of antennas in a multipath environment," *Microwave and Optical Technology Letters*, vol. 30, no. 6, pp. 386–391, 2001. [Online]. Available: http://dx.doi.org/10.1002/mop.1323

[53] P.-S. Kildal, "Factorization of the feed efficiency of paraboloids and cassegrain antennas," *Antennas and Propagation, IEEE Transactions on*, vol. 33, no. 8, pp. 903 – 908, aug 1985.

[54] ——, "Combined e - and h -plane phase centers of antenna feeds," *Antennas and Propagation, IEEE Transactions on*, vol. 31, no. 1, pp. 199 – 202, jan 1983.

[55] ——, "Comments on "phase center calculations of reflector antenna feeds","
Antennas and Propagation, IEEE Transactions on, vol. 33, no. 5, pp. 579 –580,
may 1985.

[56] P. Kildal and Z. Sipus, "Classification of rotationally symmetric antennas as
types bor 0 and bor 1," *Antennas and Propagation Magazine, IEEE*, vol. 37,
no. 6, p. 114, Dec. 1995.

[57] Z. Ying, A. Kishk, and P.-S. Kildal, "Broadband compact horn feed for prime-
focus reflectors," *Electronics Letters*, vol. 31, no. 14, pp. 1114 –1115, jul 1995.

[58] Y. Karandikar and P.-S. Kildal, "X-ka dual band prime focus feed for satel-
lite earth terminals," in *Antennas and Propagation, 2009. EuCAP 2009. 3rd
European Conference on*, march 2009, pp. 3085 –3089.

[59] R. Olsson, P.-S. Kildal, and S. Weinreb, "Measurements of a 1 to 13 ghz model
of a dual polarized low-profile log-periodic feed for us-ska," in *Antennas and
Propagation Society International Symposium, 2005 IEEE*, vol. 2B, july 2005,
pp. 700 – 703 vol. 2B.

[60] ——, "The eleven antenna: a compact low-profile decade bandwidth dual polar-
ized feed for reflector antennas," *Antennas and Propagation, IEEE Transactions
on*, vol. 54, no. 2, pp. 368 – 375, feb. 2006.

[61] R. Olsson, P.-S. Kildal, and M. Shields, "Measurements of a 150 to 1700 mhz
low loss eleven feed for the 42 m radio telescope at green bank," in *Antennas
and Propagation Society International Symposium 2006, IEEE*, july 2006, pp.
347 –350.

[62] Y. Karandikar and P. Kildal, "Optimization of 200-800mhz eleven feed for gmrt,"
in *Antennas and Propagation, 2007. EuCAP 2007. The Second European Con-
ference on*, nov. 2007, pp. 1 –6.

[63] J. Yang, S. Pivnenko, T. Laitinen, J. Carlsson, and X. Chen, "Measurements
of diversity gain and radiation efficiency of the eleven antenna by using dif-
ferent measurement techniques," in *Antennas and Propagation (EuCAP), 2010
Proceedings of the Fourth European Conference on*, april 2010, pp. 1 –5.

[64] N. Wadefalk, P.-S. Kildal, and H. Zirath, "A low noise integrated 0.3-16 ghz dif-
ferential amplifier for balanced ultra wideband antennas," in *Compound Semi-
conductor Integrated Circuit Symposium (CSICS), 2010 IEEE*, oct. 2010, pp. 1
–4.

[65] Y. B. Karandikar, J. Yang, and P.-S. Kildal, "Reduction of radiation from central
exciting region of eleven feed and pattern improvements for vlbi2010 applica-
tions," in *Antennas and Propagation (EuCAP), 2010 Proceedings of the Fourth
European Conference on*, april 2010, pp. 1 –5.

[66] Y. B. Karandikar and P.-S. Kildal, "Comparisons of different descrambler/power
combining boards layout for multi-port, decade bandwidth eleven feed," in *An-
tennas and Propagation (EuCAP), 2010 Proceedings of the Fourth European
Conference on*, april 2010, pp. 1 –6.

[67] P. F. Goldsmith, *Quasioptical Systems: Gaussian beam quasioptical propagation
and applications.* Piscataway,NJ: IEEE Press, 1998.

[68] J. Tuovinen, "Accuracy of a gaussian beam," *Antennas and Propagation, IEEE Transactions on*, vol. 40, no. 4, pp. 391 –398, Apr. 1992.

[69] S. E. Schwarz, "Efficiency of quasi-optical couplers," *International Journal of Infrared and Millimeter Waves*, vol. 5, pp. 1517–1525, 1984, 10.1007/BF01040503. [Online]. Available: http://dx.doi.org/10.1007/BF01040503

[70] W. B. Dou and Z. L. Sun, "A note on the coupling efficiency between an antenna and a gaussian beam," *International Journal of Infrared and Millimeter Waves*, vol. 17, pp. 1235–1241, 1996, 10.1007/BF02088909. [Online]. Available: http://dx.doi.org/10.1007/BF02088909

[71] R. Wylde, "Millimetre-wave gaussian beam-mode optics and corrugated feed horns," *Microwaves, Optics and Antennas, IEE Proceedings H*, vol. 131, no. 4, pp. 258 –262, 1984.

[72] J. Murphy, M. McCabe, and S. Withington, "Gaussian beam mode analysis of the coupling of power between horn antennas," *International Journal of Infrared and Millimeter Waves*, vol. 18, pp. 501–518, 1997, 10.1007/BF02677936. [Online]. Available: http://dx.doi.org/10.1007/BF02677936

[73] P.-S. Kildal, "Gaussian beam model for aperture-controlled and flareangle-controlled corrugated horn antennas," *Microwaves, Antennas and Propagation, IEE Proceedings H*, vol. 135, no. 4, pp. 237 – 240, Aug. 1988.

[74] P. Kittara, G. Yassin, and S. Withington, "Theoretical analysis of the pickett potter horn-reflector antenna for submillimetre-wave applications," in *High Frequency Postgraduate Student Colloquium, 1999*, 1999.

[75] A. Buck, "The radiation pattern of a truncated gaussian aperture distribution," *Proceedings of the IEEE*, vol. 55, no. 3, pp. 448 – 450, 1967.

[76] C. Balanis, *Modern Antenna Handbook*. USA: John Wiley & Sons Inc., 2008.

[77] D. Liu, B. Gaucher, U. Pfeiffer, and G. J., *Advanced Millimeter-wave Technologies*. UK: Wiley, 2009.

[78] K. Gupta and H. P., *Analysis and Design of Integrated Circuit Antenna Modules*. New York: Wiley Series in Microwave and Optical Engineering, 2000.

[79] G. Rebeiz, "Millimeter-wave and terahertz integrated circuit antennas," *Proceedings of the IEEE*, vol. 80, no. 11, pp. 1748 –1770, nov 1992.

[80] H.-M. Heiliger, M. Nagel, H. G. Roskos, H. Kurz, F. Schnieder, W. Heinrich, R. Hey, and K. Ploog, "Low-dispersion thin-film microstrip lines with cyclotene (benzocyclobutene) as dielectric medium," *Applied Physics Letters*, vol. 70, no. 17, pp. 2233 –2235, april 1997.

[81] C. Balanis, *Advanced engineering electromagnetics*. New York: Wiley, 1989.

[82] G. Kumar and K. Ray, *Broadband microstrip antennas*. Artech House, 2003.

[83] D. Filipovic, S. Gearhart, and G. Rebeiz, "Double-slot antennas on extended hemispherical and elliptical silicon dielectric lenses," *Microwave Theory and Techniques, IEEE Transactions on*, vol. 41, no. 10, pp. 1738 –1749, oct 1993.

[84] v. d. Vorst, "Integrated lens antennas for submillimetre-wave applications," Ph.D. dissertation, Technische Universiteit Eindhoven, 1999.

[85] D. Pasqualini and S. Maci, "High-frequency analysis of integrated dielectric lens antennas," *Antennas and Propagation, IEEE Transactions on*, vol. 52, no. 3, pp. 840 – 847, march 2004.

[86] W. Dou, G. Zeng, and Z. Sun, "Pattern prediction of extended hemispherical-lens/objective-lens antenna system at millimetre wavelengths," *Microwaves, Antennas and Propagation, IEE Proceedings -*, vol. 145, no. 4, pp. 295 –298, aug 1998.

[87] A. Karttunen, "Design of feed systems for hologram-based compact antenna test ranges," Helsinki University of Technology, Tech. Rep., 2009.

[88] M. van der Vorst, P. de Maagt, A. Neto, A. Reynolds, R. Heeres, W. Luinge, and M. Herben, "Effect of internal reflections on the radiation properties and input impedance of integrated lens antennas-comparison between theory and measurements," *Microwave Theory and Techniques, IEEE Transactions on*, vol. 49, no. 6, pp. 1118 –1125, jun 2001.

[89] A. Neto, S. Maci, and P. De Maagt, "Reflections inside an elliptical dielectric lens antenna," *Microwaves, Antennas and Propagation, IEE Proceedings -*, vol. 145, no. 3, pp. 243 –247, jun 1998.

[90] B. Das and K. Joshi, "Impedance of a radiating slot in the ground plane of a microstripline," *Antennas and Propagation, IEEE Transactions on*, vol. 30, no. 5, pp. 922 – 926, sep 1982.

[91] D. Pozar, N. Das, B. Das, and K. Joshi, "Comments on "impedance of a radiating slot in the ground plane of a microstripline"," *Antennas and Propagation, IEEE Transactions on*, vol. 34, no. 7, pp. 958 – 959, jul 1986.

[92] C.-L. Li, P.-Y. Lin, and C.-K. Huang, "Impedance bandwidth improvement for microstrip-fed slot antennas using short-circuited termination," *Microwave and Optical Technology Letters*, vol. 45, no. 1, pp. 67–70, 2005. [Online]. Available: http://dx.doi.org/10.1002/mop.20726

[93] B. Chantraine-Bares, R. Sauleau, L. Le Coq, and K. Mahdjoubi, "A new accurate design method for millimeter-wave homogeneous dielectric substrate lens antennas of arbitrary shape," *Antennas and Propagation, IEEE Transactions on*, vol. 53, no. 3, pp. 1069 – 1082, march 2005.

[94] M. Abbasi, S. Gunnarsson, N. Wadefalk, R. Kozhuharov, J. Svedin, S. Cherednichenko, I. Angelov, I. Kallfass, A. Leuther, and H. Zirath, "Single-chip 220-ghz active heterodyne receiver and transmitter mmics with on-chip integrated antenna," *Microwave Theory and Techniques, IEEE Transactions on*, vol. 59, no. 2, pp. 466 –478, feb. 2011.

[95] S. Gunnarsson, N. Wadefalk, J. Svedin, S. Cherednichenko, I. Angelov, H. Zirath, I. Kallfass, and A. Leuther, "A 220 ghz single-chip receiver mmic with integrated antenna," *Microwave and Wireless Components Letters, IEEE*, vol. 18, no. 4, pp. 284 –286, april 2008.

[96] A. Neto, "Uwb, non dispersive radiation from the planarly fed leaky lens antenna -part 1: Theory and design," *Antennas and Propagation, IEEE Transactions on*, vol. 58, no. 7, pp. 2238 –2247, july 2010.

[97] A. Neto, S. Monni, and F. Nennie, "Uwb, non dispersive radiation from the planarly fed leaky lens antenna -part ii: Demonstrators and measurements," *Antennas and Propagation, IEEE Transactions on*, vol. 58, no. 7, pp. 2248 – 2258, july 2010.

[98] N. Llombart, G. Chattopadhyay, A. Skalare, and I. Mehdi, "Novel terahertz antenna based on a silicon lens fed by a leaky wave enhanced waveguide," *Antennas and Propagation, IEEE Transactions on*, vol. 59, no. 6, pp. 2160 –2168, june 2011.

[99] G. Chattopadhayay, C. Lee, C. Jung, R. Lin, A. Peralta, I. Mehdi, N. Llombert, and B. Thomas, "Integrated arrays on silicon at terahertz frequencies," in *Antennas and Propagation (APSURSI), 2011 IEEE International Symposium on*, july 2011, pp. 3007 –3010.

[100] S. Mass, *Microwave Mixers.* Norwood,MA: Artech House, 1993.

[101] ——, *The RF and Microwave circuit design cookbook.* Boston: Artech House, 1998.

[102] ——, *Nonlinear microwave and RF circuits.* Boston: Artech House, 2003.

[103] S. Gunnarsson, "Analysis and design of a novel 4 subharmonically pumped resistive hemt mixer," *Microwave Theory and Techniques, IEEE Transactions on*, vol. 56, no. 4, pp. 809 –816, april 2008.

[104] K. Yhland, "Simplified analysis of resistive mixers," *Microwave and Wireless Components Letters, IEEE*, vol. 17, no. 8, pp. 604 –606, aug. 2007.

[105] A. A. Saleh, *Theory of Resistive Mixers.* Massachusetts: The M.I.T. Press, 1971.

[106] S. Maas, "A gaas mesfet mixer with very low intermodulation," *Microwave Theory and Techniques, IEEE Transactions on*, vol. 35, no. 4, pp. 425 – 429, apr 1987.

[107] H. Zirath, "A subharmonically pumped resistive dual-hemt-mixer," in *Microwave Symposium Digest, 1991., IEEE MTT-S International*, jul 1991, pp. 875 –878 vol.2.

[108] H. Zirath, I. Angelov, N. Rorsman, C. Karisson, and M. Sironen, "A millimeterwave allnas-gainas hfet-based subharmonically pumped mixer," in *Microwave Conference, 1995. 25th European*, vol. 1, sept. 1995, pp. 294 –298.

[109] B. Gilbert, "A precise four-quadrant multiplier with subnanosecond response," *Solid-State Circuits, IEEE Journal of*, vol. 3, no. 4, pp. 365 –373, dec. 1968.

[110] S. Gunnarsson, M. Gavell, D. Kuylenstierna, and H. Zirath, "60 ghz mmic double balanced gilbert mixer in mhemt technology with integrated rf, lo and if baluns," *Electronics Letters*, vol. 42, no. 24, pp. 1402 –1403, 23 2006.

[111] T.-H. Wu, S.-C. Tseng, C.-C. Meng, and G.-W. Huang, "Gainp/gaas hbt sub-harmonic gilbert mixers using stacked-lo and leveled-lo topologies," *Microwave Theory and Techniques, IEEE Transactions on*, vol. 55, no. 5, pp. 880 –889, may 2007.

[112] E. Ojefors, B. Heinemann, and U. Pfeiffer, "A 220ghz subharmonic receiver front end in a sige hbt technology," in *Radio Frequency Integrated Circuits Symposium (RFIC), 2011 IEEE*, june 2011, pp. 1 –4.

[113] I. Higgins, "Performance of self-oscillating gaas mesfet mixers at x-band," *Electronics Letters*, vol. 12, no. 23, pp. 605 –606, 11 1976.

[114] M. Roberts, S. Iezekiel, and C. Snowden, "A w-band self-oscillating subharmonic mmic mixer," *Microwave Theory and Techniques, IEEE Transactions on*, vol. 46, no. 12, pp. 2104 –2108, dec 1998.

[115] A. Friberg, T. Jaakkola, and J. Tuovinen, "Electromagnetic gaussian beam beyond the paraxial regime," *Antennas and Propagation, IEEE Transactions on*, vol. 40, no. 8, pp. 984 –989, Aug. 1992.

[116] D. Pozar, *Microwave Engineering.* New York, USA: John Wiley & Sons, 2004.

[117] Agilent, "Fundamentals of rf and microwave noise figure measurements," Agilent Technologies Inc., Tech. Rep. Application Note 57-1, August 2010. [Online]. Available: http://cp.literature.agilent.com/litweb/pdf/5952-8255E.pdf